# PROPERTIES OF CEMENT- BASED SOLIDIFIED WASTE CONTAINING LEAD AND CHROMIUM HYDROXIDES

**\*A. El- Dakroury**

*Hot lab. Center and waste management*
*Atomic Energy Authority, Hot Laboratories and Center, 13759 Cairo Egypt*
*E-mail: aishaw95@yahoo.com*

## ABSTRACT

Experiments were completed to investigate the effects of synthetic lead and chromium hydroxides on the properties of cement-based solidified wastes. Synthetic lead and chromium hydroxides have been mixed with Ordinary Portland Cement at 10, 20 and 30 wt % and a water-to-solid ratio of 0.45 was used throughout the experiments. The final setting, strength development and metal leachability of the solidified wastes were determined using Vicat Needle, unconfined compressive strength and a modified American Nuclear Standards Committee (ANSI/ ANS -16.1) respectively. It was found that the addition of lead and chromium hydroxides interferes with the normal hydration reaction of OPC by prolonging the final setting time from 4 hours to 78 and 100 hours at 10 and 20wt % of lead hydroxide and setting was not observed up to 150 hours at a 30 wt %. Chromium hydroxide also causes similar interference but the effect is significantly less than that of lead hydroxide. The hydration retardation caused by the addition of lead and chromium hydroxide results in the microstructures development of the solidified wastes to be different from that of normal cement hydration and therefore the compressive strength ofthe solidified wastes has been reduced. Leaching of lead and chromium from the solidified wastes is determined by leachate pH. The ingression of acidic leachant through connected primarily porosity of the solidified wastes causes desorption and resolubilization of lead and chromium.

**Keywords**: Stabilization/Solidification, lead, chromium, Portland cement, setting time, strength, Leach-ability.

## INTRODUCTION

There has been increasing concern in recent years associated with the management and disposal of hazardous industrial wastes and the control of their potential impact on both public health and the environment. This has led to the introduction of waste related laws and regulations in many countries which have controlled the disposal options available for hazardous wastes and made waste producers as well as management companies develop more environmentally safe disposal methods. Consequently there will be significant emphasis on the elimination of hazardous wastes from manufacturing processes and increased reliance on reuse and recycling stabilization/solidification (S/S) processes are potential treatments for the hazardous wastes produced by a range of different industries. Wastes suitable for this form of treatment include many types of industrial sludges and treatment residues which contain high levels of inorganic components but relatively low levels of organics. The technology aims to prevent the release of hazardous components from the solidified wastes after disposal in a landfill by limiting the solubility and mobility of the contaminants This results from the transformation of the waste into a monolithic solid material and the chemical interactions between the waste and the solidification binders or additives. The chemical changes that take place as a result of the interaction between waste components and Portland cement play an important role in controlling the quality of cement-based solidified waste products Il-6].Current

---

solidification processing normally involves simply mixing wastes with binders, and this generally produces relatively poor materials. They are mechanically very weak in comparison with structural concretes and their rnicro structures normally contain high levels of porosity [7]. Slight variations in process formulation or waste composition could induce undesirable effects and produce products with reduced mechanical stability and increased leachability [8]. The leachability of waste constituents from cement-based S/S products after landfilling is the most important factor determining the effectiveness of the treatment process' Leaching of contaminants may occur when cement-based S/S products are in contact with landfill leachate. Several leach testing procedures have been developed to simulate the landfill environment and take into account the monolithic nature of S/S wastes [9]. These tests assess both the short and long-term environmental impact due to leaching of hazardous constituents from S/S treated wastes' In this work, the interfering effects on setting times, strength development and leachability of cement-based solidified waste forms caused by the addition of lead and chromium hydroxide were investigated. Cement-based stabilization is a viable process for treating many potentially hazardous wastes, particularly that containing metallic and metalloid elements. In particular, it provides a very promising solution for the disposal of arsenic bearing wastes  In cement stabilization, water in the waste chemically reacts with OPC to form hydrated calcium silicates and aluminate compounds, while the solids act as aggregates to form a "concrete" [10,11]

## Lead

The primary industrial sources of lead (Pb) contamination include metal smelting and processing, secondary metals production, lead battery manufacturing, pigment and chemical manufacturing, and lead-contaminated wastes. Widespread contamination due to the former use of lead in gasoline is also of concern. Lead released to groundwater, surface water and land is usually in the form of elemental lead, lead oxides and hydroxides, and lead metal oxidation complexes. Lead occurs most commonly with an oxidation state of 0 or +II. Pb(II) is the more common and reactive form of lead and forms mononuclear and polynuclear oxides and hydroxides. Under most conditions $Pb^{2+}$ and lead-hydroxy complexes are the most stable forms of lead [12]. Low solubility compounds are formed by complexation with inorganic ($Cl^-$, $CO_3^{2-}$, $SO_4^{2-}$, $PO_4^{3-}$) and organic ligands (humic and fulvic acids, EDTA, amino acids). Lead carbonate solids form above pH 6 and PbS is the most stable solid when high sulfide concentrations are present under reducing conditions. Most lead that is released to the environment is retained in the soil. The primary processes influencing the fate of lead in soil include adsorption, ion exchange, precipitation, and complexation with sorbed organic matter. These processes limit the amount of lead that can be transported into the surface water or groundwater. The relatively volatile organolead compound tetramethyl lead may form in anaerobic sediments as a result of alkyllation by microorganisms. The amount of dissolved lead in surface and groundwater depends on pH and the concentration of dissolved salts and the types of mineral surfaces present. In surface and ground-water systems, a significant fraction of lead is undissolved and occurs as precipitates ($PbCO_3$, $Pb_2O$, $Pb(OH)_2$, $PbSO_4$), sorbed ions or surface coatings on minerals, or as suspended organic material .[12,13]

## Chromium

Chromium (Cr) is one of the less common elements and does not occur naturally in elemental form, but only in compounds. Chromium is mined as a primary ore product in the form of the mineral chromite, $FeCr_2O_4$. Major sources of Cr contamination include releases from electroplating processes and the disposal of chromium containing wastes. Cr(VI) is the form of chromium commonly found at contaminated sites. Chromium can also occur in the  oxidation state, depending on pH and redox conditions. Cr (VI) is the dominant form of chromium in shallow aquifers where aerobic conditions exist. Cr(VI) can be reduced to Cr(III) by soil organic matter, $S^{2-}$ and $Fe^{2+}$ ions under anaerobic conditions often encountered in deeper groundwater. Major Cr(VI) species include chromate ($CrO_4^{2-}$) and dichromate ($Cr_2O_7^{2-}$) which precipitate readily in the presence of metal cations (especially $Ba^{2+}$, $Pb^{2+}$, and $Ag^+$). Chromate and dichromate also adsorb on soil surfaces, especially iron and aluminum oxides. Cr(III) is the dominant form of chromium at low pH (<4). $Cr^{3+}$ forms solution complexes with $NH_3$, $OH^-$, $Cl^-$, $F^-$, $CN^-$, $SO_4^{2-}$, and soluble organic ligands. Cr(VI) is the more toxic form of chromium and is also more mobile. Cr(III) mobility is decreased by adsorption to clays and oxide minerals below pH 5

and low solubility above pH 5 due to the formation of $Cr(OH)_3(s)$. Chromium mobility depends on sorption characteristics of the soil, including clay content, iron oxide content and the amount of organic matter present. Chromium can be transported by surface runoff to surface waters in its soluble or precipitated form. Soluble and unadsorbed chromium complexes can leach from soil into groundwater. The leachability of Cr(VI) increases with soil pH increases. Most of chromium released into natural waters is particle associated, however, and is ultimately deposited into the sediment [13]

## MATERIALS AND METHODS

**Synthetic Lead and Chromium Hydroxides and cement**
Lead and chromium hydroxides were prepared by precipitation from l M lead nitrate and chromium nitrate solution by adding 10M sodium hydroxide to control the pH of the solution. The slurries of lead and chromium hydroxides were thoroughly mixed to achieve a pH o f 9.5 ± 0.1 and 7.5 ± 0.1. The slurry was vacuum filtered through Whatman No .l filter paper and the filter cake dried overnight a 105ºC before being ground to a particle size of < 500 μ m. The cement used in this work was a normal Portland cement, manufactured by Helwan portland cement t company, Cairo Egypt. The chemical characteristics of the cement are given in Table 1

**Preparation**
Solidified waste samples were prepared by mixing synthetic lead and chromium hydroxides with OPC at 10, 20 and 30 wt %. Water to solid ratio of 0.45 was used to maintain good workability when transferring the sample into a cylindrical plastic moulds. The slurry was mixed following the standard test method ASTM C 305-94 to achieve a uniform distribution of metal waste before being transferred to the plastic mould. The cement solidified metal wastes were allowed to solidify, in the sealed plastic moulds to avoid carbonation prior to testing. 2.3 Time of Setting of Hydraulic Cement by Vicat Needle The standard test method ASTM C 191-92 has been modified to determine the time of setting of cement metal waste mixes' The cement metal waste mixes were prepared at w/s ratio of 0.45, then transferred into the ring and the excess mix was removed. The penetration of the needle was determined every 15 minutes for the control cement paste and every 30 minutes for the cement metal waste mix. The final setting time is obtained when the needle does not sink visibly into the mix.

**Table 1: the chemical composition of (OPC), wt %**

| Component | Cement |
|---|---|
| $SiO_2$ | 21.26 |
| $Al_2O_3$ | 4.79 |
| $Fe_2O_3$ | 3.14 |
| CaO | 64.10 |
| MgO | 2.35 |
| $Na_2O$ | 0.02 |
| $K_2O$ | 0.36 |
| $TiO_2$ | 0.19 |
| $MnO_2$ | 0.04 |
| $P_2O_5$ | 0.03 |
| SrO | 0.03 |
| BaO | 0.04 |
| $SO_3$ | 2.63 |
| Loss on Ingnition | 1.04 |
| Insoluble Residue | 0.11 |
| C3S | 55.2 |
| C2S | 19.3 |
| C3A | 7.4 |
| C4AF | 9.5 |

**Time of Setting of Hydraulic Cement by Vicat Needle**
The standard test method ASTM C 191-92 has been modified to determine the time of setting of cement metal waste mixes. The cement metal waste mixes were prepared at w/s ratio of 0.35.The mix was then transferred in to the ring and the excess mix was removed. The penetration of the needle was determined every 15 minutes for the control cement paste and every 30 minutes for the cement metal waste mix. The final setting time is obtained when the needle does not sink visibly into the mix.

**Unconfined Compressive Strength**
The unconfined compressive strength of the solidified wastes was done following ASTM D1633-96. The size of the cylindrical sample was modified to a diameter of 50 mm. and height of 100 mm. The compressive strength of the solidified waste samples was determined after curing for 1 , 3 , 8 , 15,29,51 and 91 days

**Dynamic Leach Test**
Metal leaching from the solidified wastes has been assessed using a modified ANSVANS 16.1 [14 ]leach test on the samples cured for 28 days .Cylindrical samples (25 mm. diameter and 25 mm. height) were suspended in a plastic net in 0.2N acetic acid solution, at a leachant volume to surface area ratio of 20:1. The leachates were removed to determine the pH and metal concentration and the leachant was replace periodically after intervals of static leaching The leachants were renewed at 1, 8, 15,29 and 57 days. This produces severe leaching conditions and allows assessment of leaching performance over longer time periods.

## RESULTS AND DISCUSSION

**Time of Setting of the Solidified Wastes**
The time of setting of ordinary Portland cement (OPC) in the presence of 10, 20 and 30 wt% of synthetic lead and chromium hydroxides are presented in Figures I and 2. The final setting time of mixes with 10 and 20 wt%. additions of lead hydroxide were 78 and 100 hours compared to 4 hours for control OPC whereas those mixes with 10, 20 and 30 wt% of addition of chromium hydroxide were 5, 6.5 and 7.5 hours respectively. It is noticed that the final setting time of the lead doped OPC is much longer than that of the chromium doped OPC and the final setting had not occurred up to 150 hours of observation when a 30 wt% . of lead hydroxide was added. This suggests that lead hydroxide causes more interference on normal hydration of OPC than chromium hydroxide. Both lead and chromium hydroxides are amphoteric metals which were extensively resolubilized under highly alkali environment of cement and adsorbed onto the hydrating surfaces of cement clinker particles causing hydration retardation [1, 10]. It is possible that the adsorption of hydroxyl lead ion onto the hydrating surfaces of cement clinker particles Leads to the formation of less permeable coatings which cause more severe retardation of normal cement hydration than that of chromium.
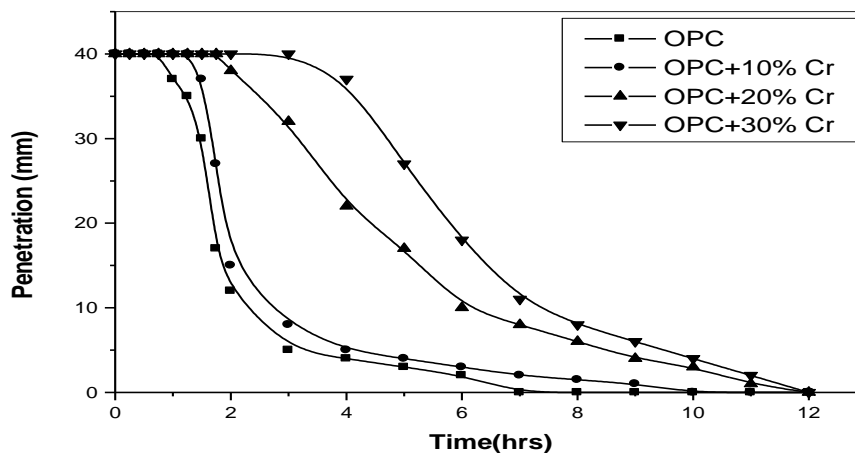


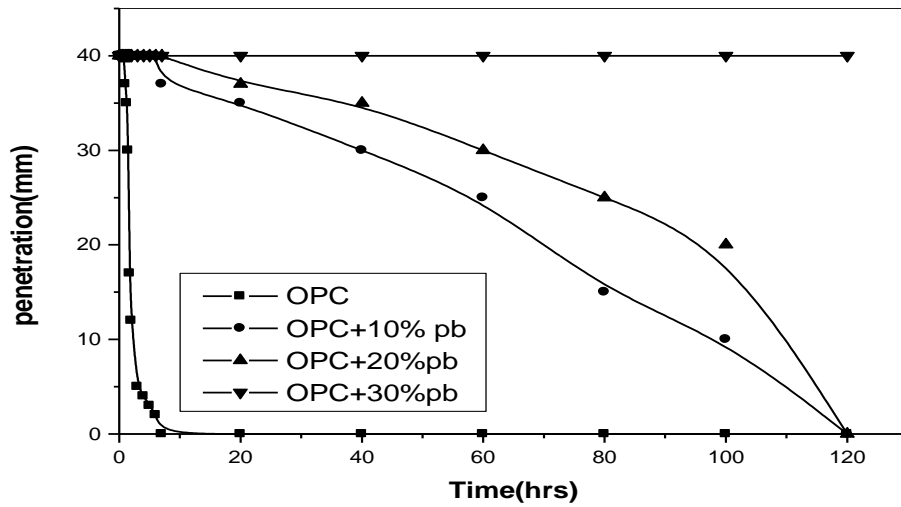**Fig 1:  Time of setting of OPC in the presence of chromium hydroxide**

**Fig 2:  Time of setting of OPC in the presence of lead hydroxide**

**Unconfined Compressive strength**
Strength of the Solidified Wastes (Figures 3 and 4) shows the compressive strength of the solidified wastes doped with 10, 20 and 30 wt% of lead and chromium hydroxides as a function of curing time. The interfering effect of lead and chromium hydroxides on OPC hydration results in a lower rate of strength development of the solidified waste forms compared to control hardened cement. It was found that strength has not been developed during the first day of curing when lead hydroxide was added at l0 and 20 wt % and up to 3 days of curing with 30 wt % addition .It was also noticed that there is a decrease in compressive strength of the solidified waste forms with an increase in the concentration of lead and chromium hydroxides. It is possible that lead and chromium hydroxides which were adsorbed onto the hydrating surface of cement clinker particles were incorporated into the CSH gels. It was reported that hydration of clinkers in the presence of 16 wt. % of lead nitrate induced an increased gel formation [11]. This increased gel formation is associated with volume change in the solidified waste forms which leads to micocraking and as a result, a decrease in compressive strength was observed in Figures 3.4
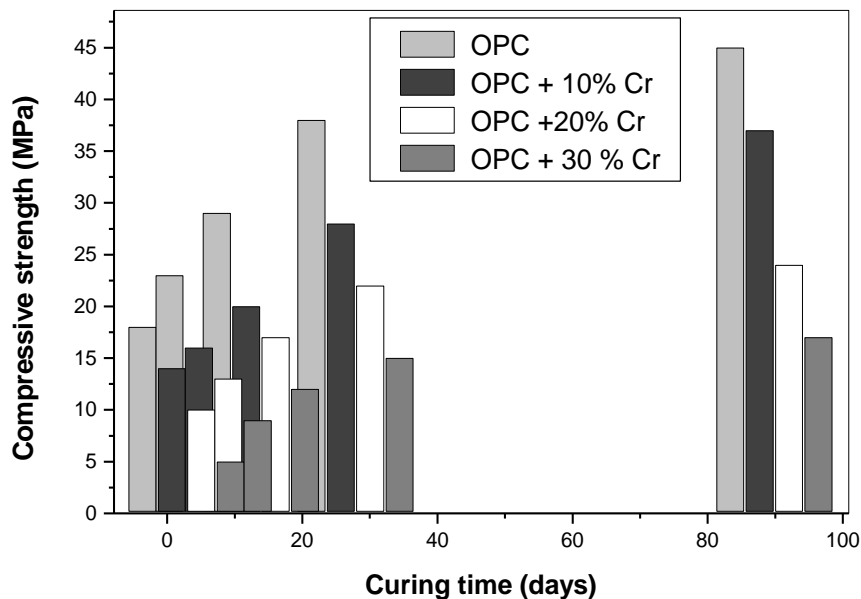


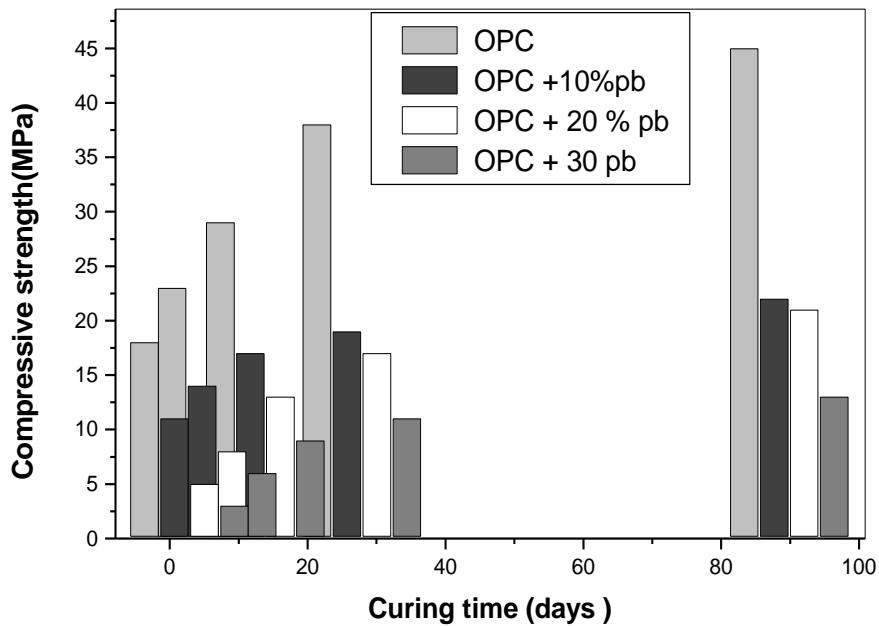**Fig 3:  Compressive strength of the OPC/Cr waste mixes as a function of curing time**

**Fig 4: Compressive strength of the OPC/pb waste mixes as a function of curing time**

**Leachability of Metals from the Solidified Wastes**
Leachability of Metals from the Solidified Wastes Leachate pH of the solidified wastes after each interval of exposure is shown in Table 2

**Table 2: Leachate pHs of the solidified wastes at each interval of exposure**

| Sample | | Leachate pHs | | | | |
|---|---|---|---|---|---|---|
| | initial | Day 1 | Day 8 | Day 15 | Day 28 | Day 60 |
| OPC | 2.9 | 4.2 | 4.7 | 4.6 | 4.6 | 4.6 |
| OPC+10%pb(OH)$_2$ | 2.9 | 4.3 | 4.7 | 4.6 | 4.4 | 4.4 |
| OPC+20%pb(OH)$_2$ | 2.9 | 4.3 | 4.7 | 4.3 | 4.3 | 4.4 |
| OPC+30%pb(OH)$_2$ | 2.9 | 4.3 | 4.7 | 4.2 | 4.3 | |
| OPC+10%Cr(OH)$_3$ | 2.9 | 4.4 | 4.8 | 4.5 | 4.4 | 4.3 |
| OPC+20%Cr(OH)$_3$ | 2.9 | 4.4 | 4.7 | 4.4 | 4.5 | 4.4 |
| OPC+30%Cr(OH)$_3$ | 2.9 | 4.4 | 4.7 | 4.5 | 4.4 | 4.5 |
| | | | | | | |

The cumulative amount of lead and chromium leached from the solidified wastes as a function of exposure duration is presented in Figures 5 and 6. The pH of leachants from control OPC samples changed from an initial pH of 2.9 to approximately between 4.2 and 4.7 at different exposure duration. Similar variations in leachate pH were observed for both lead and chromium doped OPC samples.
 An increase of leachant pH is a result of dissolution of calcium hydroxide which is produced in large quantities during the hydration reactions of OPC.
Calcium hydroxide and the high pH of the pore water provide a buffering capacity to the solidified waste forms against acid attack [15]. The cumulative amounts of lead and chromium leached from the solidified wastes in the presence of 10, 20 and 30 wt %o of lead and chromium hydroxides after leaching for 57 days were 688,1 , 438, 3, 548 and 2l, 48, l 5 l mg/l respectively. Metal hydroxides are amphoteric metals and their solubility are strongly dependent on leachate pHs [16].
Lead and chromium hydroxides have minimum solubility around pH 9.5 and 7.5 whereas leachate pHs of the solidified wastes were between 4.4 and 4.8. The difference between minimum solubility of lead hydroxide and leachate pH is large compared to that of chromium hydroxide.

As a result, lead was released from the solidified wastes at a higher rate than chromium. It is also possible that lead hydroxide causes more severe hydration retardation than chromium hydroxide and these results in poor microstructure development of the solidified wastes which contain a high level of porosity.

During leaching tests of monolithic samples the ingress of the acetic acid leachant through the open and connected porosity leads to a reduction in the pH of the internal pore water causing desorption and resolubilisation of heavy metals.
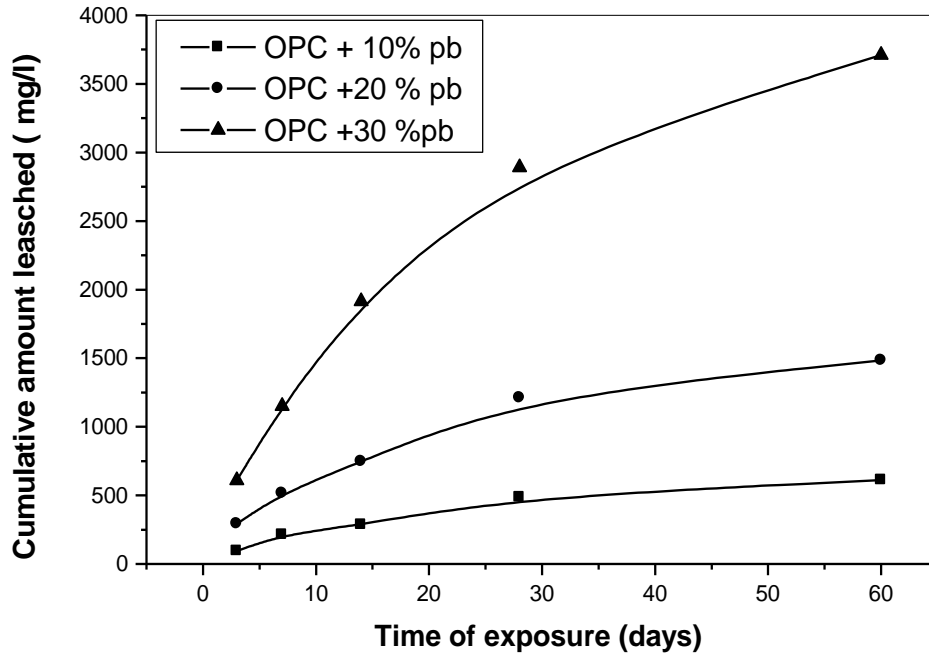


**Fig 5: Cumulative amount of pb leached after exposure to 0.5 acetic acid leachant as function of time exposure**
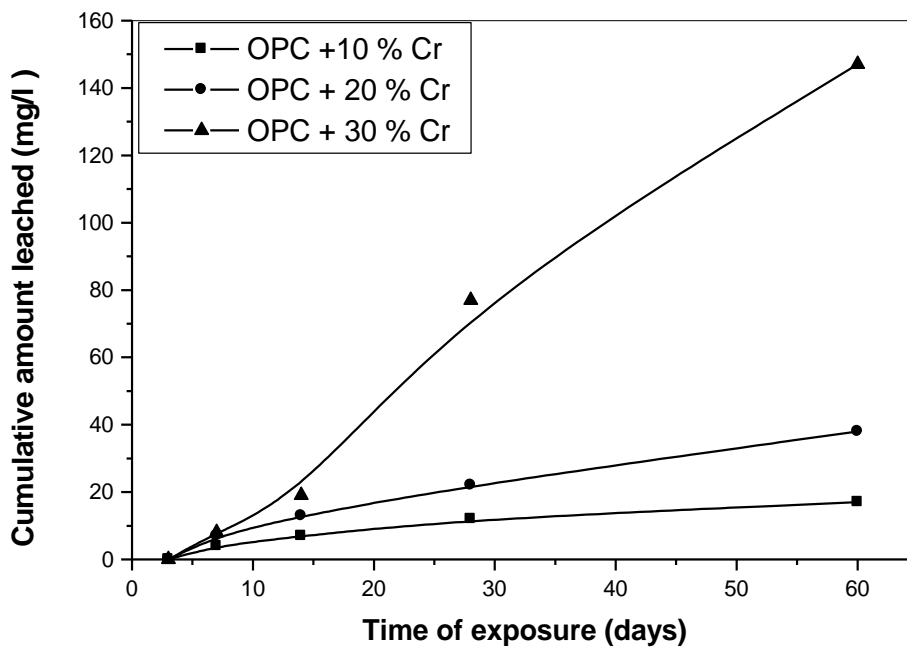


**Fig 6:  Cumulative amount of Cr leached after exposure to 0.5 acetic acid leachant as a function of time exposure**

## CONCLUSIONS

The following conclusions can be drawn from this work:
1.  Lead hydroxide causes more severe hydration retardation than chromium hydroxide as is indicated by the longer final setting time and lower rate of strength development of the solidified wastes.
2.  The interfering effects caused by the addition of lead and chromium hydroxides increase with the contents addition of heavy metals
3.  Lead and chromium hydroxides interfere with the normal cement hydration by adsorptions onto the hydrating surface of cement clinker particles and thus reducing the inward diffusion of water to the cement grains.
4.  Compressive strength of the solidified wastes decreased with waste loading. Although strength requirements for solidified wastes are not as important as those for structural concretes, failure to obtain adequate strength is an indicator of a poor microstructure and may be expected to lead to increase leaching.
5.  Leaching of the amphoteric lead and chromium from the solidified wastes is strongly dependent on leachate pH.

## REFERENCES

1.  Ibplecas and Sdimovic 2004 "Immobilization of industrial waste in cement–bentonite clay matrix " Mater. Sci., Vol. 27, No. 2,  pp. 175–178. © Indian Academy of Sciences .
2.  Wang, S.and Vipulanandan, C. (2000) "Solidification/Stabilization of Fe(II) Treated Cr(VI) Contaminated Soil." Environmental Engineering Science 8(5): 301-308.
3.  Hills,C.D., Koe,L.,Sollars,C.J.and R.Perry,(1992).Early Heat of Hydration During the Solidification of a Metal Plating Sludge,Cement and Concrete Research,Yol.22,pp.822-832,
4.  Barna, R., Rethy, Z., and Tiruta-Barna, L.(2005) ."Release dynamic process identification for a cement based material in various leaching conditions. Part I.Influence.of.leaching conditions on the release amount".J. Environ. Manage.74: 141–151.
5.  Jang A. and Kim I., December (2000) "Solidification and stabilization of Pb, Zn, Cd and Cu in tailing wastes using cement and fly ash, Minerals Engineering, "Volume 13, Issues 14-15, , Pages 1659-1662.
6.  Silveira B., Dantas A., Blasques J. and  Santos R.,  March (2003)" Effectiveness  of cement-based  systems  for  stabilization  and solidification of spent  pot  liner inorganic  fraction ", Journal  of Hazardous  Materials, Volume 98,  Issues 1-3, 17, Pages 183-190.
7..  Santanu Paria and Pak Yuet K. (2006) "Solidification–stabilization of organic and inorganic contaminans using Portland cement" Environ. Rev. 14(4): 217–255 NRC Canada .
8.  A. Osmanlioglu,  (2002) "Immobilization of radioactive waste by cementation with purified kaolin clay, "Waste Management, Volume 22, Issue 5, , Pages 481-483.
9.  Nina Bednarsek" (2005-2006) An investigation of solidification / stabilization treatment on petroleum hydrocarbon – contamination sand"Cranfield University MSc Environmental Diagnostics Academic year .
10.  Leist, M., Casey, R.J.,and Caridi, D.(2003)." Evaluation of leaching  tests  for cement based immobilization of hazardous   compounds". J. Environ. Eng. 129: 637–641.
11.  Yukselen, M.A., and Alpasalan, B. 2001." Case study-leaching of metals from soil contaminated by mining activities." J. Hazard. Mater. B87: 289–300.
12.  karamalidis Athanasios K.; voudrias Evangelos A (2009). "Leaching and Immobilization Behavior of Zn and Cr from Cement-Based Stabilization/Solidification of Ash Produced from Incineration Environmental engineering science   ISSN 1092-8758 , vol. 26, no1, pp. 81-96
13.  Appel,C.and L.Ma. (2002).Concentration, pH, and surface charge effects on cadmium and lead sorption in three tropical soils. Journal of Environmental Quality.Vol.31,pp 581-589
14.  American Nuclear Standards Committee. (2003)." Measurement of the leachability of solidified low-level radioactive wastes by a short-term test procedure". ANSI/ANS 16.1.
15.  Go˜ni S., Guerrero A., Lorenzo M.P. (2006)"Efficiency of fly ash belite cement and zeolite matrices for immobilizing cesium" Journal of Hazardous Materials B1371608–1617
16.  Athanasios K. Karamalidis, Evangelos A. Voudrias (2009) "Leaching and Immobilization Behavior of Zn and Cr from Cement-Based Stabilization/Solidification of Ash Produced from Incineration of Refinery Oily Sludge "Environmental Engineering Science., 26(1): 81-96.

# UTILIZATION OF USED-ENGINE OIL IN CONCRETE AS A CHEMICAL ADMIXTURE

**\* Dr. Gamal Elsayed Abdelaziz**

*Associate Professor, Faculty of Engineering in Shoubra, Benha University, Egypt*
*E-mail: abdelazizge@yahoo.co.uk*

## ABSTRACT

As an attempt for reducing the harmful impacts of throwing the used-engine oil (UEO) in the environment on marine, human and underwater lives and agriculture production, this study have been undertaken, aiming to adopt such waste material in concrete industry as a chemical admixture. Therefore, an experimental program was designated initially to investigate the effectiveness of UEO on the various fresh properties of concrete (consistency, rate of slump loss, setting time and air content). The performance of concrete containing UEO in its hardened state was then thoroughly studied, through assessing the various mechanical and microstructure-related properties, namely, 28 day-compressive strength, surface hardness, homogeneity, sorptivity, porosity and degree of hydration. Ten OPC concrete mixes and another ten OPC paste mixes made with different contents of UEO, water reducing admixture and air-entraining admixture (0, 0.15, 0.30 and 0.60%, by cement mass) were consequently prepared. The results showed that utilizing of UEO in OPC mixes has reasonably altered its fresh parameters, where, an increase in initial slump and air content, and a decrease in rate of slump loss and initial setting time were found. A slight reductions in the 28-day compressive, homogeneity, density and degree of hydration, and an increase in porosity and rate of water inflow into cover zone were noted when UEO was induced into OPC mixes. The results also indicated that the fresh and hardened characteristics of OPC concretes containing either UEO or air entraining admixture are comparable.

**Keywords :** Waste Materials, Used-Engine Oil, Environmental Impacts, Admixtures.

## INTRODUCTION

There is a current trend all over the world to investigate the utilization of processed and unprocessed by-products and domestic wastes as raw materials in concrete, as components of concrete binder, as aggregates, a portion of aggregate, or ingredients in manufactured aggregates. Some wastes can be used as chemical admixtures and additives, which can alter the fresh and hardened properties of concrete [1]. However, successful use of industrial by-products or wastes in concrete depends mainly on the requisite properties of the end product. Several by-products or wastes have been reported in literature to be used in concrete and construction industry; such as recycled concrete aggregate, pozzolans, fly ash, blast furnace slag, silica fume, rice husk ash, waste-derived fuels, organic fiber materials, etc [2].

It is estimated that less than 45% of the used-engine oil is being collected worldwide while the remaining 55% is thrown by the end user in the environment. The discharge of used oil can become a serious problem or a valuable resource depending upon how it is managed. Simply reflect on the fact that one oil change contains four quarts of foils, which when improperly disposed of sufficient to ruin one million gallons of fresh water, which in turn adversely impacting human life, fish and plant life [2,3]. So, in this context, the proper management of used oil is essential to eliminate or minimize potential environmental impacts.

Historically, reference books on concrete technology and cement chemistry indicated that the leakage of oil into the cement in older grinding units has led to a greater resistance to freezing

and thawing, which led few researchers in two separate studies to adopt and utilize used-engine oil (UEO) in concrete mixes. They have added UEO to concrete mix ingredients aiming to obtain a similar effect to that reported from using air entraining admixture in concrete mixes [1,4]. Hamad et al [1] have therefore investigated the effects of UEO on the fresh hardened properties concrete. Their preliminary results showed that UEO increased the slump, and % air of fresh concrete, and not adversely affect the compressive strength of hardened concrete. Hamad and Reteil [4] found that UEO did not have significant effect on the structural behavior of reinforced concrete elements, where the ultimate load or load deflection diagrams have not been altered due to adding UEO to concrete mix ingredients.

The efficiencies of used-engine oil and new-engine oil on improvement of properties of fresh concrete and hardened concrete have been recently investigated by Shafiq et al [5]. Their results showed that the used-engine oil increased the slump between 18 to 38% and air content between 26 to 58% with respect to the control mix containing no admixture. Used engine oil reasonably reduced the porosity and did not adversely affect the strength properties of concrete. They also found that the performance of concrete made with either UEO or new-engine oil were more or less similar. This means that UEO behaved as a chemical plasticizer and air entraining admixtures in concrete as the fluidity and air content of concrete have been increased with adding UEO to concrete mix. However, this hypothesis has to be backed with an experimental proof.

## RESEARCH SIGNIFICANCES

It is apparent that not all fresh and hardened properties of concrete incorporating UEO have not been thoroughly investigated and understood yet. Where, there is still a lack of knowledge regarding the impacts of UEO on rate of setting, rate of fluidity loss, homogeneity, and microstructure-related characteristics (degree of hydration, porosity and rate of fluid transport into cover zone). Moreover, there is a need to a comparative study to understand the main differences or coincidence between the various properties of concrete made with UEO and with the corresponding of that made with traditional-chemical admixture (plasticizer and air-entraining). Clarifying such aspects is essential prior to recommending such waste material in concrete industry.  Consequently, the main objectives of this study can be summarized as follows:

1- To clarify the impacts of used-engine oil (UEO) on air content, consistency, initial setting time and rate of fluidity loss of concrete.
2- To investigate the compressive strength, surface hardness, homogeneity, and microstructure related properties (hydration, porosity and sorptivity) of OPC concrete made with different contents of UEO.
3- To compare between the behaviors of concretes made with either UEO or traditional-chemical admixtures (namely, water-reducing and air-entraining) during their fresh and hardened state.

## EXPRIMENTAL PROGRAM

Ten OPC concrete mixes and another ten OPC paste mixes were prepared. The variables in these mixes include admixture type and dosage of admixture. Two chemical admixtures were adopted in these mixes, namely, water-reducing admixture (WR) complies with ASTM C 494-81 Type A and BS 5075 Part 1 and air-entraining admixture (AE) complies with ASTM C 260- 81 and BS 5075 Part 2. Used engine oil (UEO) was also utilized in these mixes as an admixture. The used UEO was collected from different vehicles service station in Cairo. The chemical analysis of the used UEO is listed in Table 1. Four dosages for each used admixture were regarded (control, 0.15, 0.30 and 0.60, % by weight of cement).  Constant water cement ratio of 0.50 was used for cement paste and concrete mixes.

**Table 1: Chemical analysis of UEO**

| Sulfate, mg/g | Lead, mg/kg | pH value |
|---|---|---|
| 4.15 | o.45 | 7.10 |

For concrete mixes, constant weights of washed-natural desert sand of 700 kg/m³ and natural gravel of 1070 kg/m³, complying with ASTM C 33 and ESS 1109/2002 requirements, were used. Constant weight of Local OPC (400 kg/m³), complying with BS 12 (1978), EN 197-1, ESS 5325 (2005) and ASTM C618 (1992), was used. The chemical composition of the used cement (OPC) and physical properties of the used aggregate are represented in Tables 2 and 3, respectively.

The initial setting time of OPC mixes made with or without these above-mentioned admixtures were also measured, using Vicate apparatus, and the results will be demonstrated in the next section.

Mixing of concrete ingredients was performed in the laboratory (20 ± 2°C and 65% RH), using a 100 liter capacity concrete mixer. Dry ingredients of concrete mix were initially mixed for one minute prior to adding the mixing water. Admixtures such as UEO, WR and AE were diluted in water before it was added to the dry ingredients in the mixer. Water was then added to dry mixture of cement and aggregate and mixed for another two minutes, which were enough periods for producing homogenous concrete.

**Table 2: Chemical composition of OPC**

| SiO$_2$ | AL$_2$O$_3$ | Fe$_2$O$_3$ | CaO | MgO | Na$_2$O | K$_2$O | SO$_3$ | LOI | Insoluble residue |
|------|------|------|------|-----|------|------|------|-----|-----------|
| 20.1 | 4.3 | 3.8 | 61.1 | 1.7 | 0.4 | 0.19 | 3.6 | 3.8 | 0.90 |

**Table 3: Physical properties of gravel and sand**

| | Maximum aggregate size, mm | 24-hour water absorption, % | Specific gravity | Fineness modulus | Unit weight, kg/m³ |
|--------|------|------|------|------|------|
| Gravel | 20 | 0.50 | 2.50 | - | 1570 |
| Sand | - | 0.66 | 2.66 | 2.59 | 1590 |

Immediately after mixing, the initial slump values were measured for all concrete mixes in accordance with BS 1881: Part 102 (1983) and air content was quantified in accordance with the method B described in BS 1881: part 106: 1983 and ASTM- C 173. The values of instant slump at different elapsed times from the end of mixing process, 30, 60, 120 and 240 minutes, were also recorded, to assess the rate of slump loss of concrete (fluidity loss). Meanwhile, ten cube specimens (150 mm) were taken from each concrete mix, demolded, cured in water for 27 days.  Five specimens were allocated for measuring the surface hardness, homogeneity, density and compressive strength of concrete, while, the other five specimens were designated for sorptivity test.

The surface hardness and homogeneity of specimens were then examined at age of 28 days, using Schmidt hammer of type N and ultra-sonic pulse velocity according to BS 1881 Part 201 and ASTM C 805, respectively. This was followed by determining the compressive strength, according to BS 1881: Part 116: 1983 and BS 1881: Part 121: 1883. An average of five measurement values for each tested property was then obtained. Prior to compressive strength test, the cubes were used to test the SSD density following BS 1881: Part 114: 1983.

For determining the sorptivity, the surfaces of designated concrete specimens were exposed capillary absorption test, as described earlier by McCarter et al [6]. The sorptivity of concrete specimens were then calculated using the data recorded from capillary absorption test, using the same test procedures and mathematical expression used by Hall [7] and Claisse et al [8]. Hall [7] has defined the sorptivity (S) as the slope of the cumulative volume of water absorbed per unit area (i) against the square root of time (t), using the following Equation. Each reported test data point is the mean of the results for five specimens.

$$i = a + St^{0.5} \qquad \dots\dots\dots\dots(1)$$

To determine the porosity and degree of hydration of OPC matrices containing the above-mentioned admixtures, % of evaporated water (EW) and % of non-evaporable water (NEW) of hardened OPC paste were assessed, respectively, following the same approach suggested in literature [9,10,11,12] . So, ten OPC paste mixes incorporating different dosages of UEO, WR

and AE admixture (0, 0.15, 0.30 and 0.60 %) AE were prepared. Five disc samples of 25 mm thickness and 50 mm height were taken from each cement paste mix, and then cured in water till the age of testing (28 days). After curing, the saturated-surface dry weight of each disc specimen was weighted ($W_1$), followed by oven-drying the specimen at 105ºC and 950 ºC. Constant weights of each specimen at 105ºC ($W_2$) and 950 ºC ($W_3$) were recorded. % EW and NEW were then approximately estimated, using the following Equations 2 and 3, respectively. Each reported test data point is the mean of the results for five samples.

$$\%EW = 100 \ (W_1-W_2)/W_2 \qquad ........(2)$$
$$\%NEW = 100 \ (W_2-W_3)/W_2 \qquad ........(3)$$

The %EW represents the amount of free water (unbound water) existed in pores of OPC matrix, which in turn it can be considered in this study as an indicative measure for the amount of interconnected pores (porosity) in concrete [10]. While, %NEW was adopted to provide an indicative measure for the amount of bound water in OPC matrix, existed in OPC hydration products, where all hydration products approximately decompose when it is exposed to a high elevated temperature of 950 ºC [12].

## RESULTS AND DISCUSSION

### Fresh Properties
Effect of inducing used engine oil (UEO) into OPC mixes, as an admixture, on their initial slump and air content are illustrated in Figs. 1 and 2, respectively.  A comparison between the effects of traditional chemical admixtures, namely, water reducer (WR) and air entraining (AE), and UEO on these parameters was also shown. As seen from Fig.1, the initial slump of OPC concrete increases with increasing the dosage of UEO induced in OPC mixes. The amount of increase reaches 25, 75 and 110%, compared to the corresponding of OPC made without admixture (control mix).

The effect of UEO on initial slump seems to be nearly close to that obtained when a traditional chemical admixture (water-reducing admixture, WR) was used. Consequently, utilization of UEO has a beneficial role on enhancing the consistency of concrete. This confirms the findings reported earlier by Shafiq et al [5], whom found that the enhancement in slump value with the addition of used-engine oil was in the range of 15 to 54%.
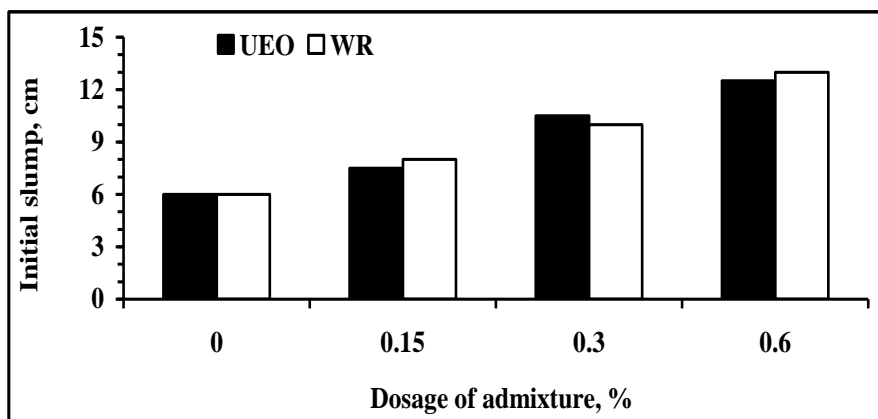


Fig.1: Initial slump of OPC mixes made with either UEO or WR.

As noted from the results in Fig. 2, UEO can also alter the air content of fresh concrete, where, the % of air content increased by about 5, 10 and 25% as a result of inclusion 0.15, 0.30 and 0.60% UEO in OPC mix, respectively, compared to that of control mix. However, this effect is not comparable with that noted when OPC mixes were admixed with air-entraining admixture (AE), where, the air content of concrete was significantly increased with adding AE to OPC mix by amounts reach 30, 65 and 80%, as a result of utilizing 0.15, 0.30 and 0.60% AE, respectively.
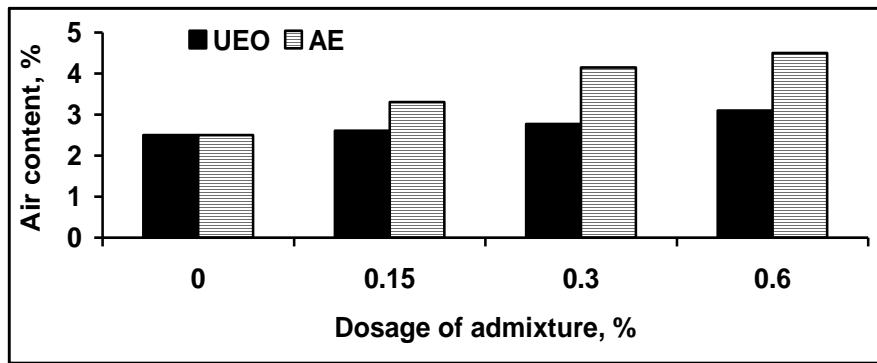
**Fig. 2: Air content of OPC mixes made with either UEO or AE.**

Moreover, the effects of UEO and traditional-chemical admixtures (WR or AE) on the initial setting time of OPC mixes were also investigated, and the results are plotted in Fig. 3. The results affirms that UEO has a significant effect on reducing the value of setting time, where the initial setting time of OPC mixes made with 0.15, 0.30 and 0.60% UEO reach  120, 110 and 90 minutes, respectively, while the corresponding of that mix made without admixture reaches 150 minutes. It also seems from the results plotted in Fig. 3 that the values of initial setting time of OPC mixes made with WR and AE are fairly close to each other, and not comparable with those made with UEO. So, it can be stated that utilizing of UEO in OPC concrete mixes can reasonably alter their consistency, compactability and rate of setting, as verified from the results established in Figs. 1 to 3.
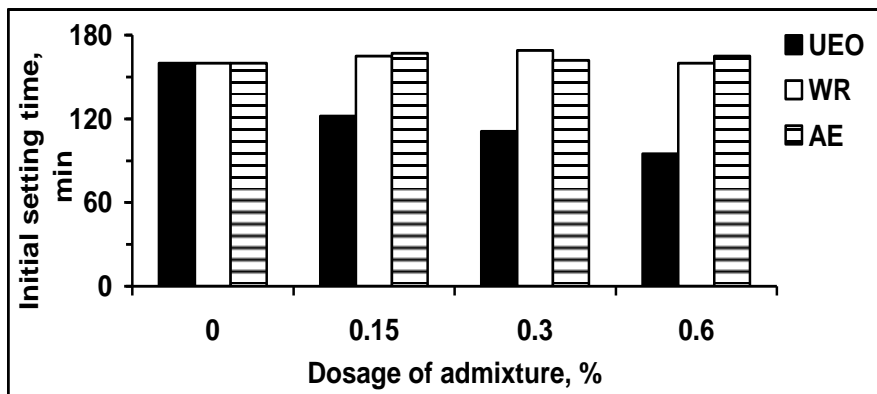


**Fig. 3: Initial setting time of OPC mixes made with various admixtures.**

The question arises from the above discussion is; would such beneficial effect of UEO on the consistency of concrete remain at later elapsed periods? The answer to this arisen question would provide a good understanding to the properties of OPC concrete during its casting and placement state. Determining the rate of loss in fresh properties of concrete is imperative for concrete technologists and engineers on site in order to specify the suitable period between mixing and casting.

So, the instant slump of OPC concrete containing different dosages of UEO (0.0, 0.15, 0.30 and 0.6%) were studied at different elapsed periods from mixing (EP), 0, 30, 60, 120 and 240 minutes.

The results of this investigation are shown in Fig. 4, where the % values of relative slump (instant slump/initial slump) were plotted against EP. As seen, % of relative slump dramatically decreases with increasing EP for all investigated mixes. Rate of decrease in the % of relative slump increased with increasing the dosage of UEO. In other words, inclusion of UEO into OPC mix can lead to increase its rate of slump loss (fluidity loss). These results agree with those reported in Fig. 3, where the setting time was noted to be decreased with increasing UEO content, thus leading to increase the rate of slump loss (fluidity loss).
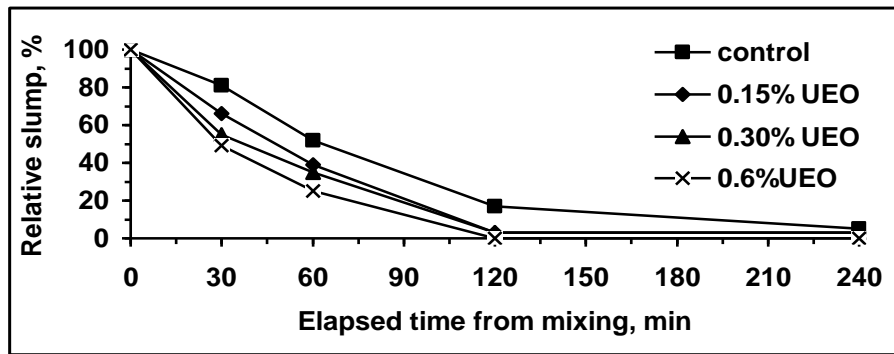
**Fig. 4: Rate of slump loss of OPC concrete mixes made with different contents of UEO.**

The rate of slump loss of mixes containing 0.30% UEO was compared with that of mixes made with either 0.30% WR or 0.30% AE, as illustrated in Fig. 5.  It can be seen that, at  one hour from mixing, the % of relative slump for all considered mixes containing UEO and traditional-chemical admixtures are almost similar, and lower than that of control mix, where the % of slump loss reach 65 and 45%, for mixes made with admixtures and without admixtures, respectively. After an hour from mixing, the mixes containing UEO started to loose its fluidity more rapidly than that for mixes admixed with WR and AE.  However, the rate of slump loses of mixes incorporated with traditional-chemical admixtures (WR and AE) appeared to be comparable with that of control mix.
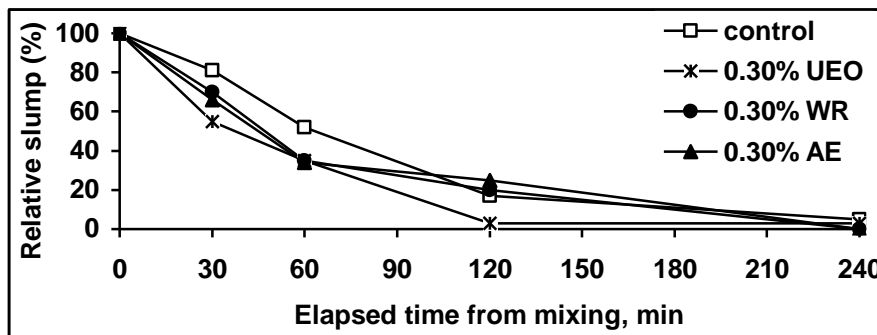


**Fig. 5: Rate of slump loss of OPC mixes made with different admixture types.**

To sum up, utilization of used-engine oil (UEO) resulted in a significant alteration in the performance of OPC concrete during its fresh state. UEO decreases the initial setting time and increases the consistency, air content and rate of fluidity loss of OPC concrete. These effects increased with increasing the dosage of UEO in OPC mixes. Therefore, UEO behaved as a chemical admixture and its uses would provide the dual action for plasticizer and air-entraining admixtures. However, a further rhyeology study is required to understand the mechanism of such waste material on fresh parameters of OPC concrete and then clarifying this phenomenon.

**Hardened Properties**
It is comprehensible from the above discussion that, utilizing UEO as an admixture has reasonable impacts on the various characteristics of concrete during its fresh state. Consequently, an imperative question may be arisen, would these impacts accompany with alterations in the various properties of concrete during its hardened state? As a result, the experimental program was conducted to investigate the mechanical, homogeneity and microstructure-related characteristics of OPC concrete made with different dosages of UEO. The mechanical property was examined as a function of compressive strength and surface hardness of concrete. While, microstructure-related characteristics of concrete were assessed by studying their porosity (EW), degree of hydration (NEW) and rate of water flow into cover zone using sorptivity approach. These above-mentioned properties were also evaluated for

OPC concrete made with traditional-chemical admixtures (WR and AE) and were then compared with those of OPC concrete made with UEO.

**Mechanical characteristics**
Figs. 6 and 7 show 28-day compressive strength and surface hardness of OPC concrete incorporated with various dosages of UEO, WR and AE (0, 0.15, 0.30 and 0.60, % by cement mass. As seemed from the results reported in Fig. 6 that inducing of UEO into OPC could slightly decrease the 28-day compressive strength. The amount of decrease reaches about 5, 8 and 15%, when a dosage of 0.15, 0.30 and 0.60% UEO was utilized, respectively, compared with that of control specimens. Similar effect but with a slight extent was noted when AE was utilized, where the amount of reduction in the compressive strength attained 5 to 10%. Whilst, an opposite effect was not found when WR was used, where the compressive strength was slightly enhanced as a result of adding WR to OPC mix.
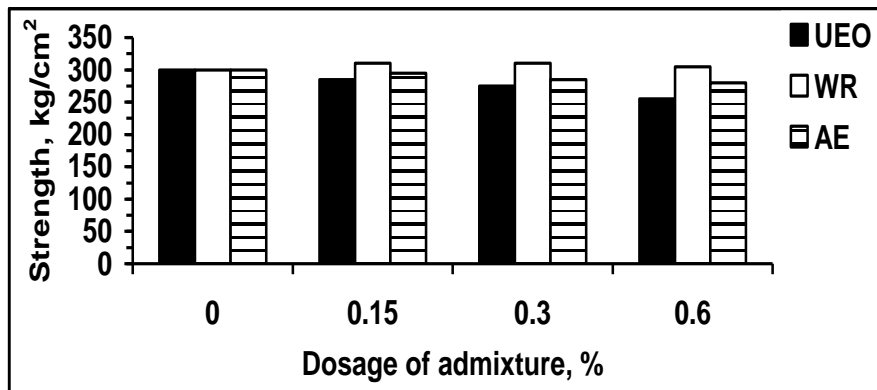


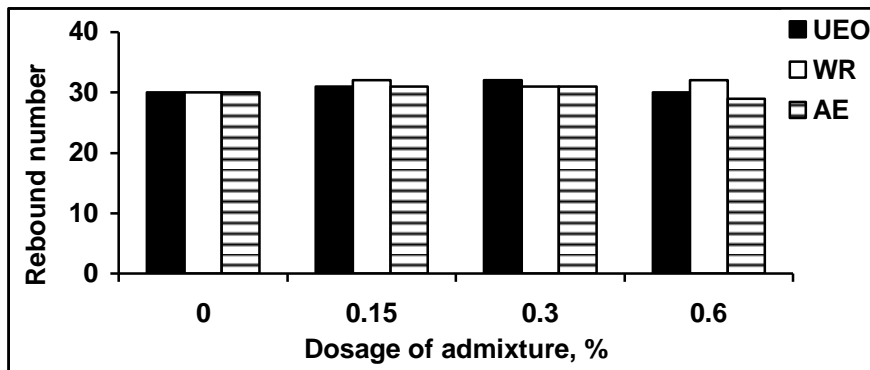**Fig. 6: 28-day compressive strength of OPC concrete made with various admixtures.**



**Fig. 7: Hardness of OPC concrete made with various admixtures.**

These results however, disagree with the findings obtained by Hamad et al [1] and Shafiq et al [5], whom revealed that UEO maintained the compressive strength whereas the chemical air-entraining admixture caused approximately 50% loss in compressive strength. Despite of this contradictory, they reported that the other mechanical properties were significantly adversely affected by utilization UEO or AE in OPC mixes, where they found UEO resulted in average losses of 21, 17 and 6% in the values of flexural strength, splitting tensile strength and modulus of elasticity. The corresponding losses when AE was used 33, 42 and 35%, respectively [1].
On the other hand, the results illustrated in Fig. 7 emphasize that the UEO insignificantly affected the surface hardness of concrete, where, the rebound number measurements (taken by Schmidt Hammer apparatus at age of 28 days) vary from 30 to 32. Similar effects were noted when traditional-chemical admixtures was utilized. However, there is a contradiction between the impacts of UEO on surface hardness and compressive strength. This may be arisen from the difference between the sensitivity of both approaches used in this study for tracing such impacts.

**Homogeneity and density**

The homogeneity of concrete containing such waste material (UEO) or traditional chemical-admixtures was investigated using ultra-sonic pulse velocity (UPV) approach, and the results of such investigated are shown in Fig. 8. As shown, the homogeneity of concrete is slightly reduced as a result of inducing UEO into OPC mix. The amount of reduction reaches 5, 10 and 15%, when 0.15%, 0.30 and 0.60% UEO were used, respectively. These reductions are nearly similar with that produced for specimens made with AE. An opposite effect was produced when WR was used, where the value of UPV of OPC concrete was enhanced by about 5 to 10%, compared to control specimen. These behaviors are generally close to that obtained earlier when the compressive strength of specimens made with such admixtures was regarded, see Fig. 6.
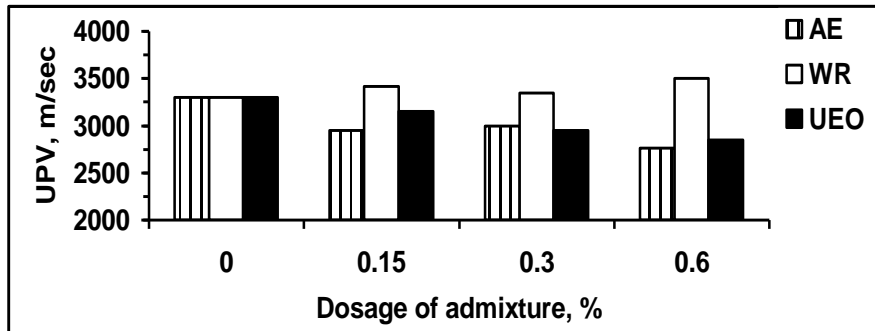


**Fig. 8: Ultrasonic-pulse velocity of OPC concrete made with various admixtures.**

Fig. 9 demonstrates the saturated unit weight of OPC concrete made with different admixture types (UEO, WR and AE). Slight reduction in the density of OPC concrete was noted when OPC concrete was admixed with either UEO or AE. These reductions are in concurrent with that noted reductions in the compressive strength and homogeneity characteristics see the results reported in Figs. 7 and 8. On the other hand, the density of OPC maintained unvaried when WR admixture was induced into its mix.  These above-mentioned effects may be attributed to the significant role of UEO and AE on altering the % air content, which in turn would affect the hardened properties of concrete [13].
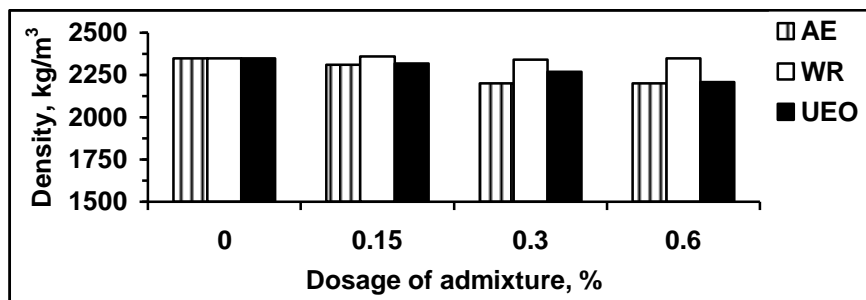


**Fig. 9: Saturated unit weight   of OPC concrete made with various admixtures.**

**Microstructure-related characteristics**

It is clear from the above discussion that, incorporating UOE in OPC mixes can alter most of investigated engineering properties, strength, homogeneity and density. However, there is no available scientific explanation in literature to understand this phenomenon. Therefore, the % of evaporable water (EW) and % of non-evaporable water (NEW) of OPC matrix was investigated to clarify the impacts of UEO on its microstructure-related characteristics, porosity and degree of hydration, respectively. The rate of water inflow into the cover zone was also elucidated to determine the absorptivity of such concrete, which is mainly dependent on the pore structure of surface zone of concrete. Investigating these characteristics could provide a clear image to the influences of UEO on microstructure of concrete, which in turn, have an effect on concrete properties during its hardened state.

Therefore, effects of UEO on %EW and %NEW of hardened cement paste, using thermo-gravimetric analysis approach, were examined, and the results are plotted in Figs. 10 and 11, respectively. A comparison between the effects of UEO and the other traditional-chemical admixtures (WR and AE) on these properties was also presented. As seen, the porosity of OPC matrix (represented by % EW) significantly increases with increasing the dosage of UEO in OPC matrix, and the amount of increase in porosity vary from 20 to 25%. This means that the inclusion of UEO into OPC matrix can alter its microstructure to a more porous structure, hence leading to reduce its mechanical, homogeneity and density characteristics, as verified from the results illustrated shown in Figs. 6, 8 and 9.

A similar effect but with slight extent was noted when the impact of UEO on the degree of hydration (characterized by % NEW) was determined, see Fig. 11. The amount of reduction in % NEW attained about 10%, when 0.60% UEO was used, which resulted in  an increase in the amount of pores in OPC matrix and consequently an increase in its porosity, thus affecting the hardened properties of concrete. The results reported in Figs. 11 and 12 also emphasize that the role of UEO and AE on the micro structural-related characteristics (porosity and degree of hydration) are fairly comparable. Where, % EW increases and % NEW decreases with inducing AE into OPC mixes. These impacts however, disagree with that produced when WR admixture was utilized, where; %EW and %NEW approximately remain unvaried as a result of using WR.
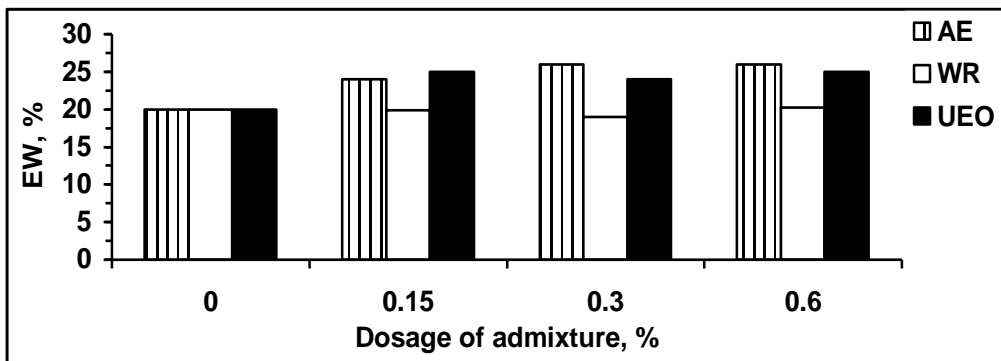


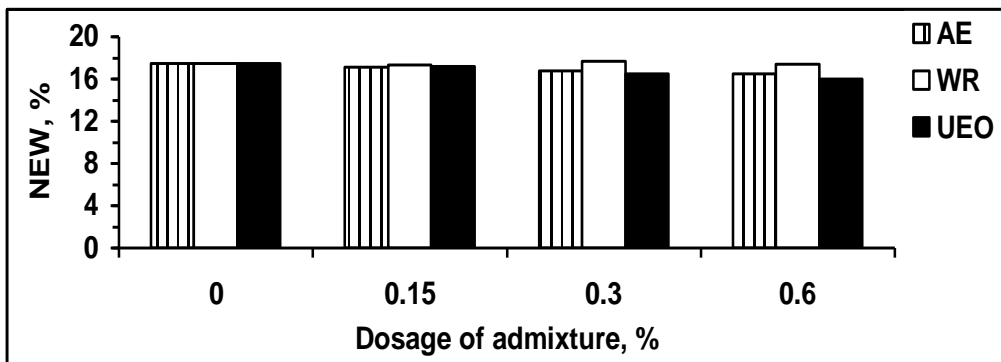**Fig. 10: Amount of evaporable water in of OPC hardened cement paste made with various admixtures.**



**Fig. 11: Amount of non-evaporable water in of OPC hardened cement paste made with various admixtures.**

The rate of water inflow into cover zone of OPC concrete containing such admixture types was investigated as a function of its sorptivity to assess its mass transport property and hence microstructure characteristics.  The results of this investigation are shown in Fig. 12. As seen, the sorptivity of OPC concrete proportionally increases with utilizing either UEO or AE. On the other hand, the sorptivity of OPC concrete was reduced with the addition of WR admixture, and the amount of reduction increases with increasing the dosage of WR. This may be attributed to the enhancements occur to porosity and degree of hydration of OPC matrix, as indicated from the results shown in Figs. 10 and 11.
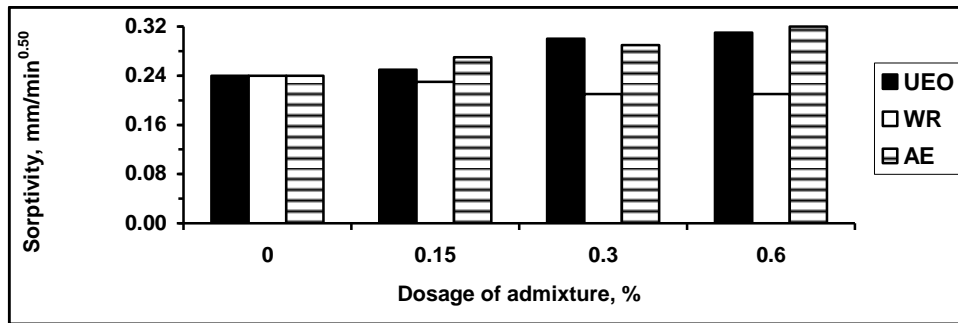
**Fig. 12: Sorptivity of OPC concrete made with various admixtures.**

The results reported in Fig. 12 verify that inclusion of either UEO or AE into OPC mixes may lead to increase the amounts of fluid pathways and interconnected pores in cover zone, which resulted in an increase in their sorptivity values. In other words, utilization of UEO in concrete industry may influence micro structural- related characteristics. However, a further microstructure analysis study has to be performed to confirm such explanation and to provide more information about pore size distribution, capillary pores and nature and amount of hydration of OPC matrix containing such waste material (UEO). The impacts of UEO on the various hardened properties of concrete would be then simply clarified and understood.

## CONCLUSIONS

Based on the results and discussion, the following conclusions were made:

1. Utilization of used-engine oil (UEO) resulted in a significant alteration in the performance of OPC concrete during its fresh state. UEO decreases the initial setting time and increases the consistency, air content and rate of fluidity loss of OPC concrete. These effects increase with increasing the dosage of UEO in OPC mixes. Therefore, UEO behaved as a chemical admixture and its impacts would provide the dual action of both plasticizer and air-entraining admixtures.

2. Inducing UEO into OPC mixes has a reasonable influence on the microstructure-related characteristics of hardened OPC matrix. Where, increasing the dosage of UEO resulted in an increase in porosity and sorptivity and a slight reducing in the degree of hydration.

3. 28-day compressive strength, homogeneity and density of OPC concrete can be slightly degraded due to the adoption of UEO. However, the surface hardness of concrete has not adversely affected due to the use of UEO.

4. Impacts of UEO and air-entraining admixture on the various investigated characteristics of OPC concrete during its hardened seem to be more or less similar.

## ACKNOWLEGEMENT

## REFERENCES

1. Hamad, B. S., Rteil, , A. A. and El-Fadel, M. (2003), "Effect of used engine oil on the properties of fresh and hardened concrete", Construction and Building Materials, Vol. 17, pp. 311-318.
2. Samarin, A. (1999), " Wastes in concrete: converting liabilities into assets", Proceedings of the International Seminar on Exploring Wastes in Concrete, Edited by Dhir, R., and Jappy T., Scotland, pp. 1-21.

3.  Ibrahim, T. H. and Al-Zubaidy, A. H. (2007), "Assessment of using unleaded fuel in harsh environment of the United Arab Emirates", Journal of Environmental Management, Vol. 85, pp. 171-178.
4.  Hamad, B. S. and  Rteil, A. A. (2003), "Effect of used engine oil on structural behavior of reinforced elements", Construction and Building Materials, Vol. 17, pp. 203-211.
5.  Shafiq, N., Nuruddin, M.F. and Kamaruddin, I. (2006), "Effectiveness of used engine oil on improvement of properties of fresh and hardened concrete" Proceedings of the 6th Asia-Pacific Structural Engineering and Construction Conference (APSEC 2006), Kuala Lumpur, Malaysia, 5-6 Sept. 2006, pp. 159-166.
6.  McCarter, W. J., (1993), "Influence of Surface Finish on Sorptivity on Concrete", Journal of Materials in Civil Engineering, Vol. 5, No 1, pp. 130-136.
7.  Hall, C., (1989), "Water Sorptivity of Mortars and Concretes: A review", Magazine of Concrete research, Vol. 47, No. 147, pp. 51-61.
8.  Claisse, P. A., Elsayad, H. I. and Shabaan, I. G., (1997), "Absorption and Sorptivity of Cover Concrete", Journal of Materials in Civil Engineering, pp. 105-110.
9.  SERGI, G. (1986). "Corrosion of steel in concrete: Cement matrix variables", Ph.D. Thesis, Aston University, England, UK, 395 pp.
10. Parrott, L.J., (1992), "Variations of Water Absorption Rate and Porosity with Depth from an Exposed Concrete Surface: Effects of Exposure Conditions and Cement Type", Cement and Concrete Research, Vol. 22, pp. 1077-1088.
11. Rahman, A. A. and Glasser, F. P. (1989), "Comparative studies of the carbonation   of hydrated cements', Advances in Cement Research, Vol. 2, No. 6, pp. 49-54.
12. Ramachandran, A. I. (1969), "Application of different thermal analysis in cement chemistry", Pub. Chemical Publishing Company, London.
13. Du, L. and Folliard, K. J.(2005), "Mechanisms of air entrainment concrete", Cement and Concrete Research, Vol. 35, pp. 11463-1471.

# EXPERIMETAL AND NUMERICAL ANALYSIS OF STEEL SCAFFOLDINGS UNDER VERTICAL LOADS

*M. M. El-Sadaawy, M. T. Hanna*

*Structure & metallic construction institute*
*Housing and Building Research Center, Cairo, Egypt*
*m_massoud2002 @yahoo.com ; m_tawfick2003 @yahoo.com*

## ABSTRACT

Steel scaffoldings used in the shuttering of concrete works are temporary movable space steel structures which must have special treatment in analysis and in the calculation of the maximum working load. The types of scaffolding under study in this research are grouped into three groups with different spans and heights and constant width. The study has been divided into numerical and experimental investigations. The numerical analysis includes eigen value analysis to determine the elastic buckling loads, as well as nonlinear analysis to determine the ultimate loads. The experimental program includes testing for some cases with total height 4.0m.The numerical model was verified by comparing its results with the experimental one. The different buckling modes of failure have been plotted. In addition, the relation between the buckling length factor, K, and the total height of the scaffoldings has been determined. Moreover, tables and charts indicating the ultimate loads and the buckling factors are represented for the different types of scaffoldings.  Finally, the factor of safety for the frame work under analysis has been evaluated considering the allowable stress design method in the Egyptian code of practice. Results reflect that this factor of safety is less than that considered in Egyptian code of practice, especially in the elastic range.

## INTRODUCTION

The multi use of the scaffoldings in the shuttering of bridges and concrete buildings reflect a great importance in the design of these structural systems. The steel scaffoldings are usually space structures composed of slender elements and subjected to heavy loads due to the own weight of concrete. Moreover, their overall heights are relatively large compared with the cross section plan dimensions. Therefore, the determination of the ultimate capacity of these structures needs special analysis taking into consideration different modes of failure. The main two types of framework available in the Egyptian market are the cross bracing scaffolding and the truss spaced frame. The working capacity for the steel scaffoldings is typically determined through laboratory tests and the test setup is illustrated in some codes like the British standards (BS EN 12813:2004) for both the vertical and horizontal loads. A simple change in the system layout requires a new set of tests to evaluate the system and to determine its new capacity thus this research will focus primarily on regulating the design of the steel scaffoldings taking into account the effect of the space action on the different modes of failure that might occur under static loading.

The literature review done for this study focused on the stability of multistory frames. Chen and others (1995) detailed the method specially designed for elastic buckling analysis of cross bracing scaffolding systems where failure is controlled by instability. The influence of the connection stiffness is included in the analysis by the concept of effective length. It was found that the buckling capacity of the frame is very much dependent on the joint stiffness and the

---

degree of dependence increases with the unit height. Salem and others (2004) studied  the effect of unsymmetrical loads acted on braced and unbraced multistory frames. They showed that the presence of unequal axial forces in columns together with primary bending moments have a considerable effect on the elastic buckling loads of the braced planar frames. Chung (2004) presented a systematic study on the structural behaviour of multi-storey door-type modular steel scaffolds through both experimental and numerical investigations, he proved that it is unconservative to take the load carrying capacities of two storey and three storey modular steel scaffolds to be the same as those of one storey scaffolds due to significant difference in their buckling behaviour. Chan and Zhou (2000) produced a practical integrated nonlinear analysis and design  for a simple column in two dimensional truss and three dimensional space frame, the method produces a consistent result as the design codes in the generation of the column buckling curves.

**Cases under study**
The frame works considered in this research are the trussed space frame which consists of several rounded pipe sets connected with each other and every set was 2.0m high and consists of circular pipe columns and horizontal truss. The truss has a height of 0.5m and consists of welded round pipes. These sets are connected to each other by circular pipe with benz. The columns are supported by jacks at the ground to adjust the total height. The frame works under study have three different spans (1.2, 1.8, and 2.7 m) while the spacing is constant and equal to 1.2m as shown in Fig.(1), thus we have three groups with different heights ranging from 4.0m to 20.0m. The buckling modes for plane structures have been studied in a lot of researches showing the governing failure mode.

## ANALYSIS

**Experimental analysis**
The three groups of scaffolding shown in Table (1) were erected in the lab at the Housing and Building Research Center with a total height 4.0m. The geometric imperfections of the columns were measured using a total station.The deviation in X and Y directions were recorded for the four columns of the three groups at the mid height of the columns. The maximum deviation either in X direction or Y direction didn't exceed ± H/200.  The four columns of the frame work were loaded gradually up to 30 ton (working load). The strains and displacements in columns were recorded using strain gauges and LVDT"s. The strain gauges have been located on the columns at every level at perpendicular points to indicate the normal strains which are accompanied by bending strains due to the imperfections and buckling. The displacements have been measured at the middle height of the columns in the two horizontal directions. Figure (2) shows the locations of the strain gauges and the LVDT"s., while Fig. (3) shows the experimental setup.The relation between the applied load and the strains for the three groups were plotted in Fig. (4), while the relation between the applied load and the displacements were plotted in Fig.(5).

**Table 1: Dimensions of the scafolding experimental studied cases**

| Group No. | Plan dimensions | | Truss-spacing in elevation s (mm) | Height h(mm) |
|---|---|---|---|---|
| | b(mm) Width | a(mm) Length | | |
| A | 1200 | 1200 | 500 | 4000 |
| B | 1200 | 1800 | 500 | 4000 |
| C | 1200 | 2700 | 500 | 4000 |

**Non linear analysis**
A non-linear finite element model is made using "COSMOS/M" finite element package (Ref 7). Both geometric and material non-linearties were accounted for the model. The geometric imperfections have been included in the analyses by modeling the columns. The stress-strain

curve of the material is assumed to be elastic-perfectly plastic obeying VON- MISSES yield criterion and it is assumed that the material of the cross sections is steel 37 with yield strength 2400 Kgm/cm2. The boundary conditions for columns satisfy the hinge support conditions. Ultimate nonlinear analysis has been carried out for the three groups (A,B,C) considering truss vertical spacing 0.5m with total height 4m and 16m and also for spacing 1.5m with total height 5m and 15m.   For groups (A) and (B) the modes of failure were torsion and overall buckling, while for group (C) the mode of failure is overall buckling for different heights which are presented in Fig.(6). The load displacement relation obtained by finite element analysis are represented in Fig.(5). Compression between non-linear analysis and experimental load-deflection curves reflects that the non-linear finite element model give the same response as experimental one. This is clearly shown in Fig.(5b) in which the LVDT(2) reading correlate the F.E.M. results.

### Elastic analysis

In the analysis, a three dimensional model (COSMOS/M) was conducted to deduce the elastic buckling loads. The connections between the members of the trusses with the columns are considered as flexible joints, while the other connections are considered as rigid connections. The supports are considered as hinges. Three groups, "A": 1.2x1.2m, group "B" : 1.2x1.8m, and group "C" :1.2x2.7m, are considered as indicated in Fig.1. The column cross section was selected as a pipe with diameter 61mm and thickness 2.0mm, while the truss sections were pipes with diameter 34mm and thickness 1.5mm. The parameters considered in the analysis were the span of the scaffolding, a, the spacing between trusses, S, and the total height of the scaffolding, H. Two values for the spacing (S) were investigated;0.5m and 1.5m. The total height H has values of 4m, 8m, 12m, 16m, 20m, for spacing S= 0.5m, while for spacing S= 1.5m , the height H has values of 5m, 9m, 13m, 15m and 21m. Elastic analysis was performed to indicate the elastic buckling load for all the groups, thus the factor of buckling length related to spacing, S, has been deduced as shown in Fig.(7) for spacing S =0.5m and in Fig.(8) for spacing S=1.5m using the elastic Euler equation  $(P_e = \prod^2 EI/L^2)$.

## RESULTS AND DISCUSSIONS

In order to check the experimental work with the analytical work , the load displacement curve for the three experimental cases up to 30 ton loading was compared with that of the numerical analysis up to failure in Fig.(5). Figure (7) and (8) represent the relation between the buckling length factor (K) and the total height of the scaffolding. It is clearly shown that the buckling factor (K) increases by increasing the total height (H), especially for spacing S=0.5 m. For S=1.5m,the increase in (K) is slightly less. For the three groups, the increase in width (a) of the scaffoldings caused a decrease in the buckling factor (K). From elastic analysis and the values of (K), we estimated the working load per column on the scaffolding using the Egyptian code of practice (ASD-2001) and calculated the factor of safety by dividing the ultimate load detected from the nonlinear ultimate analysis with the working load deduced by the Egyptian code of practice as shown in Tables (2) and (3). In most cases it is obvious that the factor of safety is less than that considered in ECP, especially in the elastic range.

**Table 2: Spacing S=0.5m**

| GROUPS | GROUP(A) | | | | GROUP(B) | | | | GROUP(C) | | | |
|---|---|---|---|---|---|---|---|---|---|---|---|---|
| H (m) | l/i | PULT (F.E.) (ton) | Pworking (ECP) (ton) | F.S. | l/i | PULT (F.E.) (ton) | Pworking (ECP) (ton) | F.S. | l/i | PULT (F.E.) (ton) | Pworking (ECP) (ton) | F.S. |
| 5 | 104 | 8.5 | 4.97 | 1.71 | 112.9 | 8.022 | 4.213 | 1.904 | 111.4 | 8.1875 | 4.33 | 1.89 |
| 15 | 118.81 | 7.303 | 3.8 | 1.92 | 128.5 | 7.173 | 3.252 | 2.2 | 118.8 | 7.533 | 3.805 | 1.98 |

**Table 3: Spacing S=1.5m**

| GROUPS | GROUP(A) | | | | GROUP(B) | | | | GROUP(C) | | | |
|---|---|---|---|---|---|---|---|---|---|---|---|---|
| H (m) | l/i | PULT (F.E.) (ton) | Pworking (ECP) (ton) | F.S. | l/i | PULT (F.E.) (ton) | Pworking (ECP) (ton) | F.S. | l/i | PULT (F.E.) (ton) | Pworking (ECP) (ton) | F.S. |
| 4 | 64.36 | 14.337 | 8.1 | 1.77 | 76.73 | 14.03 | 7.284 | 1.926 | 71.8 | 14.266 | 7.625 | 1.87 |
| 16 | 80.45 | 10.3 | 7.012 | 1.46 | 92.1 | 10.78 | 6.076 | 1.77 | 76.73 | 11.343 | 7.284 | 1.56 |
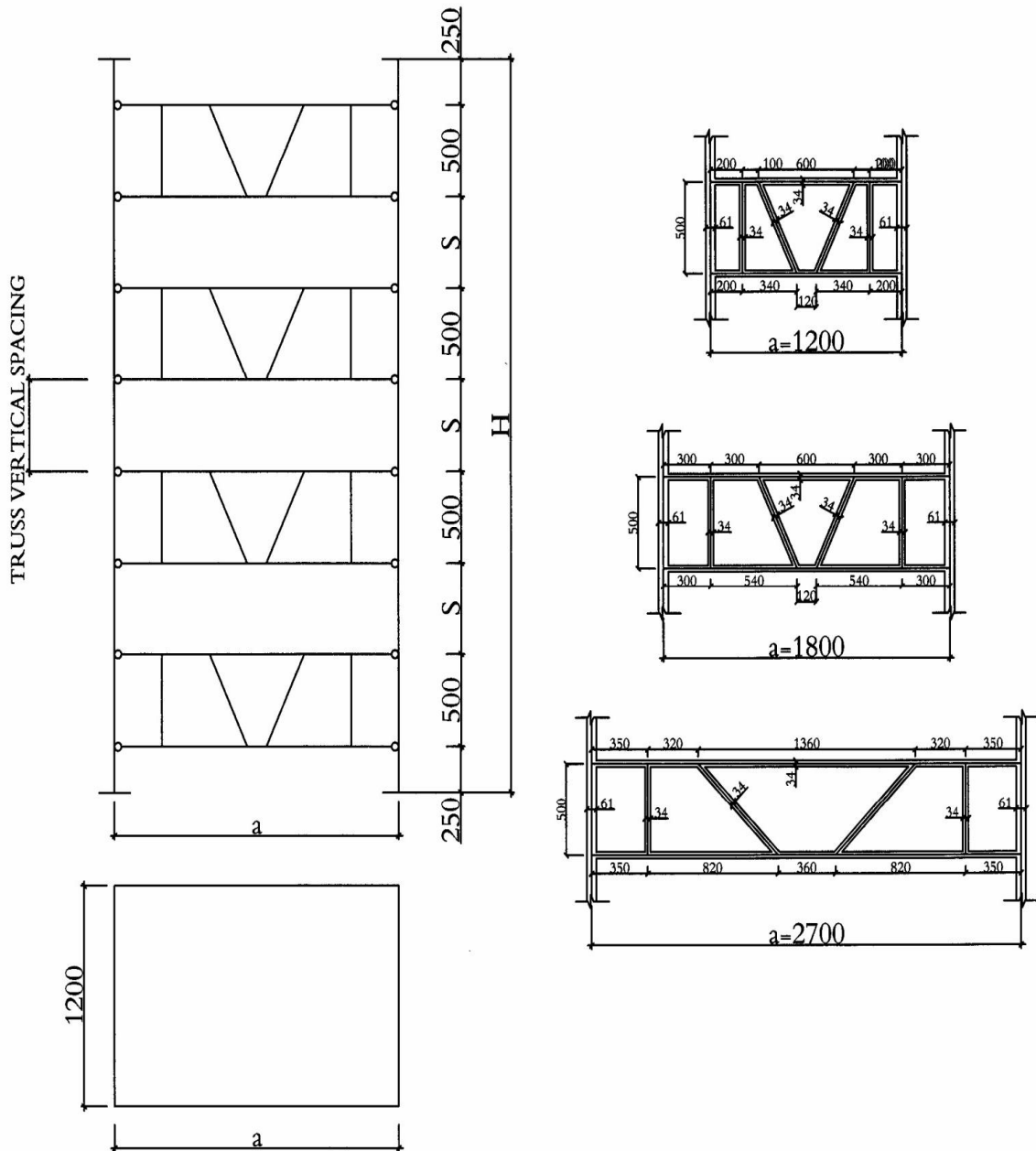


**Fig. 1: The theoretical cases**
**Typical dimensions and configurations for steel scaffoldings**
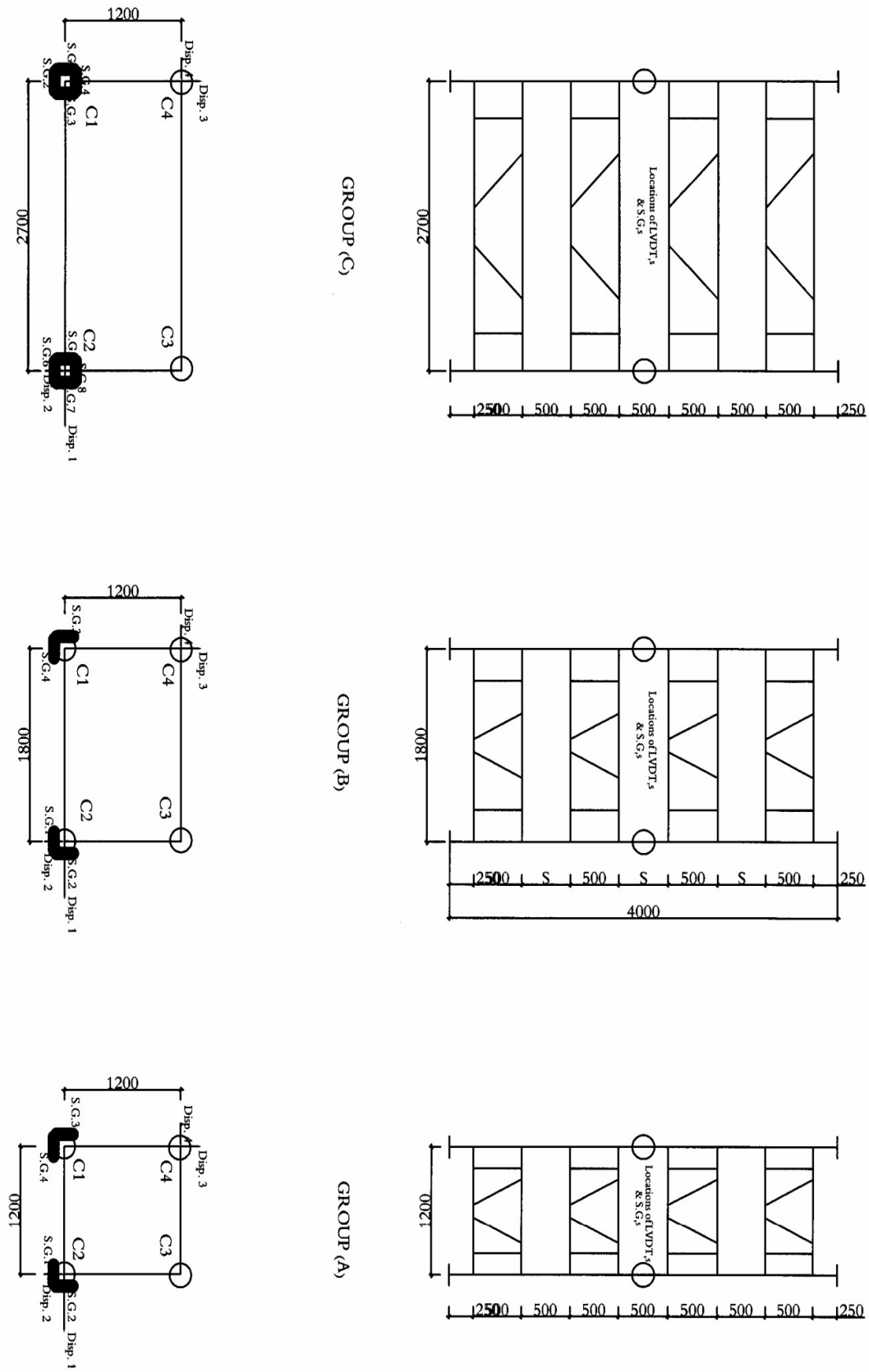
**Fig. 2: The experimental cases**
**Geometric dimension of the three tests specimens**
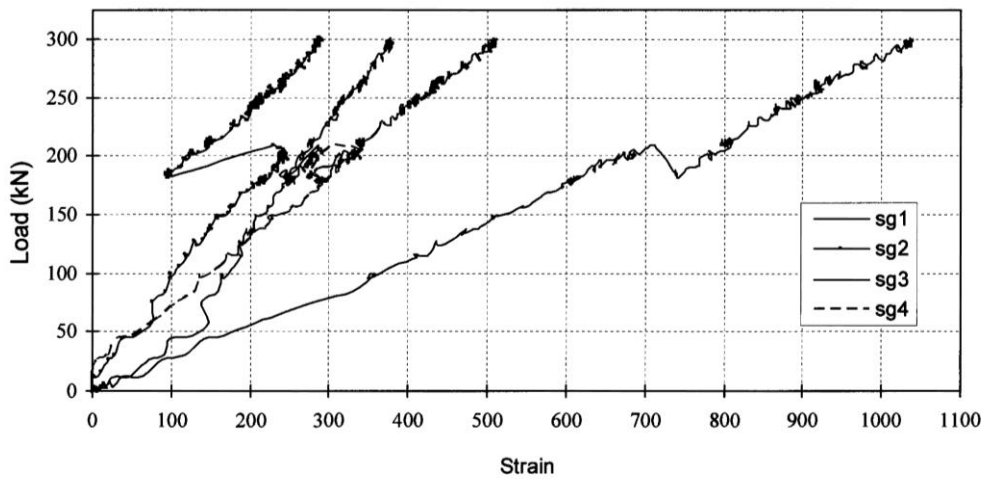
**Fig. 3: Experimental setup**



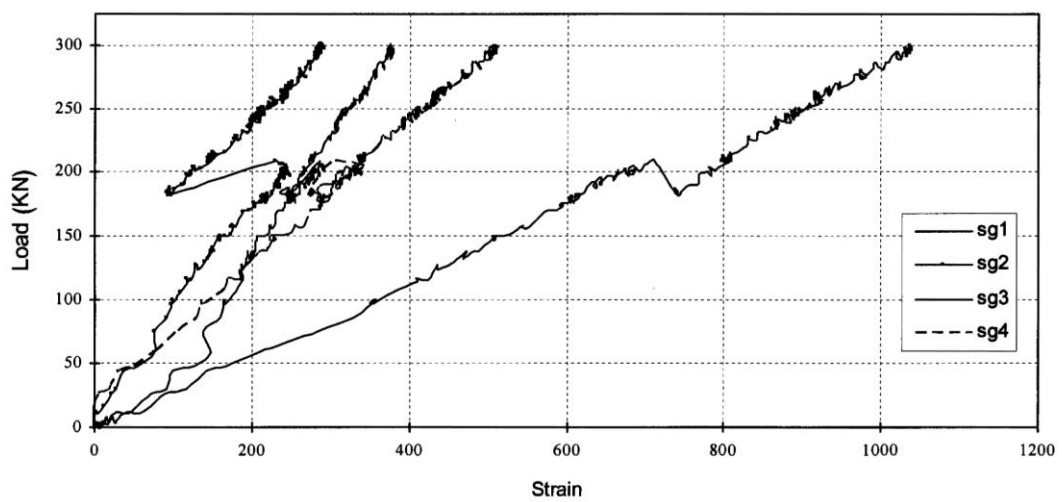**Fig. 4: (a) Relation between load & strain for group ( A)**



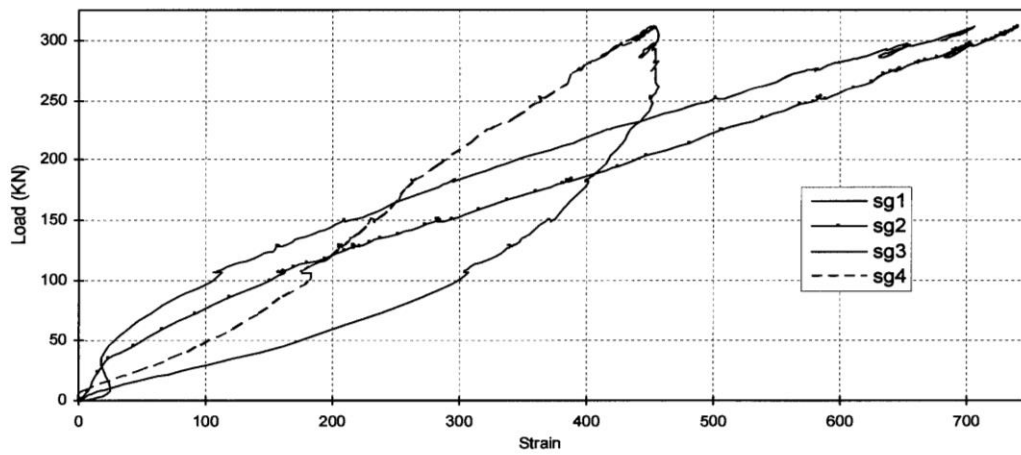**Fig. 4: (b) Relation between load & strain for group ( B)**

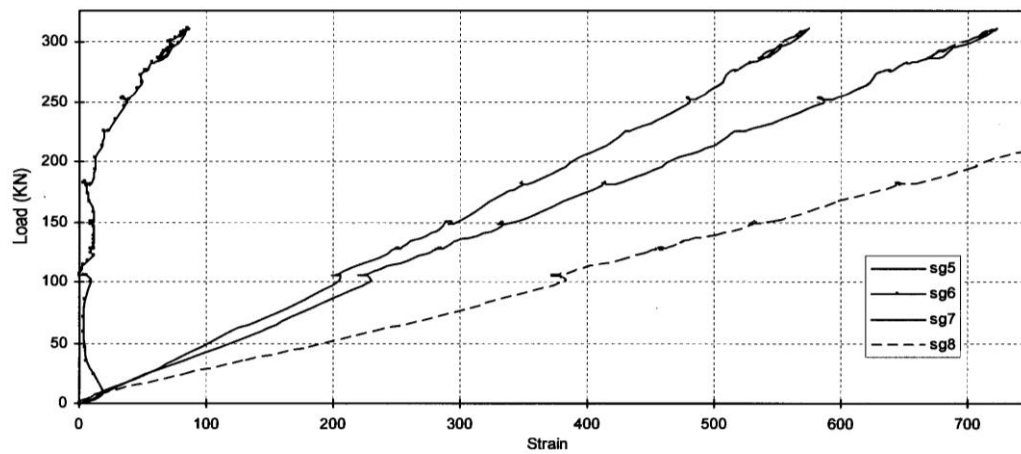**Fig .4: (c) Relation between load & strain for C1 group (C)**

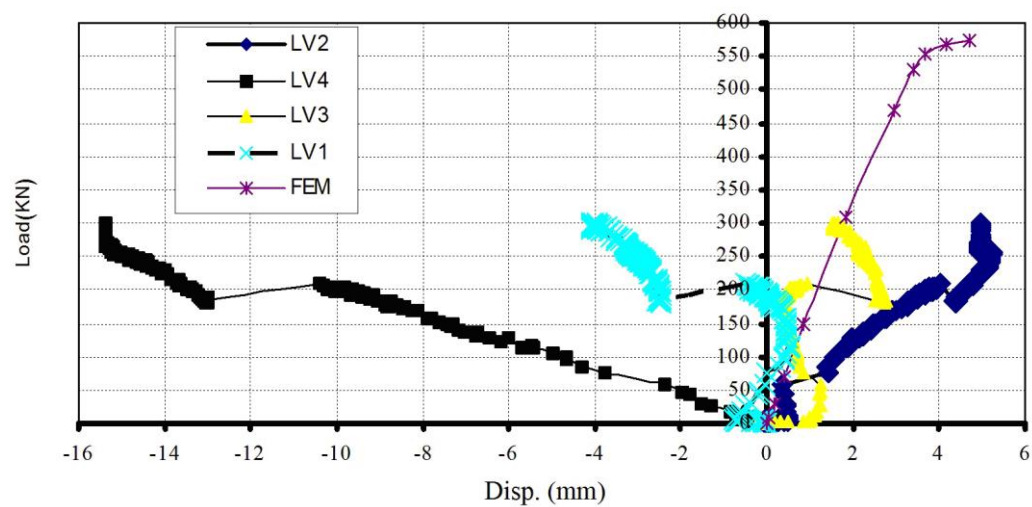**Fig. 4: (d) Relation between load & strain for C2 group (C)**
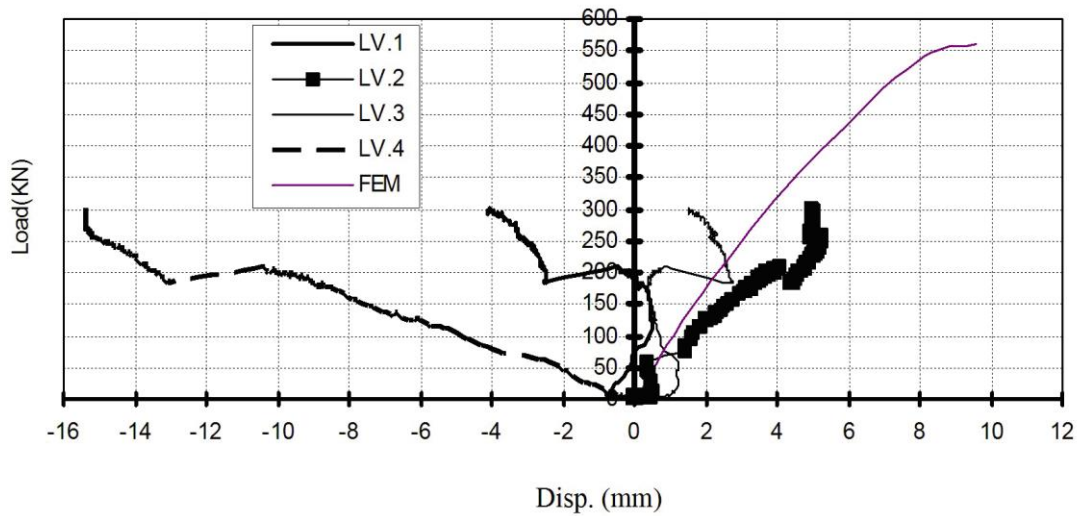
**Fig. 5:(a) Relation between load & displacement for group (A)**

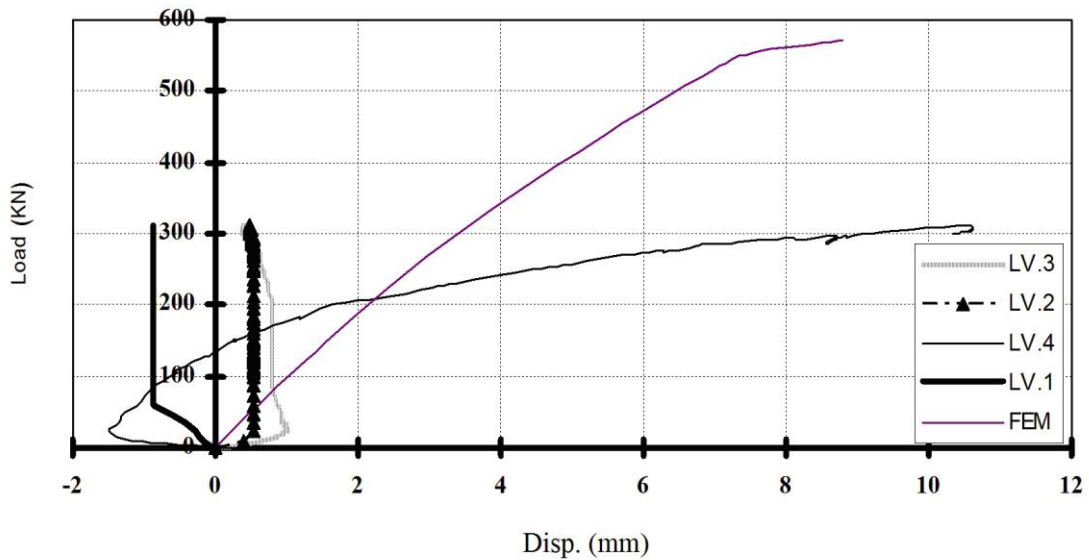**Fig. 5:(b) Relation between load & displacement for group (B)**



**Fig. 5:(c) Relation between load & displacement for group (C)**

## CONCLUSIONS

From previous analysis we can conclude the following:
1. The total height of the scaffolding has a very significant effect on the elastic buckling load and also on the ultimate load due to the significant difference in buckling behaviour for different scaffoldings with different heights.
2. The cross section dimensions have no significant effect on the ultimate capacity of this type of scaffoldings.
3. The use of the Egyptian code equations in calculating the working stress is not applicable for such types of structures. Thus the code must consider a factor of safety for temporary structures different than that for permanent ones taking into consideration the shape, the modeling of connections and the height of the scaffoldings and the imperfections during fabrications and erections.
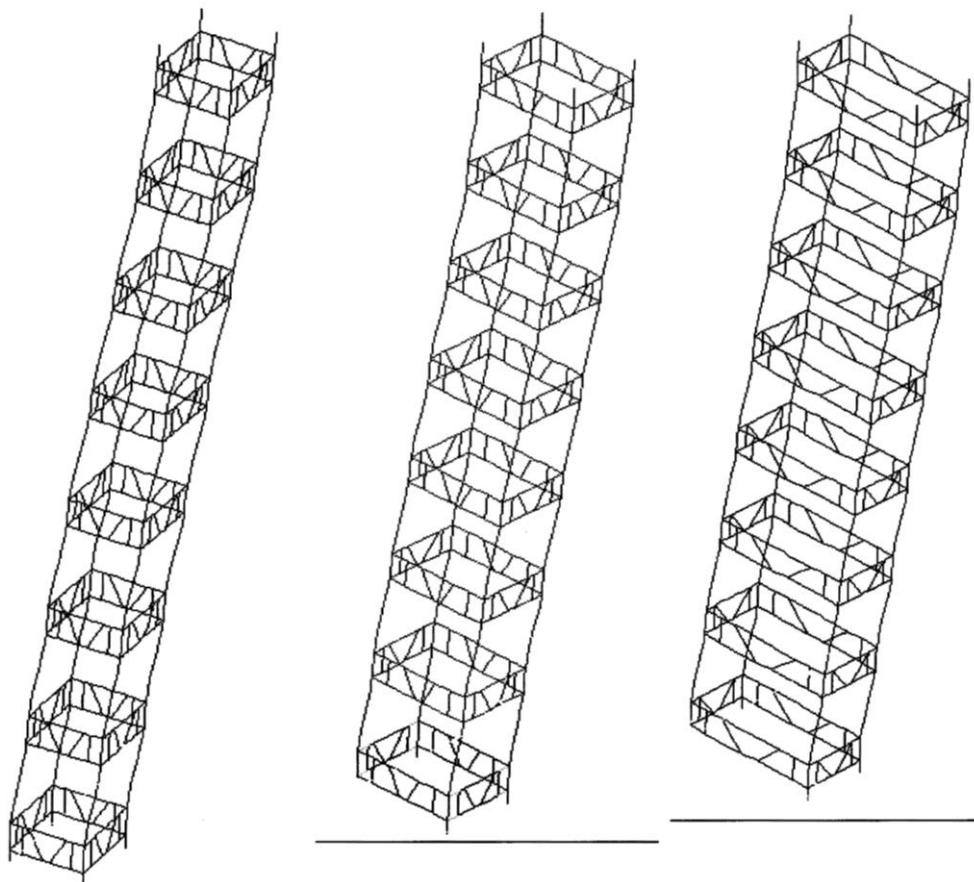
Group "A" 1.2mX1.2m          Group "B" 1.2mX1.8m          Group "C" 1.2mX2.7m

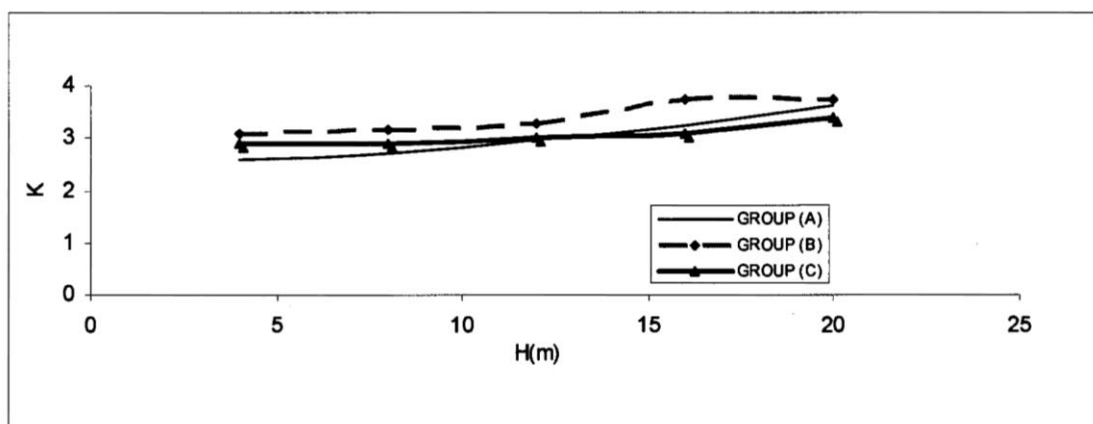**Fig.6: Buckling mode shapes, S = 1.5m**



**Fig. 7: Relation between total height (H) & buckling factor (k) for spacing 0.5 m**
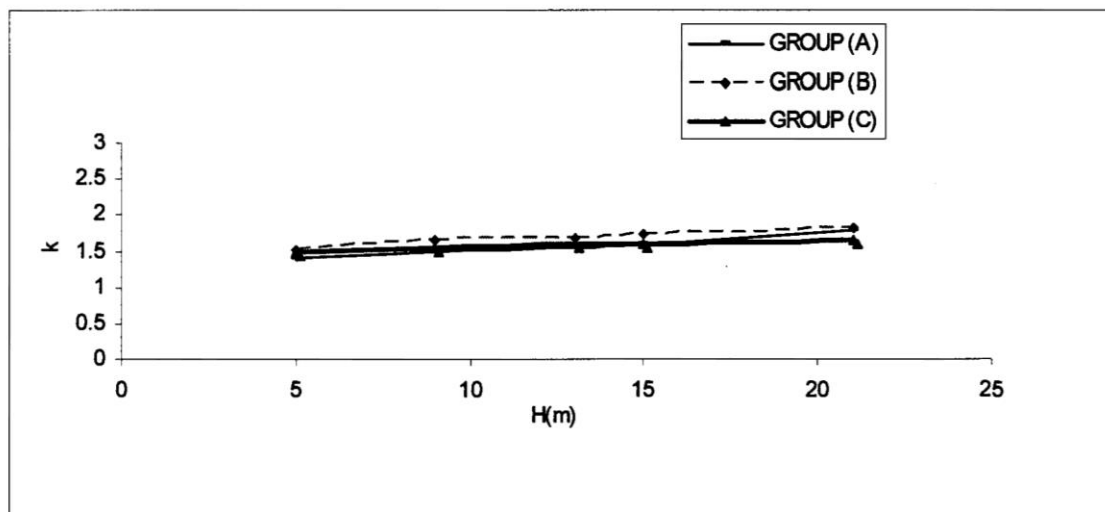
**Fig. 8: Relation between total height (H) & buckling factor (k) for spacing (1.5 m)**

## REFERENCES

1. Chan, Zhou and others, (1995), "Stability analysis of semirigid steel scaffolding,"J. Engineering Structures .vol.17, No. 8, pp.568-574.
2. Chan, (2001), "Non-linear behavior and design of steel structures," J. of Constructional Steel Research, vol.57, pp. 1217 - 1231.
3. Chan and Zhou (2000), "Non-linear integrated design and analysis of skeletal structures by 1 element per element." J. Engineering Structures. Vol. 22, pp. 246-257.
4. Chung (2004), "Structural instability of multi-storey door-type modular steel scaffolds." J. Engineering Structures. Vol. 26, pp. 867-881.
5. Salem A.H., M. El Aghoury, F.F. El Dib, and M.T.Hanna (2004),"Elastic stability of planar steel frames with unsymmetrical beam loading", J.Structural Engineering, Nov, pp. 1852 - 1859.
6. British Standard BS EN (2004) -12813, "Temporary works equipment".
7. COSMOS/2.6 Preprocessing, Analysis and Postprocessing Interface – Structural Research and Analysis Corporation – Santa Monica, California 90405.
8. Egyptian code of practice for steel construction and bridges (Allowable stress design ASD) code No. ECP 205-2001.

# POTENTIAL HAZARDS OF NONSTRUCTURAL SYSTEMS DAMAGE IN HOSPITALS UNDER EARTHQUAKES IN EGYPT

## * Dr. Mohamed Ihab Sherif Elmasry

*Associate Professor, Construction and Building Engineering Dept.*
*Arab Academy for Science and Technology and Maritime Transport (AASTMT)*
*P.O. Box 1029, Abu-Qir, Alexandria, Egypt, Email: elmasryi@yahoo.com*

## ABSTRACT

Buildings in the contemporary world have a lot of nonstructural components within their interior details. Such components include plumbing pipes, air conditioning ducts, fire fighting systems, *etc.* Because earthquakes happen, the reliability of such nonstructural details inside seismically excited structures should be a matter of concern. However, it has always been difficult to develop a single set of seismic design guidelines for all the nonstructural components due to the diversity of types and configurations. This is the fact despite that damages to nonstructural components during earthquakes represents a significant portion of the resulting imposed damage in structures. Moreover, though design codes may allow for some nonstructural damage under moderate earthquakes yet some buildings such as hospitals cannot tolerate such damage in order to remain functional. This is the case as hospitals need to be continuously functional especially when catastrophic events as earthquakes take place. An analysis that shows one of the forms of the nonstructural damage in hospitals under seismic loading is studied. A main fire fighting piping system fixed to the ceilings of a hospital building is the case study. The study focuses on the dynamic response of the fixation system of the fire fighting piping network during earthquakes. Results obtained from the numerical example indicate the necessity to include the dynamic structural parameters of the buildings in defining the equivalent lateral seismic forces on nonstructural components fixations.

**Keywords:** Nonstructural Details, Damage, Hospitals, Earthquakes, Seismic Excitation.

## INTRODUCTION

Nonstructural details or secondary systems in structures are those systems and elements housed or attached to floors, roof, and walls of a building or an industrial facility that are not part of the main or intended load bearing structural system of the building or the industrial facility [21]. Generally, nonstructural components may be classified into three broad categories: *(1)* Architectural components; *(2)* Mechanical and electrical equipments; and *(3)* Building contents. Examples of architectural nonstructural components are: nonbearing walls and partitions, cladding, *etc.* Examples of the mechanical and electrical components are: piping, air conditioning systems, *etc.* Furniture is a good example of the third category. Such nonstructural details, however, may be subjected to relatively large seismic forces and must depend on their own structural characteristics to resist these forces.

In addition, the evolution of model building codes around the globe had been a process that fundamentally focused on the primary structural systems of buildings. This consequently resulted in the fact that the secondary systems and nonstructural components were given much less attention than that given to the primary structural systems [9,11,21]. In spite of their name, secondary systems are far from being secondary in importance. It is now widely recognized that the survival of secondary systems and nonstructural building components is essential to provide emergency and recovery services in the aftermath of an earthquake [8]. In addition, the safety concerns as well as the possibility of severe economic losses demand a better performance

from these components during an earthquake event, and call for better design requirements and preventive measures [16]. The case is even more reflected in case of the Egyptian codes for assembling nonstructural details where until recently, only the Egyptian Code of Practice of Air Conditioning and Cooling (ECP-ACC)[17] included two appendices (C and D) explaining the seismic lateral forces design for the anchorage of some mechanical and electrical details. In spite of that, the latest Egyptian code of Practice for Loads and Forces Calculation in Structural Works (ECP-ELF)[18], which was firstly issued in 2003, includes in section 8-7-5 further details for evaluating equivalent seismic forces on nonstructural components in buildings. However, the 2003 version of ECP-ELF [18] was restored several times for corrections and revisions by the publishing authority and using older codes was the case until the ECP-ELF [18] was finally issued in September 2008.

Nonetheless, nonstructural components have recently been given a renewed interest from code writing authorities [5] and have been strongly influenced in the USA for example by the National Earthquake Hazards Reduction Program (NEHRP) [6,7]. This can even be observed from the major changes in the requirements for nonstructural components that were adopted when going from the 1994 Uniform Building Code (UBC) [19] to the 1997 UBC [20] and then to the new International Building Code (IBC) [10]. Villaverde (1997) [21] provides an excellent review of some of the recent activities in USA and Japan in that field. However, changes in the seismic design provisions for nonstructural components in many codes [10,17,19,20] have focused primarily on the magnitude of applied forces and have not explicitly considered the dynamic behavior of the nonstructural components or their attachments [11]. Accordingly, a difficult question that earthquake investigations about buildings reliability attempt to answer would be "are our latest codes and standards doing an adequate job, or do they require revision?"

Moreover, the reliability of nonstructural components in healthcare facilities as hospitals is even of greater interest and should be studied carefully for many reasons. A fundamental reason would be the fact that nonstructural components in hospitals are essential and their failure may lead to the closure of facilities that are structurally undamaged.  Another reason would be the fact that if hospitals become not serviceable during major events such as earthquakes then the number of human losses would exponentially increases. This should consequently require for studying the reliability of the hospitals structural systems and their nonstructural components under earthquakes or similar destructive events.

This paper studies the damage hazards that can be undergone by the fixation systems of some of the nonstructural components in existing hospitals, built before the year 2008, under seismic loading. A 6-story multi span hospital building with a main fire fighting piping system hung to the ceilings is the case study. The study focuses on the dynamic response of the fixation system of the fire fighting piping network during earthquakes. The observations introduced herein show how neglecting important design parameters such as dynamic response amplification in the design of anchorages of nonstructural components inside important structures, *e.g.* hospitals, can lead to damage of such anchorages and destruction of the attached nonstructural components. Results obtained from the numerical example indicate the necessity to consider the dynamic structural parameters of the buildings main structural systems on designing a nonstructural component fixation.

## HISTORICAL REVIEW OF NONSTRUCTURAL DAMAGE IN BUILDINGS

Many lessons can be learnt from the investigated damages to nonstructural components in buildings during previous earthquakes. Such lessons can be a good guide for learning how to protect essential facilities such as hospitals from earthquake disruption in Egypt. As found in many prior earthquakes *e.g.* Northridge earthquake in California, USA, the performance of engineered or code conforming component anchorage was significantly superior to that of components installed without the benefit of earthquake engineering [6]. For example, damage to low-rise storefront windows was more prominent than damage to high-rise curtain wall systems and glazing for which design methods based on drift have been in wide use over the past two decades. As another example, suspended ceilings installed in the 1980s or 1990s in USA benefited from the seismic provisions of the Uniform Building Code (UBC) [19,20], which required diagonal tension wires and vertical compression struts. The newer ceilings had less damage than older ones, though in many cases the new installations did not meet the full intent of the UBC provisions [9].

Moreover, as in prior earthquakes, damage to mechanical equipments during Northridge earthquake was widespread [9]. However, mechanical and electrical details designed using prescriptive building code requirements for seismic forces appeared to have performed better. This is the fact knowing that the amplification of the seismic forces at the upper stories or at the roof of multi-story buildings may have exceeded the capacity of the mounting hardware at several installations. In other instances, the design may have been adequate; however, the installation was not complete. For example, bolts that were too short were ripped from mounting plates because of insufficient engagement.

**Healthcare Facilities**

A large amount of information has been collected on hospitals damage during the Northridge earthquake, 1994 [9]. In addition to the efforts of Earthquake Engineering Research Institute (EERI) reconnaissance team members, the state's Office of Statewide Health Planning and Development (OSHPD) collected and analyzed information. In addition to the reports by OSHPD [13], other reports were used to compile the information about damages to the medical facilities during the Northridge earthquake [4,12,14,15].

The draft report prepared by OSHPD to the state's building safety board [13] states that hospital buildings constructed under the requirements of the seismic safety act performed well with respect to the primary structural systems except for Holy Cross hospital that suffered severe structural damage. However, the performance of nonstructural details of the buildings performed poorly. This consequently resulted in extensive damage to the building interiors including flooding, which resulted in a temporary shut down of several hospital buildings. A similar conclusion was reached in the seismic safety commission background report [4]. Murray (1994) [12] states that broken domestic water piping was found in 20 facilities, and broken fire sprinkler piping in 29 facilities. Emergency power systems failed to operate at six facilities, not including temporary outages. The overall restoration of utility electrical service was rapid: about 93% had their power back within 24 hours. However, the hospitals in the vicinity of Northridge, where the shaking and damage were worst, often faced longer outages, extending to about a week [14].

In addition, Patrucco and McGavin (1994) [14] stated that as a result of the shaking due to Northridge earthquake, ten hospitals partially or completely evacuated patients. The fact that two of the largest and newest healthcare facilities by that time in the San Fernando Valley, Olive View and Holy Cross, were effectively shut down for the week of the earthquake by nonstructural damage is troubling and raises issues about whether the seismic safety act's aim to provide functional hospitals is being met. At Olive View hospital, the primary or most disabling nonstructural damage was water leakage from the fire sprinkler and chilled-water piping systems, which led to the decision of evacuation [9]. On the roof, four-inch chilled-water lines broke at cast iron valves and the flowing water penetrated to the top floor. At numerous locations, unbraced small-diameter copper piping broke at their connections to anchored equipment. Recommendations have been made for more thorough approaches to pipe bracing, as well as for more thorough contingency planning, and emergency response training [3,9,13]. Figures 1 to 3 show some of the piping damage encountered in some hospitals after the Northridge earthquake in 1994 [9].

## PROBLEM DEFINITION

During earthquakes, the structural systems of hospitals in seismically active zones might be well shaken and excited. However, since hospitals buildings include many nonstructural details, then the credibility of a hospital to remain in function, after an earthquake erupts, requires that most of the attached nonstructural details are capable of withstanding the shaking as well as the structural system. In Egypt however, apart from the ECP-ELF, 2003[18] and two appendices (C and D) in the Egyptian Code of Practice of Air Conditioning and Cooling (ECP-ACC 2004 [17]) explaining the seismic lateral forces design of the anchorage of some mechanical and electrical details, one would not find a clearly enforced guidelines for the fixation of nonstructural details under seismic excitations. This is the case despite that earthquake damage to nonstructural components represents a significant portion of the earthquake damage in hospitals [6,11]. Accordingly, many hospitals in Egypt, which were built before applying the recent ECP-ELF code [18] (finally issued for practice in September 2008), have nonstructural components anchorages that are not well designed to resist an expected earthquake loading. Therefore,

such hospitals are subjected to unfavorable damage hazards. Having damaged hospitals and with such large number of injuries expected after earthquakes, the victims may face a great risk of not finding a suitable place for treatment.



**Fig. 1: A sprinkler pipe break at Olive View Hospital [9]**



**Fig. 2: Four-inch chilled-water lines broke at cast iron valves – Olive View hospital [9]**



**Fig. 3: Extensive flow of water from broken sprinkler pipe at the Sepulveda Veterans Administration medical center, building 3 on the 5th floor [9]**

Moreover, hospitals after earthquakes even act like a shelter and therefore are immediately occupied by people escaping the aftermath of earthquakes. Thus, the design of piping fixation systems for example in hospitals should be up to such an immediate occupancy performance level expected after earthquakes. Accordingly, the piping fixation systems design for example should consider not only that the pipes do not fall when they are suspended, but also that the

pipes should not leak due to earthquake displacements or shaking [11]. Bearing that in mind, it may not be sufficient to seismically design such systems for simply a lateral equivalent static force, but rather it is recommended to study the dynamic response aspects as well.

One of the dynamic response aspects that are undermined in the ECP-ACC [17] is the dynamic amplification of the response of nonstructural fixation systems under seismic loading. This dynamic behavior when exists is a result from the close proximity of the natural periods of the input dynamic excitation and the natural periods of the excited system. Amazingly, the amplification factor used in the evaluation of the equivalent static lateral design force for the suspended piping or electrical systems is assumed to be equivalent to 1.0 in ECP-ACC [17]. This is the case despite that the design seismic lateral forces for nonstructural details should not be independent of the dynamic characteristics (*e.g.* natural frequencies) of the building to which the nonstructural component is fixed [16]. In summary, to reduce damage hazards in hospitals, it is mandatory to make sure that the fixation systems of nonstructural components are capable of withstanding the acting loads during earthquakes. Finally, changes should be considered for the seismic design of nonstructural components in the ECP-ACC [17].

## CASE STUDY

An estimated well-equipped existing hospital building with all expected nonstructural details included above the false ceiling is the case study in the paper. The hospital is assumed lying in the north-west seismic zone of Egypt, for example in Alexandria. The secondary systems are assumed rigidly connected to the building. One of the damage hazards that thus may take place is the failure of fixations of heavy nonstructural details above the false ceiling such as heavy main fire fighting pipes. This consequently would lead to unexpected leakage of water or toxic liquids due to pipes breakage, or in worst case, heavy pipes dropping on the false ceiling and eventually to the ground. Figure 4 shows a typical suspended fixation system for pipes hung above the false ceilings.
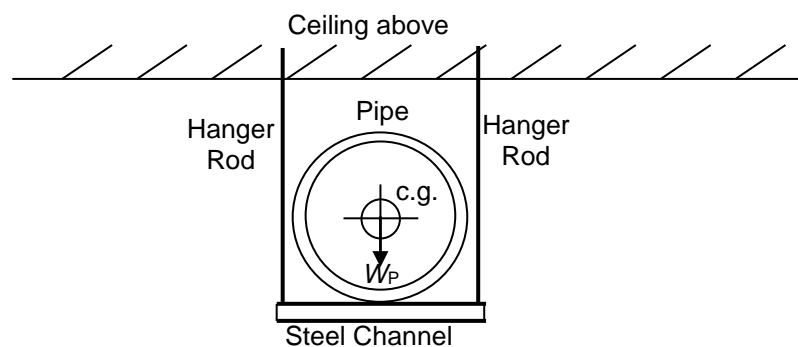


**Fig. 4: Hanging Frame (Supports and Bracing) for suspended Equipments**

**Numerical Example**

The numerical example in this paper considers the anchorage of a heavy fire fighting piping system hung to the ceiling. The piping system includes main pipes with diameters of 8 inches filled with water and fixed above corridors and hallways. The system is carried by a frame hanging system that is composed of two steel hangers that are rigidly connected to the ceilings (rods with 12 *mm* diameter) and a horizontal steel channel, as shown in Fig. 4. The vertical height of the hanging frame varies but in the study herein, the height is assumed equivalent to 500 *mm* from the ceiling.

For water systems as fire fighting systems, the piping material most widely used is steel. Thus, it is assumed that the pipes used in the studied fire fighting piping system are made of galvanized steel that follows schedule-40 pipe dimensions and properties. Schedule 40 is the standard used for pipes of water systems with diameter up to 10 inches (250 *mm*) as per the American National Standards Institute-ANSI B36.10 [1]. Thus, the weight of the pipe with water is assumed 75 *kg/m* (ANSI B36.10) [1]. Moreover, based on ASHRAE (American Society of Heating, Refrigeration, and Air Conditioning Engineers) [2] standards requirements, the pipes are assumed anchored by the hanging frames to the ceiling every 19 *ft* (nearly 6 *m*) along the route of the pipes.

In addition, it is assumed in the numerical example herein that the piping system is rigidly attached to the structure through the hanging frame. Conveniently, the studied piping system is considered fixed to the ceilings of each floor of a 6-story hospital building. The structural system of the hospital is assumed as a reinforced concrete moment resisting frame with rectangular cross sections, as shown in Fig. 5.
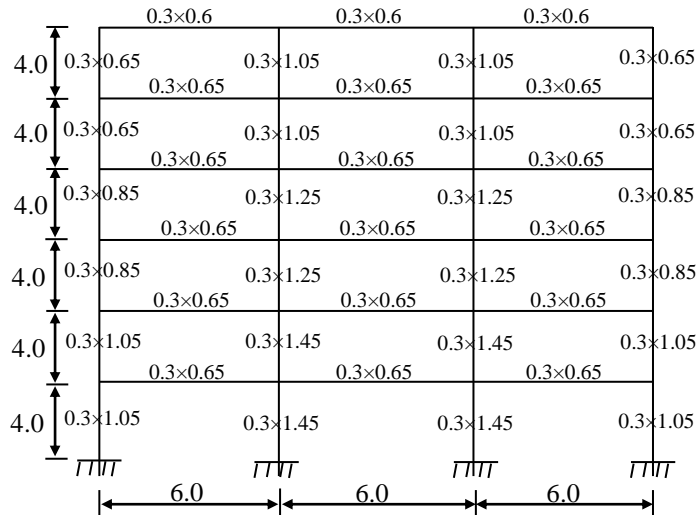


**Fig. 5: Moment resisting frame-structural system of the studied hospital**

The assumed hospital building structural system is designed to resist gravity and seismic loads [18]. The frame has three 6-meters spans and a floor height of 4-meters to give space for mechanical and electrical equipments above the false ceilings. The spacing between the moment resisting frames is taken as 5-meters. The total load of each floor on each moment resisting frame is taken as 90.56 *tons* per floor except for the roof that is taken as 64.66 *tons*.

## METHOD STATEMENT

In order to study the dynamic response of the building – pipes anchorage system, a convenient model should be chosen. The system model herein assumes that the moment resisting frame of the hospital building will behave as a shear-building model under seismic loading. In addition, the stiffness factors of the different floors of the building are calculated based on the lateral stiffness factors of the frame columns only. Thus, the lateral stiffness factors of the frame are 928138 *kN/m* for the first and second stories, 505427 *kN/m* for the third and fourth stories, and 281974 *kN/m* for the fifth and sixth stories. The damping ratio, $\zeta$, is assumed as 5% for the moment resisting frame structure whereas damping is neglected for the piping fixation frame. The Caughey damping procedure [5] is used to evaluate the classical damping matrix of the moment resisting frame structure. In addition, each hanging frame (pipes anchorage system) is assumed to behave as a single degree of freedom (SDOF) oscillator system that is mounted on each floor of the hospital structure, as shown in Fig. 6.
Moreover, since the safety of hospitals in Egypt is the main concern of this paper, then it is appropriate to use the time histories of earthquakes that occurred in Egypt in the seismic excitation testing of the building – pipes anchorage system. However, the time histories of most previous earthquakes in Egypt are not available. Thus, only the time history of the Nuwaibaa earthquake, 1995, is used to excite the building – pipes anchorage system. This should be acceptable since this paper is only studying the nonstructural damage potential in hospitals and if it exists in an earthquake then it may exist in any other earthquake. However, the available recorded earthquake ground acceleration time histories of Nuwaibaa earthquake are normalized to a maximum peak ground acceleration of 0.08*g*. This is reasonable, since the measurements of the earthquake ground accelerations are sometimes distant from the epicenter of the earthquake and the chosen peak ground acceleration is close to what is expected to occur in the north-west seismic zone of Egypt (*e.g.* Alexandria). Figure 7 shows the normalized ground

acceleration time histories of the Nuwaibaa earthquake in both the east-west and north-south directions. Moreover, Figure 8 shows a summary of the method procedure for the dynamic testing of the sustainability of the tested piping fixation system to expected earthquake loading in Egypt.
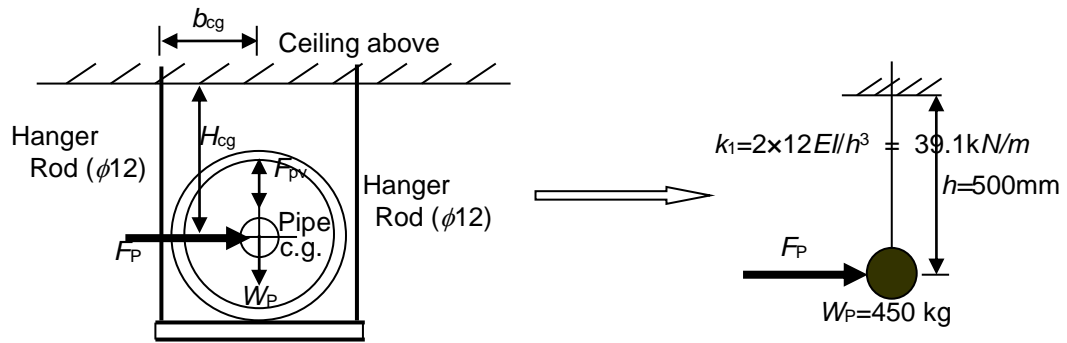


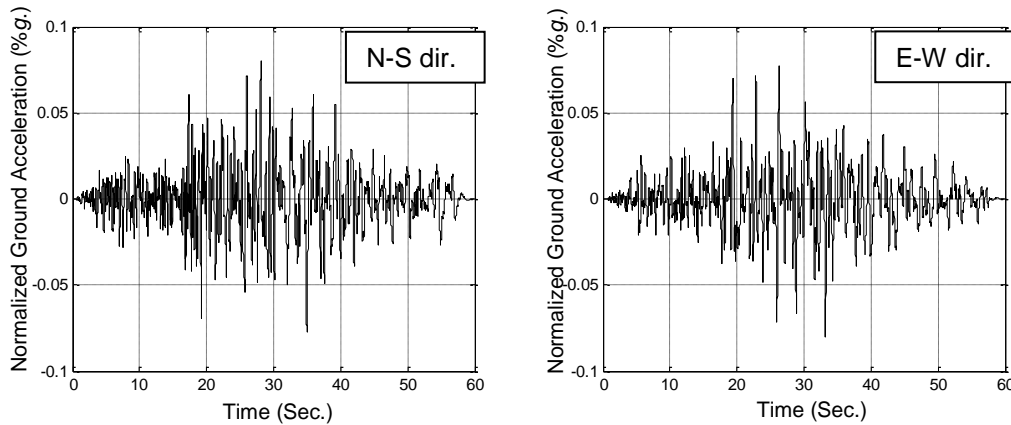**Fig. 6: Equivalent SDOF oscillator to the hanger frame of the piping system**



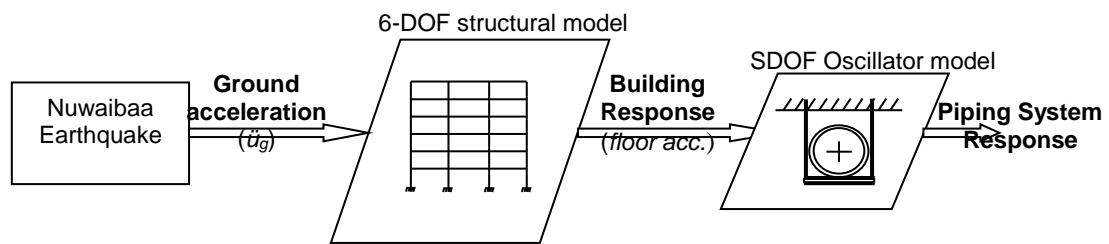**Fig. 7: Normalized Nuwaibaa earthquake ground acceleration time histories**



**Fig. 8: Procedure for the dynamic testing of the studied piping fixation system**

Furthermore, the dynamic time-domain responses of both the shear building model of the hospital building system and the SDOF oscillator model of the pipes anchorage system are obtained using a linear state space model using Matlab® software [22]. The model is summarized in the following equations. Consider a linear structural model of the form:

$$\mathbf{M\ddot{x}} + \mathbf{C}_d\mathbf{\dot{x}} + \mathbf{Kx} = \mathbf{b}f, \quad \mathbf{y} = \mathbf{C}_1\mathbf{x} + \mathbf{C}_2\mathbf{\dot{x}} + \mathbf{d}f \tag{1}$$

where $\mathbf{M}$, $\mathbf{K}$, and $\mathbf{C}_d$ are the mass, stiffness and damping matrices of the system, and $\mathbf{C}_1$, $\mathbf{C}_2$, and $\mathbf{d}$ are the output influence matrices for the displacement, velocity and the external force $f$. Thus, one can write the model in a state-space form:

$$\mathbf{\dot{q}} = \mathbf{\tilde{A}q} + \mathbf{\tilde{B}}f, \qquad \mathbf{y} = \mathbf{Cq} + \mathbf{D}f \tag{2}$$

where $\mathbf{q} = \begin{bmatrix} \mathbf{x}^\mathsf{T} & \dot{\mathbf{x}}^\mathsf{T} \end{bmatrix}^\mathsf{T}$ is the state vector, $\widetilde{\mathbf{A}}$ is the system state matrix which is dependent on the mass $\mathbf{M}$, damping $\mathbf{C}$, and stiffness $\mathbf{K}$ matrices of the structural system such that

$$\widetilde{\mathbf{A}} = \begin{bmatrix} \mathbf{0}_{n\mathrm{DOF} \times n\mathrm{DOF}} & \mathbf{I}_{n\mathrm{DOF} \times n\mathrm{DOF}} \\ \left(-\mathbf{M}^{-1}\mathbf{K}\right)_{n\mathrm{DOF} \times n\mathrm{DOF}} & \left(-\mathbf{M}^{-1}\mathbf{C}\right)_{n\mathrm{DOF} \times n\mathrm{DOF}} \end{bmatrix} \tag{3}$$

where $n$DOF is the number of degrees of freedom of the system.

In addition, $f$ is an excitation force, and $\mathbf{y}$ is a vector of measured responses. Moreover, $\widetilde{\mathbf{B}}$ is the input influence matrix, $\mathbf{C}$ is the output influence matrix for the state vector $\mathbf{q}$, and $\mathbf{D}$ is the direct transmission matrix. The latter matrices have different forms depending on the assigned type of input excitations and the desired output measurements.

In addition to that and for convenience, the pipes fixation system is tested for stability under the equivalent static force obtained from the ECP-ACC [17] as well as under that obtained from the ECP-ELF [18]. The results obtained are shown in contrast to the results from the dynamic testing. The following sections describe the ECP-ACC [17] and ECP-ELF [18] guidelines for the evaluation of the equivalent static force and the required check for stability.

**Stability of Mechanical and Electrical Details under Seismic Loads as per ECP-ACC**
The ECP-ACC [17], 2007 states that when earthquakes take place, two main forces are generated on mechanical/electrical equipments and their attachments. The forces are mainly a horizontal force, $F_\mathrm{p}$, and a vertical force, $F_\mathrm{PV}$. These forces affect the center of gravity of the electrical and mechanical component as shown in Fig. 6. Thus, the resultant force of the two forces, $F_\mathrm{p}$ and $F_\mathrm{PV}$ act on the fixation points of the equipments and the extensions in the form of a resultant tension or a resultant shear or a combination of both in a way that may damage the fixation connections. The horizontal force can be obtained by any of the following two equations [17]. The first one states that,

$$F_\mathrm{P} = \frac{a_\mathrm{P} C_a I_\mathrm{P}}{R_\mathrm{P}}\left(1 + 3\frac{h_\mathrm{x}}{h_\mathrm{r}}\right) W_\mathrm{P} \tag{4}$$

where,
   $W_\mathrm{P}$=the operating weight of the pipe, equipment or electrical system
   $a_\mathrm{P}$ =component amplification factor which is equal to 1.0
   $R_\mathrm{P}$=Component response modification factor which is equivalent to 3.0 for suspended
      piping or electrical systems
   $I_\mathrm{P}$=Importance factor and is taken equivalent to 1.5 for important structures such as
      hospitals and fire stations and equals 1.0 for other structures
   $C_a$=Seismic coefficient derived from the seismic zone, soil properties and proximity to
      known earthquake faults (UBC 1997 [20] tables 16-I, 16-Q and 16-S), and is obtained
      based upon the zone factor coefficient "Z" which is taken equivalent to 0.2 (ECP-ACC
      [17]) in case of the geographic location of Egypt
   $h_\mathrm{x}$=element or component attachment elevation with respect to ground
   $h_\mathrm{r}$=structure roof elevation with respect to ground
Meanwhile, the second equation for the evaluation of $F_\mathrm{P}$ states that,

$$F_\mathrm{P} = Z I_\mathrm{P} C_\mathrm{P} W_\mathrm{P} \tag{5}$$

where,
   $Z$= the zone factor and is taken equivalent to 0.2
   $C_\mathrm{P}$= the horizontal force factor which is taken equivalent to 0.75 for electrical and
      mechanical systems
In spite of that, the horizontal force, $F_\mathrm{p}$, has an upper and lower bounds such that

$$F_\mathrm{P} \geq 0.7 C_a I_\mathrm{P} W_\mathrm{P} \tag{6}$$

and

$$F_\mathrm{P} \leq 4 C_a I_\mathrm{P} W_\mathrm{P} \tag{7}$$

On evaluating the horizontal force, $F_p$, the resulting seismic vertical force can be as well evaluated from the equation

$$F_{PV} = \frac{F_P}{3} \tag{8}$$

Moreover, the overturning (OTM) moment on the system is calculated and compared to the resisting moment (RM). These values can be obtained knowing the horizontal and vertical active forces on the system, $F_p$ and $F_{pv}$, from the equations

$$OTM = F_P H_{c.g.} \tag{9}$$

and

$$RM = \left(W_P \pm F_{pv}\right) b_{c.g.} \tag{10}$$

where $H_{c.g.}$ is the perpendicular distance between the center of gravity of the pipe and the ceiling above it, and $b_{c.g.}$ is the perpendicular distance between the center of gravity of the pipe and each of the hanger rods (see Fig. 6).
Moreover, the design force on the hanger rods should be obtained from the equation

$$T_{eff} = \left(W_P + F_{PV}\right)/2 \tag{11}$$

**The New ECP-ELF Guidelines for Nonstructural Details**
The earthquake effect on the nonstructural details in buildings is taken as per the Egyptian code of loads, the ECP-ELF [18], as a horizontal force ($F_a$) that act in the center of gravity of the nonstructural member such that this horizontal force is calculated from

$$F_a = (S_a W_a \gamma_a)/R_a \tag{12}$$

Where $W_a$ is the weight of the nonstructural component, $\gamma_a$ is the importance factor of the nonstructural component taken as 1.5, $R_a$ is the coefficient for modifying reactions taken as 2 and $S_a$ is a coefficient related to the nonstructural component and is calculated from

$$S_a = \alpha S \left[ \frac{3(1.0 + \frac{z_a}{H})}{1.0 + (1.0 - \frac{T_a}{T_i})^2} - 0.5 \right] \geq \alpha \tag{13}$$

Where $\alpha$ is the ratio between the design ground acceleration ($a_g$) and the acceleration of gravity ($g$), $S$ is the soil coefficient, $T_a$ is the fundamental natural period of the nonstructural component. $T_i$ is the fundamental natural period of the system in the same direction of analysis, $Z_a$ is the height of the nonstructural component above the foundation level of the building, and $H$ is the full height of the building above the foundation level.

## ANALYSIS OF RESULTS

On studying the hospital building response under the normalized Nuwaibaa earthquake, it is shown that the hospital structural system responded well to the earthquake and remained stable.
Accelerations in the roof showed to be the maximum ones and went as far as $0.2g$ for the north-south direction and even beyond that to $0.21g$ in the east-west direction. Figures 9, 10 show the acceleration response of all the floors under the Nuwaibaa earthquake in both the north-south and east-west directions. In addition, the acceleration responses of the different stories of the hospital building tend to increase in a gradual manner by height such that the accelerations at the roof are bigger than those beneath.
However, since it is assumed herein that the piping fixation system is rigidly mounted to the hospital structural system at the ceiling of each floor then it would be appropriate to consider the response of each story as the dynamic excitation of the pipe fixation system fixed to that story, as explained in Fig. 8. Figures 11, 12 show the acceleration response of the pipe fixation system in each story of the hospital structure, as a percentage of the earth gravitational acceleration ($g$), when considering the building acceleration responses in both the east-west and north-south directions.
By studying the acceleration responses of the pipe fixation system at each story in the structre, it can be observed that the system shows an unstable response behavior. This is reflected in the amplification of acceleration magnitudes ongoing from the onset of the dynamic excitation till the end of the dynamic loading duration.

However, the amplification is critical in some stories rather than the others. Looking at Figs. 11, 12, one can conclude that the response amplification at the sixth story is the maximum, whereas a milder amplification is observed in the fifth and fourth stories. This is despite that the acceleration response of the 5th story in the building structure is bigger than all of those in lower stories. Similar observations can be obtained from
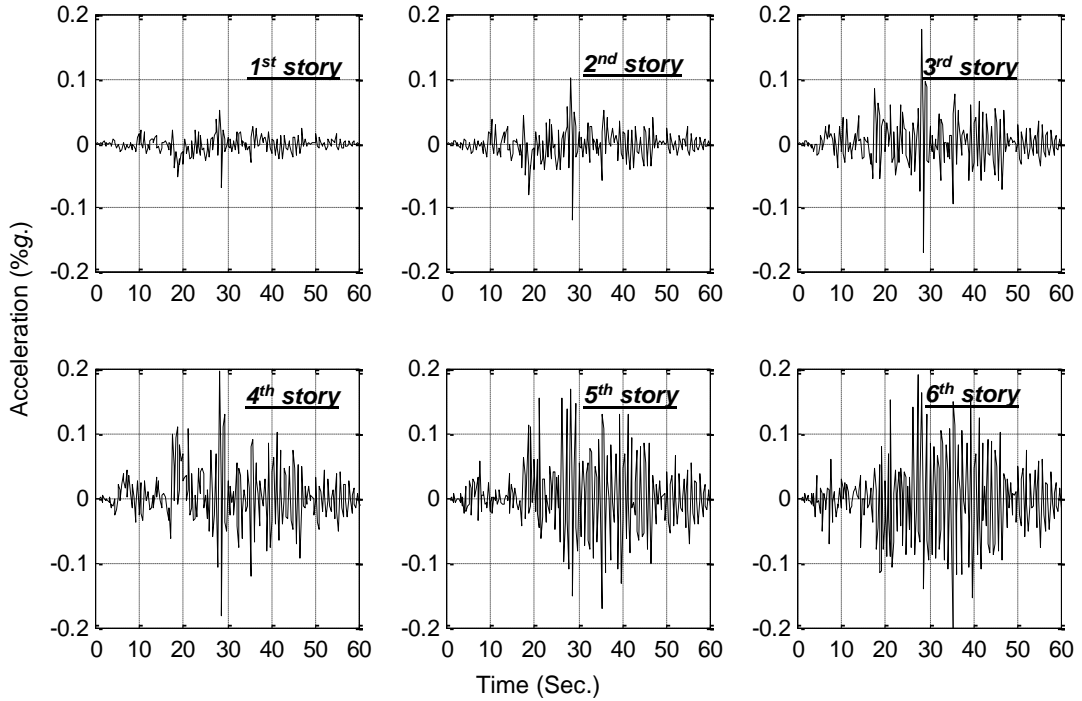


**Fig. 9: Acceleration response time history for each story of the hospital building under Nuwaibaa earthquake (N-S direction)**
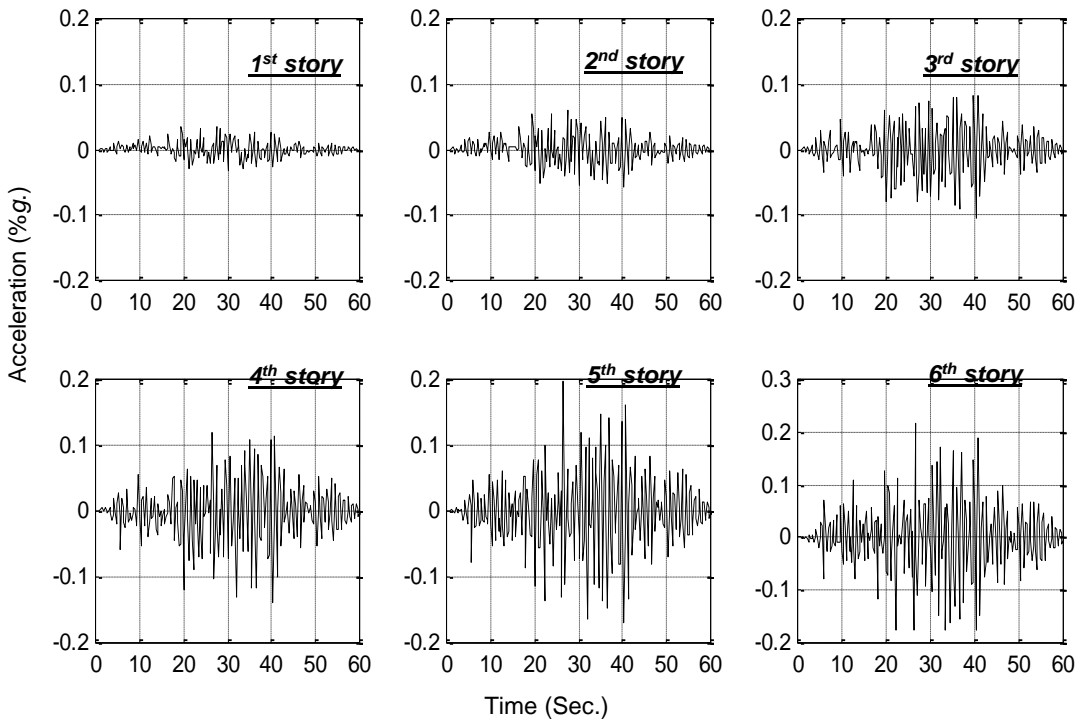


**Fig. 10: Acceleration response time history for each story of the hospital building under Nuwaibaa earthquake (E-W direction)**
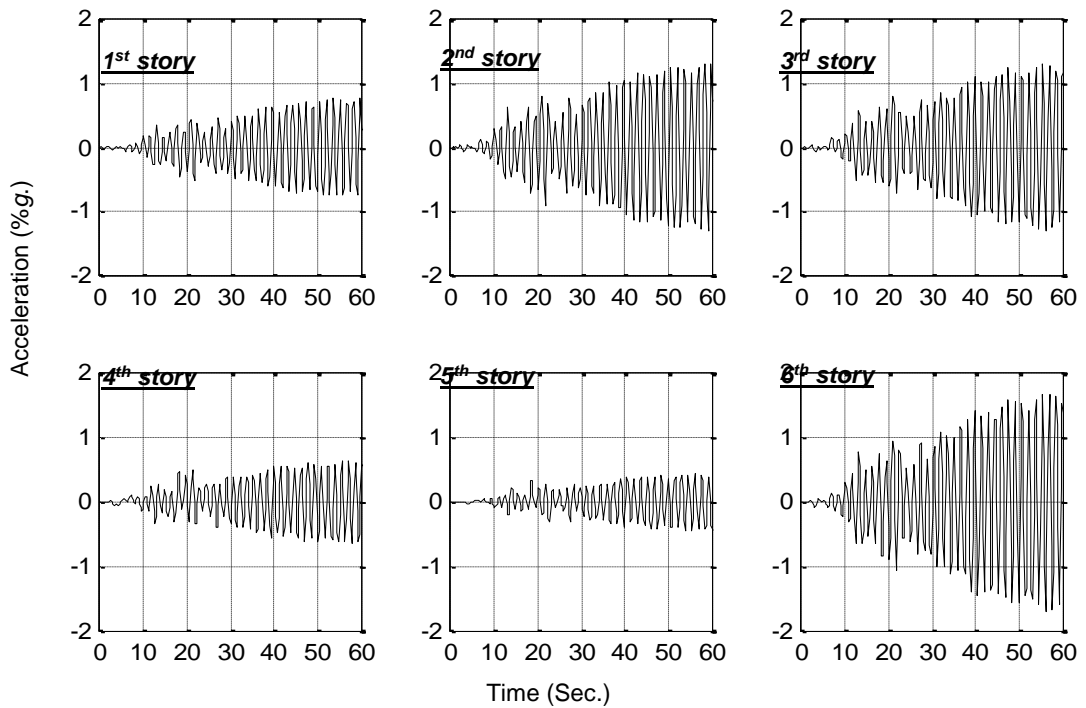
**Fig. 11: Acceleration response time history for the pipe fixation system in each story of the hospital building under Nuwaibaa earthquake (N-S direction)**
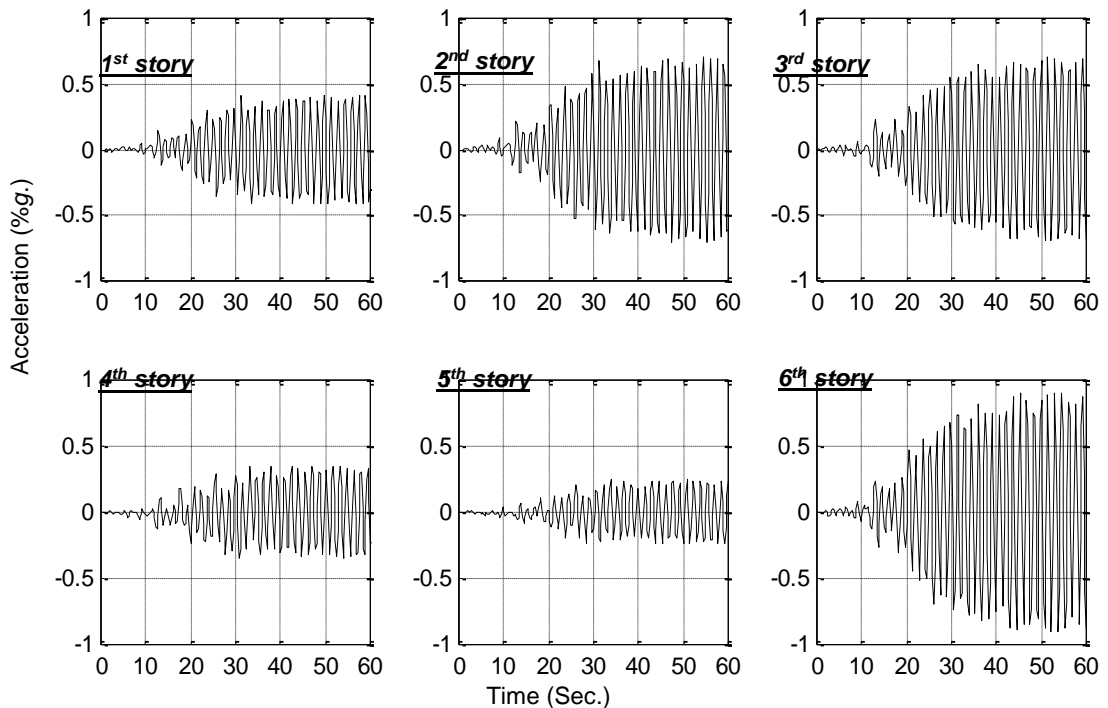


**Fig. 12: Acceleration response time history for the pipe fixation system in each story of the hospital building under Nuwaibaa earthquake (E-W direction)**

Figs. 13 and 14 showing the pipe fixation system drift relative to the ceiling in both loading directions.
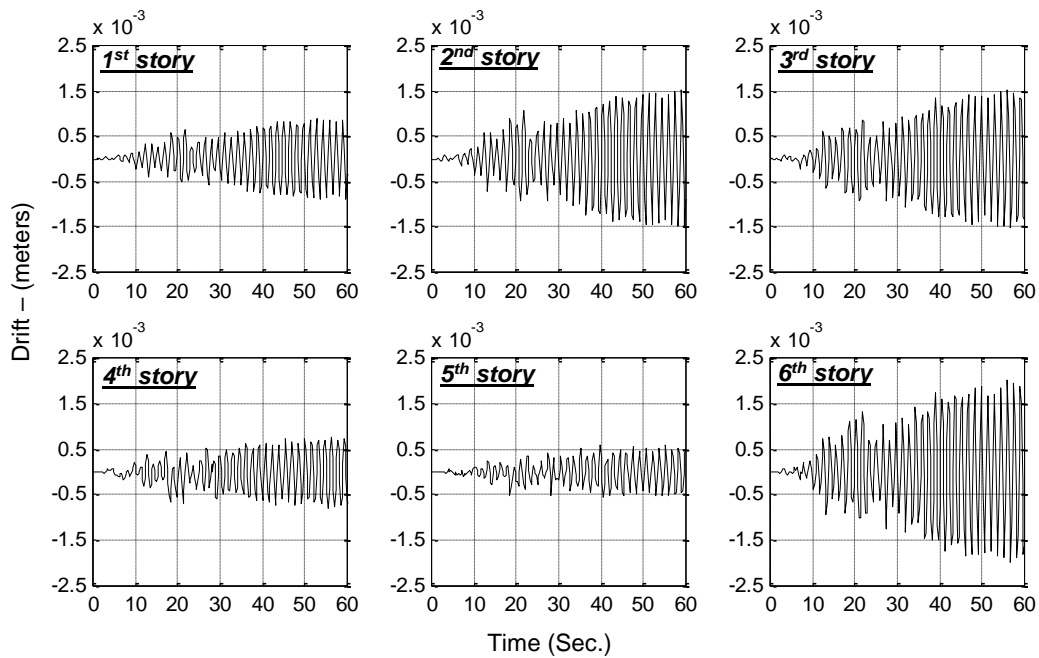
**Fig. 13: Drift response time history for the pipe fixation system in each story of the hospital building under Nuwaibaa earthquake (N-S direction)**
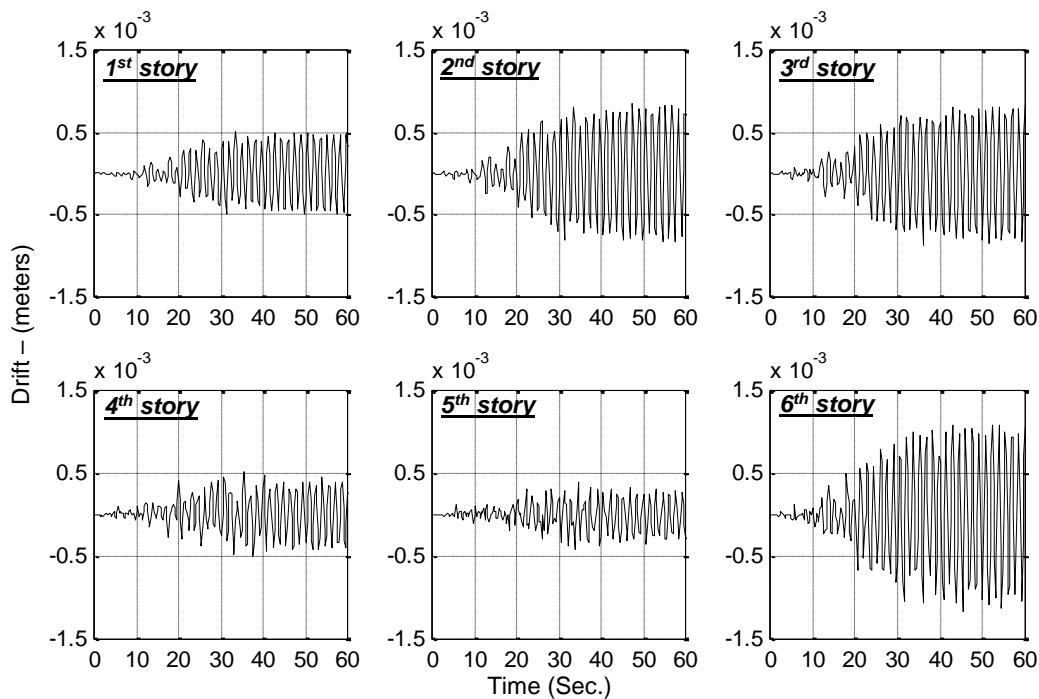


**Fig. 14: Drift response time history for the pipe fixation system in each story of the hospital building under Nuwaibaa earthquake (E-W direction)**

Based on the acceleration response time histories of each story, the frequency response (transfer function) of the hospital structural system can be obtained, as shown in Fig. 15. The damped natural frequencies of the main hospital structural system are found to be 1.05 *Hz*, 2.63 *Hz*, 4.21 *Hz*, 5.05 *Hz*, 6.44 *Hz*, and 8.55 *Hz* respectively. In contrast, the fundamental natural frequency of the pipe fixation system is found to be 4.64 *Hz*, as shown in the frequency response of the pipe fixation system in Fig. 16.
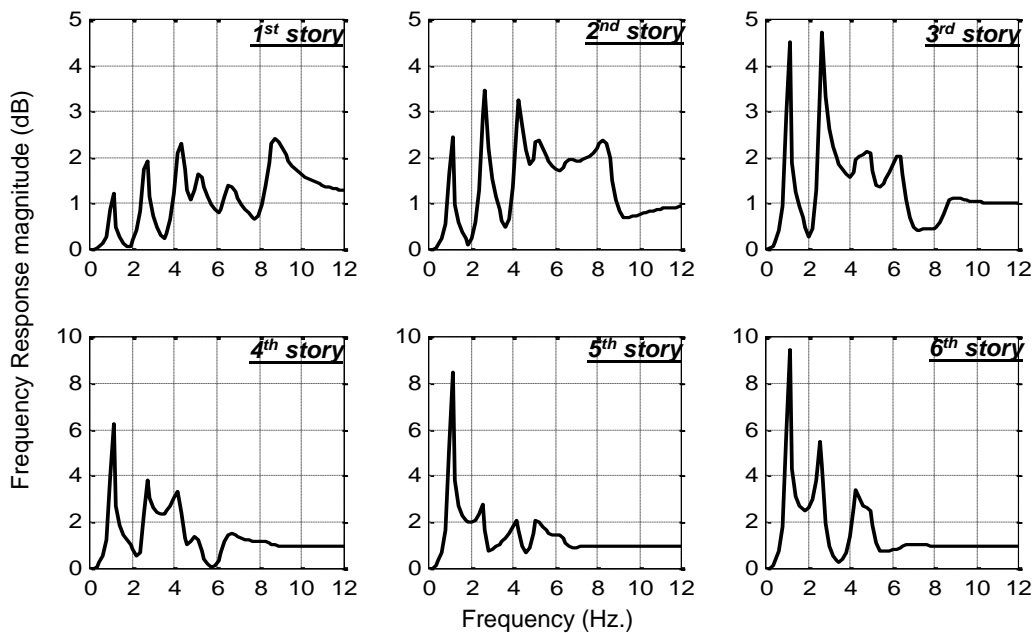
**Fig. 15: Frequency response of the hospital building based on the acceleration response time history of each story**
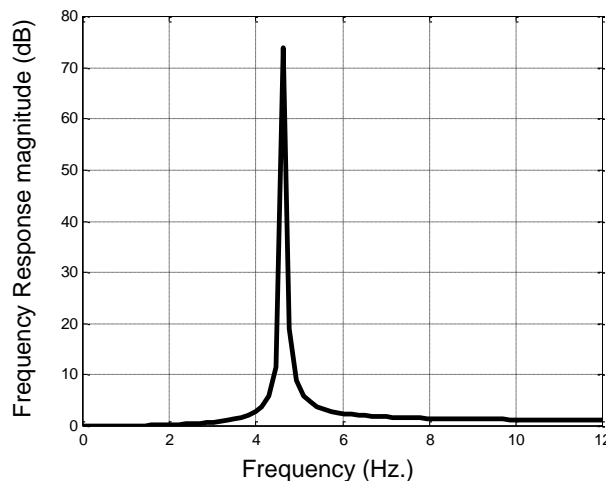


**Fig. 16: Frequency response of the pipe fixation system**

Studying the values of the natural frequencies of both the structural system and the pipe fixation system, it is clear that the fundamental mode of response of the pipe fixation system has a natural period that lies in the vicinity of the natural periods of the third and fourth modes of response of the main structural system of the hospital building. Consequently, this should explain the amplification observed in the acceleration and drift responses of the pipe fixation system where the induced excitations had frequencies that were close to the fundamental natural frequency of the pipe fixation system. Therefore, dynamic amplification took place. This is the case where the hospital building system acts like a filter to the induced ground acceleration. Such a filter amplifies only the input excitation with frequencies close to the natural frequencies of the hospital structural system thus leading to unfavorable excitation circumstances for the pipe fixation system. Moreover, looking at Fig. 15, one can conclude that the magnitude of the frequency response (transfer function) for the fourth and fifth stories in the vicinity of the third and fourth modes is smaller than other stories, thereby leading to smaller response than the other stories. Moreover, on studying the values of the peak accelerations and

drifts in the pipe fixation system at all stories of the hospital building, see, Figs. 17 and 18, it is obvious that the peaks always occurred at the roof. However, the peak accelerations and drifts are the smallest in the fifth and fourth stories respectively. This is even more reflected in the east-west excitation direction.
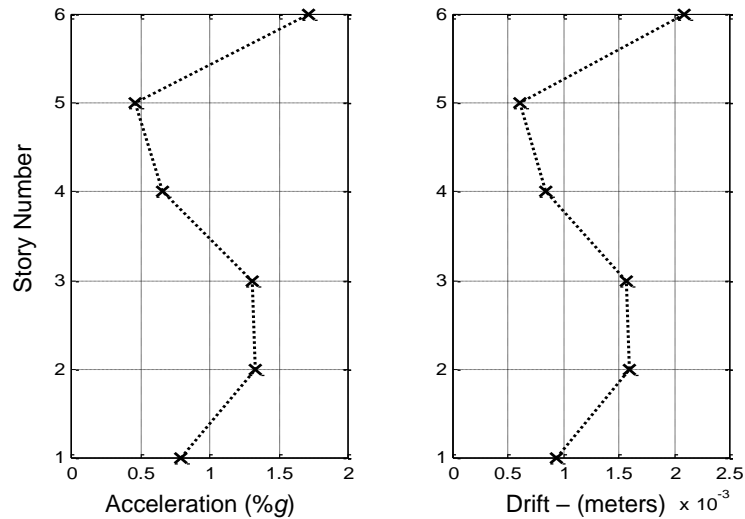


**Fig. 17: Peak accelerations and drifts of the pipe fixation system at the different stories of the hospital building under Nuwaibaa earthquake (N-S direction)**
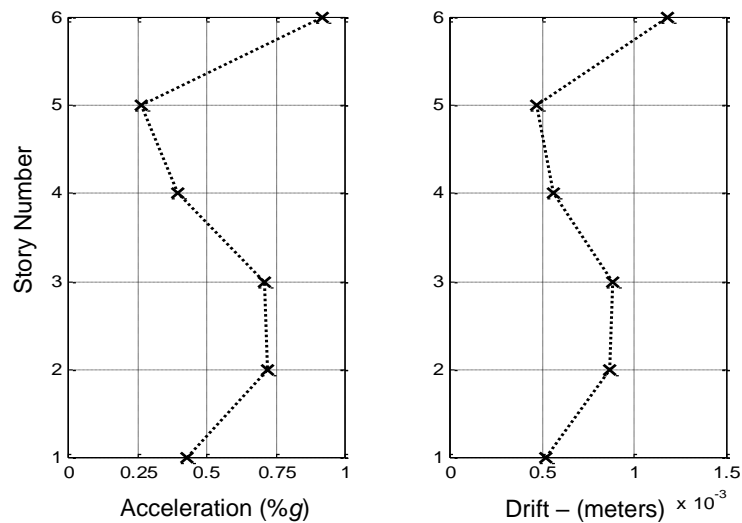


**Fig. 18: Peak accelerations and drifts of the pipe fixation system at the different stories of the hospital building under Nuwaibaa earthquake (E-W direction)**

In addition, the peak acceleration of the pipe fixation system at the roof was found to be nearly 1.7$g$ whereas the peak drift at the same level is nearly 2.15 *mm*. Such high accelerations are definitely devastating to the pipe systems and may lead to pipe breakage or failure of connecting valves between pipes. Moreover, the drift peak value though apparently small yet if the pipes connections move in an out-of-phase attitude then the resultant differential motion may be doubled. This would consequently lead to concentration of stresses at the weakest locations in the pipelines and thereby pipes breakage or leakage.

In spite of that, on applying the check of stability at the roof level based on the evaluation of the equivalent seismic lateral force explained in the ECP-ACC [17], the fixation system shows to be stable. This is the case where by calculating $F_P$ based on equation number (5) where $Z$=0.2,

$C_P$=0.75, and $I_P$=1.5 as explained earlier, and with such a weight of the pipes-fixation system of 450 *kg* for each fixation system, then the overturning moment (*OTM*) is 4050 *kg.cm* whereas the minimum resisting moment (*RM*) is equivalent to 4995 *kg.cm* for $H_{c.g.}$ and $b_{c.g.}$ values of 40 *cm* and 12 *cm* respectively.

 This, in turn, is definitely untrue as shown in the dynamic response in Figs. 11,12,13,14. This however dictates that the ECP-ACC [17] needs revision.

On the other hand, on using the recent ECP-ELF [18] the horizontal equivalent static force is equal to $F_a$=87.75 kg for the factors: $\gamma_a$=1.5, $R_a$=2, and $S_a$=0.26. The value of the coefficient $S_a$ is based upon the values of the natural periods of both the building and the nonstructural fixation system as well as the assumption that the soil under the structure is formed of rock with an upper 5 meters of weak soil (Subsoil class (A)). However, even with the recent ECP-ELF [18] guidelines followed, one can observe that the assumed overturning moment is 3510 *kg.cm* ($H_{c.g.}$=40*cm*), which is even smaller than that evaluated as per the ECP-ACC [17]. This again indicates that the fixation system of the pipes is stable which is untrue. This should again raise the requirements for revising the sections in the ECP-ELF [18] for the design of seismically resistant nonstructural details in hospitals. A good reason for that error is that the goal of code seismic design of nonstructural components has been position retention, *i.e.* keeping the nonstructural component secured so that it does not present a falling hazard during an earthquake without making an account for the damage imposed on the nonstructural component.

## CONCLUSIONS

The main task of this paper is to show the serious potential of having nonstructural components damage inside hospitals during earthquakes. This is done through studying how neglecting the dynamic properties of the main structural systems can affect the dynamic response of the attached nonstructural components. The paper focuses on the dynamic response of the fixation systems of nonstructural components in seismically excited hospitals. A 3-span 6-story hospital building with a main fire fighting piping system hung to the ceilings of the different floors is the case study.

 A simulation analysis of the 3-span 6-story building under normalized Nuwaibaa earthquake, with peak ground acceleration of 0.08*g*, is applied. The results obtained from the numerical example indicate the necessity to consider the dynamic structural parameters (*e.g.* natural periods) of the buildings main structural systems on designing a nonstructural component fixation. This should be done in order to assess the possibility of the nonstructural component responding in resonance with the response of the building. It is shown in the paper that by neglecting dynamic properties of the main system, an unstable and unfavorable dynamic response of the pipe fixation system may take place. This is the case when the fundamental natural period of the fixation system is close to any of the higher natural periods of the main building structural system. Furthermore, on studying the stability of the simulated fixation system as per the ECP-ACC [17] or even the recent ECP-ELF [18] requirements, it can be found that the fixation system is stable even when the natural periods of the main building and the fixation system are close, which is not correct. Consequently, it is advised that the Egyptian building codes [17,18] should account more for the expected amplification in the response of the nonstructural fixation systems. This in turn is done through assigning a suitable amplification factor that accounts for the proximity of the natural periods of the main and secondary systems that may occur.

## RECOMMENDATIONS

In future research, a full revision of the equivalent lateral seismic force evaluation in ECP-ACC [17] or the ECP-ELF [18] should be considered together with introducing modifications that would make such evaluations relevant to earthquakes occurring in Egypt. For example, the amplification factor, which is assumed as unity in the evaluation of the equivalent lateral seismic force, in ECP-ACC [17] needs to be revised and modified. Moreover, the Egyptian codes should account for the system ductility of nonstructural components fixation by including related factors for low, limited, and high deformability nonstructural components.

## REFERENCES

1. American National Standards Institute (ANSI), Sandard Code no: ANSI B36.10.
2. American Society of Heating, Refrigeration and Air Conditioning Engineers (ASHRAE) National Standards.
3. California Seismic Safety Commission (SSC). "Performance of essential services buildings. Background Report B7." prepared under executive order W-78-94, August, 1994.
4. California Seismic Safety Commission (SSC). "Performance of hospitals: Background Report B7." prepared under executive order W-78-94, August, 1994.
5. Chopra, A.K., Dynamics of Structures, Theory and Applications to Earthquake Engineering. Prentice Hall, Englewood Cliffs, New Jersey, 1995.
6. Federal Emergency Management Agency (FEMA). "NEHRP Recommended Provisions for Seismic Regulations for New Buildings and Other Structures, Part 2 – Commentary." Report No. FEMA 303, Washington, D.C., 1998.
7. Federal Emergency Management Agency. "NEHRP Recommended Provisions for Seismic Regulations for New Buildings and Other Structures, Part 2 – Commentary." Report No. FEMA 369, Washington, D.C., 2001.
8. Gatscher, J. A., P. J. Caldwell, R. E. Bachman, and S. R. Littler. "Seismic Qualification Testing of Nonstructural Components and Equipment." Structures, ASCE, 1-12, 2004.
9. Hall, J.F. "Northridge Earthquake Of January 17, 1994, Reconnaissance Report." Earthquake Spectra, 11 Supplement C, 1995.
10. International Code Council, International Building Code, 2006.
11. Kehoe, B. "Applying Structural Design Concepts to the Design of Nonstructural components." Structures Congress: New Horizons and Better Practices, ASCE, 2007.
12. Murray, J. "Performance of health care facilities during the Northridge earthquake: damage to water lines and failure of emergency generators." Sacramento, Office of Statewide Health Planning and Development ,CA: OSHPD, 1994.
13. Office of Statewide Health Planning and Development (OSHPD). "Draft report to the Building Safety Board on the performance of hospital buildings in the Northridge earthquake of January 17." Sacramento, CA:OSHPD, July 1994.
14. Patrucco, G., and McGavin G. "Survey of nonstructural damage to healthcare facilities in the January 17, 1994 Northridge earthquake." HMC Group. Ontario, CA, 1994.
15. Pickett, M. "17 January 1994 Northridge earthquake." Report by Dept. of Civil Engineering, University of Toledo, USA, 1994.
16. Singh, M. P., L. M. Moreschi, L. E. Suárez, and E. E. Matheu. "Seismic Design Forces I: Rigid Nonstructural Components." Journal of Structural Eng., 132(10), 1524-1532, 2006.
17. The Egyptian Code of Practice of Air Conditioning and Cooling; Ministry of Housing and Public Utilities; Research Center for Housing, Building and Physical Planning,2007.
18. The Egyptian Code of Practice for Loads and Forces Calculation in Structural Works; Ministry of Housing and Public Utilities; Research Center for Housing, Building and Physical Planning, 2003.
19. Uniform Building Code. International Conference of Building Ofiicials, Whittier, California, 1994.
20. Uniform Building Code. International Conference of Building Ofiicials, Whittier, California, 1997.
21. Villaverde, R. "Seismic design of secondary structures: State of the art." Journal of Structural Eng., 123(8), 1011–1019, 1997.
22. MATLAB® (1999). The Math Works Inc., Natick, Massachustes.

# EFFECTIVE MOMENT OF INERTIA OF REINFORCED MEDIUM STRENGTH CONCRETE BEAMS

\* **Mohamed S. Issa, Mohamed R. Mahmoud, Akram M. Torkey and Mohamed T. Mostafa**

*Housing and Building National Research Center, Giza, Egypt.*
*Faculty of Engineering, Cairo University, Giza, Egypt.*

## ABSTRACT

The effects of the loading type, and consequently the shape of the bending moment diagram, and reinforcement ratio on the effective moment of inertia needs to be studied for the case of medium strength reinforced concrete beams so that accurate estimates of the deflections are obtained. This paper deals with the short-term deflection of reinforced concrete beams made of medium strength concrete. Experimental work was carried out to investigate the effects of compression reinforcement ratio, tensile reinforcement ratio, yield strength of reinforcement, span/depth ratio and loading type on the short-term deflection. The ratio of compressive reinforcement to tensile reinforcement was found not to affect the short term deflection except before failure. It was recorded that the maximum deflection of beams with high reinforcement ratio is lower than that of similar beams with low reinforcement ratio. The grade of the tensile reinforcement generally had a small effect on the short term deflection. The increase in the span/depth ratio was associated with increase in the deflection. It was found that for the same level of total load, the deflection becomes smaller as the number of concentrated loads increases. The ACI Code [1] equation for the effective moment of inertia was modified along with another generalized equation for the effective moment of inertia to account for the effects of loading type and reinforcement ratio in the case of medium strength concrete

**Keywords:** beams, deflection, high strength, concrete, flexure, Serviceability & effective inertia.

## INTRODUCTION

The experimental work described here is designed to study the immediate deflection of high-strength reinforced concrete beams. The effects of reinforcement ratio and loading type on the short-term deflections are studied in this research. The current ACI Code equation for the effective moment of inertia does not consider the effects of loading type and reinforcement ratio. The aim of this research is to propose equations for calculating the effective moment of inertia accounting for these factors.

## EXPERIMENTAL PROGRAM

The experimental program consisted of testing eighteen beams. The ratio of the compression reinforcement to the tensile reinforcement ranged from 0.141 to 0.69. The tension reinforcement ratio ranged from 0.84% to 1.89% with yield strengths of 280 MPa and 400 MPa. All the beams were tested simply supported with span to effective depth ratio ranging from 7.41 to 27.27. Three types of loading were applied. These are midspan load, third-points loads and six equally spaced loads equivalent to uniform load. Details of the tested beams are given in Table (1.0).

## TEST SPECIMEN

Three beam cross-sections were used. These are 10*30 cm, 10*20 cm, and 10*14 cm. The

effective spans were 200 cm except for beam B21 which had a span of 300 cm.

Each beam was reinforced by two bars as tension reinforcement and two bars as compression reinfrcement. The details of these bars are found in Table (1.0). The transverse reinforcement (stirrups) was Ø8 each 6-cm center-to-center for all the tested beams.

**Table 1 : Details of the tested beams**

| Beam | Section, b × h (mm) | Load type | L/d | Reinforcement | |
|---|---|---|---|---|---|
| | | | | Bottom $A_s$ | Top $A'_s$ |
| B1 | 100 × 300 | Third points | 7.41 | 2∅16 | 2 ∅ 6, plain |
| B2 | 100 × 300 | Third points | 7.41 | 2∅16 | 2 ∅ 10 |
| B3 | 100 × 300 | Third points | 7.41 | 2∅16 | 2 ∅ 12 |
| B4 | 100 × 300 | Third points | 7.41 | 2∅18 | 2 ∅10 |
| B5 | 100 × 300 | Third points | 7.41 | 2∅12 | 2 ∅ 8, plain |
| B6 | 100 × 300 | Mid-span | 7.41 | 2∅16 | 2 ∅ 10 |
| B7 | 100 × 300 | Uni-form (6 loads) | 7.41 | 2∅16 | 2 ∅ 10 |
| B8 | 100 × 300 | Third points | 7.41 | 2∅16, plain | 2 ∅ 10 |
| B10 | 100 × 200 | Third points | 11.67 | 2∅12 | 2 ∅ 8, plain |
| B11 | 100 × 200 | Third points | 11.67 | 2∅12 | 2 ∅ 10 |
| B12 | 100 × 200 | Third points | 11.67 | 2∅10 | 2 ∅ 6, plain |
| B13 | 100 × 200 | Mid-span | 11.67 | 2∅12 | 2 ∅ 8, plain |
| B14 | 100 × 200 | Uni-form (6 loads) | 11.67 | 2∅12 | 2 ∅ 8, plain |
| B15 | 100 × 140 | Third points | 18.18 | 2∅10 | 2 ∅ 6, plain |
| B16 | 100 × 140 | Mid-span | 18.18 | 2∅10 | 2 ∅ 6, plain |
| B17 | 100 × 140 | Uni-form (6 loads) | 18.18 | 2∅10 | 2 ∅ 6, plain |
| B18 | 100 × 140 | Third points | 18.18 | 2∅10, plain | 2 ∅ 6, plain |
| B21 | 100 × 140 | Uni-Form (6 loads) | 27.27 | 2∅10 | 2 ∅ 6, plain |

## MATERIAL PROPERTIES

Steel: Normal mild steel bars of 6-,8-,10-, and 16-mm and high tensile steel bars of 10-, 12-, 16-,and 18-mm were used in these experiments. Their mechanical properties were determined from the standard tension tests.
Concrete: A mix of ordinary Portland cement, natural sand, crushed dolomite, and water was used. The admixture ADDICRETE BVF and the silica fume were also used. The proportions by weight of the concrete mix are as follows:

| Cement | :water | :crushed dolomite | :natural sand | :silica fume |
|---|---|---|---|---|
| 1 | : 0.3 | : 2.05 | : 1 | : 0.145 |

## BEAM FABRICATION

For each tested beam, the steel reinforcement cage was placed in wood form. Before installing this cage, the sides of the form were brushed by oil to avoid any bond between the concrete and form.
A mechnical rotary mixer of vertical axis and pan type was used to mix the constituent materials in the laboratory. The concrete components were weighed, and the dry mix were blended in the mixing bowl. Hence, water was gradually added to the mixing bowl until the past had formed. Then, beams were cast. At the same time, control standard specimens (cubes and cylinders) were cast in order to determine the mechanical properties of the mix. Beams were moist cured for eight days. It was then removed and stored in laboratory environment until the testing day. The test was carried out when the age of the concrete was at least one month.
The average concrete cube (150*150*150 mm) strength $f_{cu}$ was 82.3 MPa and the average concrete cylinder (150mm diameter and 300mm height) strength $f'_c$ was 64.3 MPa. The initial modulus of elasticity $E_c$ of the produced concrete was found experimentally to be equal to 26000 MPa and the splitting tensile strength was 4.32 MPa.

## TEST SET UP

All beams were tested in the Concrete Research Laboratory, Cairo University. Testing of the beams was done in a 500-ton capacity hydraulic machine. At each load increment, the vertical deflections along the span as well as the strains through the depth of the beam at midspan, were recorded. The deflections of the beams were measured using dial gages with 0.01 mm accuracy. The strains were measured using Demec gauges with gauge length of 200mm on both faces of the beams.The test was terminated when the beam showed extensive deformation. Propagation of cracks was observed and recorded and type of failure was determined.

## EXPERIMENTAL RESULTS

### Crack Patterns And Failure Mode
A summary of the test results is given in Table (2.0) and full details are available in reference [2]. The table includes the cracking load, the maximum load and the corresponding deflections at midspan. The service state load was defined as 1/1.5 the ultimate attained load. Similar characteristics were noticed for the cracking patterns of the different beams.
All beams were cracked in a flexural type mode starting by hair cracks which join and widen as the load increases up to failure. At failure, the tensile reinforcement started yielding and the crack widths increased largely. For some beams, this was followed by crushing in the top part (compression part) of the middle section of the beam.For beams subjected to third-span loads (B1, B2, B3, B4, B5, B10, B11, B12 & B15), the cracks initiated at midspan. Then the neighboring parts started to crack. Cracks were intense at midspan region and less intense at other locations. Diagonal cracks started at loads equal to 40% of the maximum load.
Intense cracks initiated in the middle parts of the beams under midspan loads (B6, B13 & B16). The crack widths were close to each other. Diagonal cracks started at load equals 49% of the maximum load.

**Table 2 : Test Results of the studied beams**

| Beam No. | $f_{cu}$ (N/mm²) | Service state | | Cracking state | | Maximum state | |
|---|---|---|---|---|---|---|---|
| | | load (kN) | deflection (mm) | load (kN) | deflection (mm) | Load (kN) | deflection (mm) |
| B1 | 83.0 | 88.09 | 3.30 | 30.00 | 0.748 | 137.20 | 5.67 |
| B2 | 83.0 | 88.09 | 3.41 | 30.00 | 0.829 | 140.00 | 11.21 |
| B3 | 83.0 | 88.09 | 3.49 | 30.00 | 0.70 | 134.00 | 7.89 |
| B4 | 81.5 | 122.18 | 4.05 | 40.00 | 0.942 | 162.00 | 6.43 |
| B5 | 81.5 | 58.76 | 2.99 | 25.00 | 0.653 | 89.70 | 8.12 |
| B6 | 81.5 | 58.14 | 3.52 | 15.00 | 0.654 | 95.00 | 9.12 |
| B7 | 82.6 | 116.26 | 3.90 | 15.00 | 0.563 | 200.00 | 7.02 |
| B8 | 82.6 | 61.31 | 2.0 | 28.00 | 0.873 | 107.08 | 6.79 |
| B10 | 82.0 | 36.69 | 6.08 | 15.20 | 1.75 | 44.12 | 7.61 |
| B11 | 82.0 | 36.69 | 8.46 | 11.30 | 1.0 | 40.10 | 19.02 |
| B12 | 82.0 | 22.48 | 3.81 | 11.80 | 0.988 | 35.04 | 10.84 |
| B13 | 82.0 | 24.22 | 4.28 | 10.00 | 1.18 | 36.40 | 9.06 |
| B14 | 82.0 | 48.39 | 5.28 | 10.00 | 0.53 | 80.00 | 16.9 |
| B15 | 82.0 | 14.57 | 7.02 | 4.50 | 1.18 | 24.72 | 17.54 |
| B16 | 83.0 | 9.62 | 4.75 | 6.10 | 2.4 | 15.80 | 11.86 |
| B17 | 82.6 | 19.22 | 7.32 | 5.40 | 1.39 | 30.00 | 16.62 |
| B18 | 81.5 | 10.61 | 4.38 | 5.60 | 2.06 | 16.38 | 12.19 |
| B21 | 82.6 | 12.43 | 13.44 | 3.75 | 2.88 | 17.00 | 18.85 |

For beams under uniform loads (B7, B14 & B17), uniform and intense cracks occurred in the middle zones of the beams. The crack widths were close to each other. Diagonal cracks appeared at 55% of the maximum load.Uniform and spread cracks along the span were observed for beams with mild steel (B8 & B18). The cracks were regularly spaced. The spacing between cracks was larger than for the other beams. Diagonal cracking occurred at 35% of the maximum load.Beams with large span-to-depth ratios (B21), had initial cracks relatively deeper than that for the other specimen.

**Load-Deflection Relationship**
A general observation is that the curves start with steep gradient until the onset of the flexural tensile cracking where the slopes reduce. After this point the load-deflection curves remain fairly linear until the strain in steel reaches the yielding value. Thus, the experimental load verses deflection curves are typically bilinear with the exception of the slightly curved upper part.

**Effect Of Compression Reinforcement On Deflection**
Figure 1.0 for beams B10 & B11 prove that the ratio of the area of compressive reinforcement to the area of tensile reinforcement had a minimal effect on the short-term deflection of the beams of this research. However, at the stage of failure beams of higher compressive reinforcement ratio recorded higher inelastic deflections.

**Effect Of Tensile Reinforcement Ratio**
The two beams B10 & B12 of Figure 2.0 show that the deflection of the beams of higher tensile reinforcement ratio is larger under small loads. For example, the maximum deflection of beam B10 with reinforcement ratio of 1.33% was 30% lower than the maximum deflection of beam B12 with reinforcement ratio of 0.924%.

**Effect Of Yield Strength Of Main Reinforcement**
The load-deflection curves for beams with different nominal yield strengths of the tensile
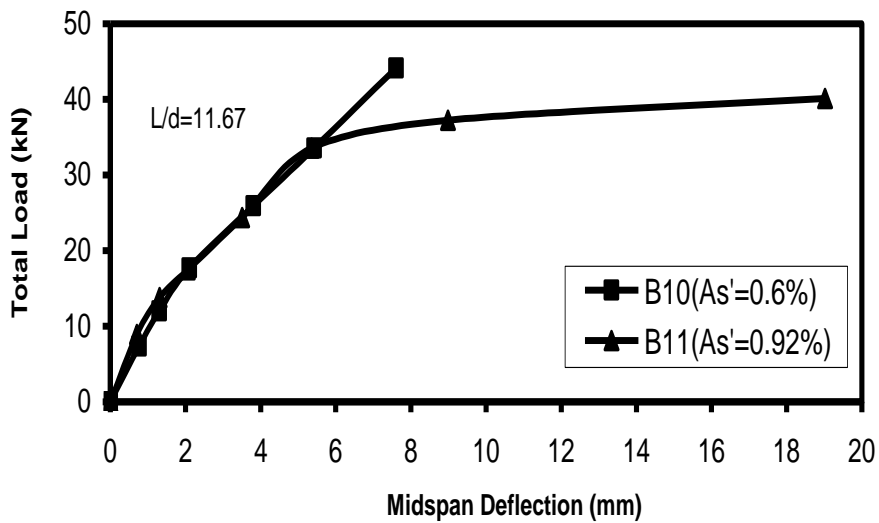
**Fig 1 : load deflection curves for beams with different compression reinforcement ratios**
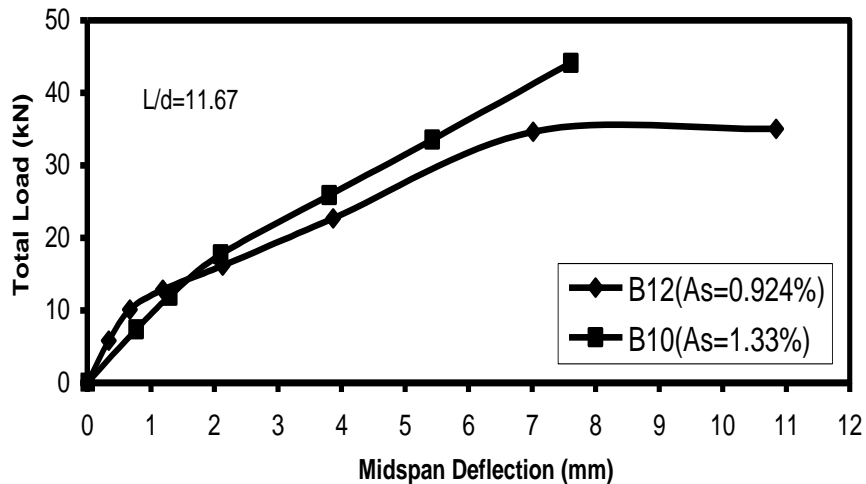


**Fig 2 : load deflection curves for beams with different tension reinforcement ratios**

reinforcement are shown in Figure 3.0 for beams B15 & B18. The curves show that the grade of tensile steel did not have a noticeable effect on the short term load-deflection curves of the beams of this research.
 Except that the maximum deflections for beams with high grade steel was generally higher than that of beams with mild steel.

**Effect Of Loading Type**
The effect of loading type can be seen clearly by comparing beams B15, B16 & B17 of Figure4.0. From all of these curves, the deflection response becomes stiffer as the number of loads increases, keeping all the other parameters constant.

**Effect Of Span/Depth Ratio**
As expected the comparison of the beams of Figure 5.0 shows that the increase in the span/depth ratio is accompanied by increase in the deflection.
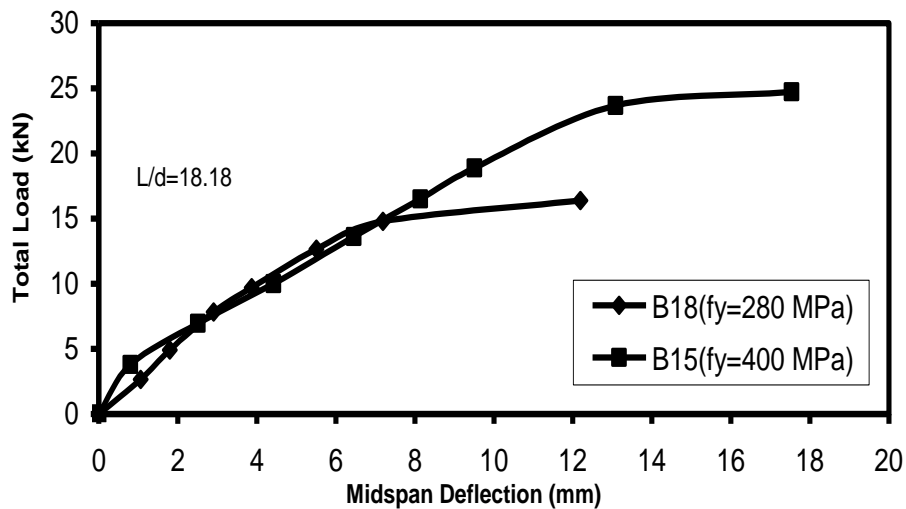
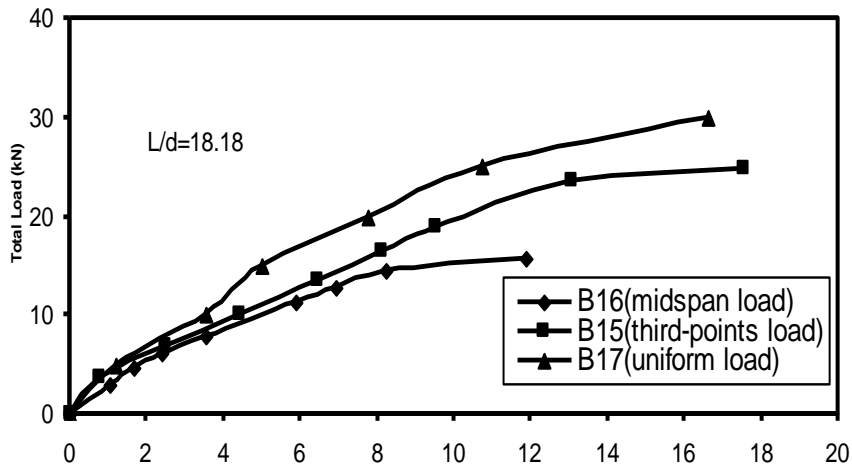**Fig 3 : load deflection curves for beams with tension reinforcements fo different yield strengths**



**Fig 4 : Load-deflection curves for beams under different loading types**

## EFFECTIVE MOMENT OF INERTIA ($I_e$)

### Effect Of Reinforcement Ratio And Loading Type

The main factors affecting the short-term deflection of a beam are the magnitude and type of load, span length, end condition, shape of cross–section, type of material, reinforcement and cracking [3]. To predict the deflections of reinforced concrete flexural members successfully, the proposed model should consider these factors. The calculation of the moment of inertia of a beam is an important task for the determination of the deflection, since it changes from the

gross inertia for uncracked sections to the cracked inertia for the fully cracked sections. The ACI Building Code adopted the reference [3] expression for the effective moment of inertia $I_e$ of a simply supported, uniformly loaded, rectangular or tee beams. This equation does not consider the loading type which means that the effective moment of inertia is the same for all identical beams loaded to the same level of moment, regardless the type of applied loading.

gross inertia for uncracked sections to the cracked inertia for the fully cracked sections. The ACI Building Code adopted the reference [3] expression for the effective moment of inertia $I_e$ of a simply supported, uniformly loaded, rectangular or tee beams. This equation does not consider the loading type which means that the effective moment of inertia is the same for all identical beams loaded to the same level of moment, regardless the type of applied loading.
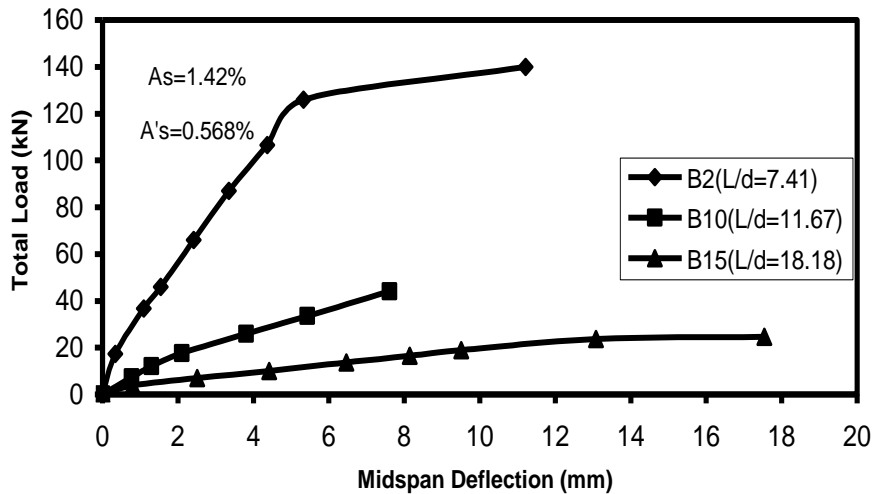
**Fig 5: Load-deflection curves for beams with different span/depth ratios**

The variation of the experimental effective inertia with the level of loading for beams under different loading types is given in Figure 6.0 where the cracking moment is calculated according to equation (1.0) which will follow and the experimental inertia is calculated according to equation (3.0) which will also follow. From this figure it is clear that for the same moment level, $I_e$ varies with the type of loading. The variation of the experimental effective moment of inertia with the load level for beams having different reinforcement ratios is presented in Figure7.0. From this figure, it is clear that sections with higher reinforcement ratios record higher $I_e$ values. Three types of loading were considered in this study, which include: midspan and third–point concentrated loads, and uniformly distributed load. The following sections present a modification to the ACI Building Code equation for the effective moment of inertia to account for the effect of these load types and for the effect of reinforcement ratio.
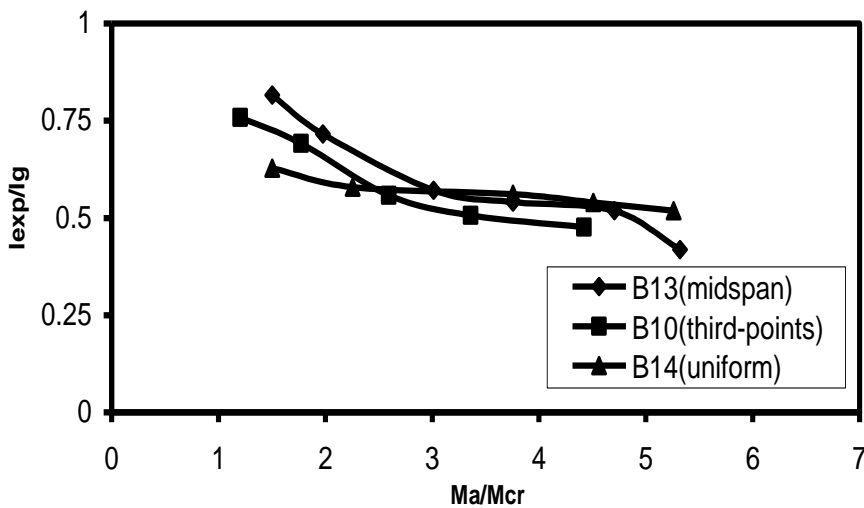


**Fig 6: Variation of Iexp/Ig with Ma/Mcr for beams under different loading types and of span-to-depth ratio of 11.67**

**Proposed Formula For The Effective Inertia $I_e$**
To calculate the effective inertia, the $M_a$, $M_{cr}$, $I_g$ and $I_{cr}$ need to be determined.
The cracking moment was calculated from the equation
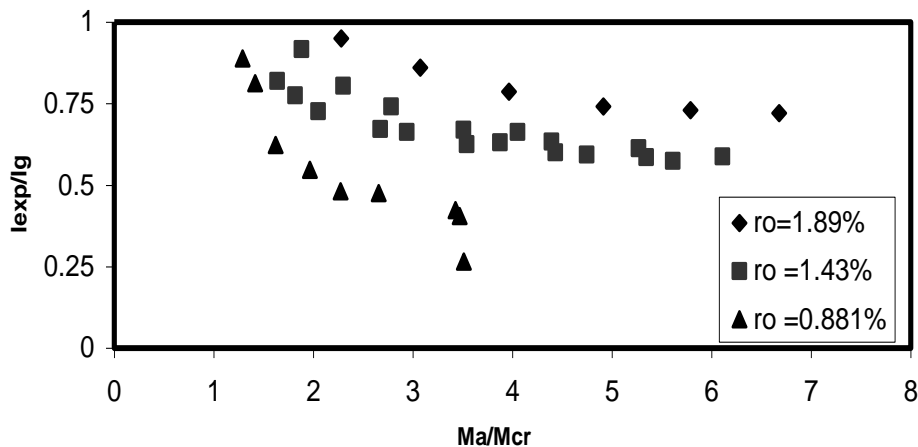
$$M_{cr} = \frac{f_r}{y_t} I_g \qquad (1.0)$$

**Fig 7: Variation of Iexp/Ig with Ma/Mcr for beams under third-points loads and with different reinforcement ratios**

where  $f_r$=the modulus of rupture

$$f_r = 0.62\sqrt{f_c^{'}} \text{ MPa} \tag{2.0}$$

$y_t$=the distance from the centroid to the extreme fiber in tension
$y_t$=h/2
Ig=moment of inertia of the concrete section
Ig=bh$^3$/12
f'c=the compressive strength of the concrete cylinder
b=width of the section
h=total depth of the section

The values of the experimental moment of inertia were determined from the elastic deflection equation as

$$I_{\exp} = \frac{KM_aL^2}{E_c\Delta_{\exp}} \tag{3.0}$$

where   $M_a$= maximum moment in the member at the loading stage for which I$_{exp}$ is being computed
L=beam span
E$_c$=modulus of elasticity of concrete=26000 MPa
$\Delta_{exp}$=measured deflection at midspan of the beam at the different load levels
$K$= constant which depends on the type of loading and end condition.

$K$= 1/12        for simply supported beams under midspan concentrated loads.

$K$= 23/216        for simply supported beams under third-point concentrated loads.

$K$=30.3/288        for simply supported beams under six uniformly spaced concentrated loads (equivalent to uniform load).

The difference between the experimental effective inertia and the effective moment of inertia calculated using the ACI Code equation can be seen clearly from Figure 8.0. The average of the absolute errors is 1040.2 cm$^4$ where the error is defined as the difference between the I$_e$ according to the ACI Code and the I$_e$ obtained from the experimental work. The standard deviation of theses errors is 1216.2 cm$^4$.
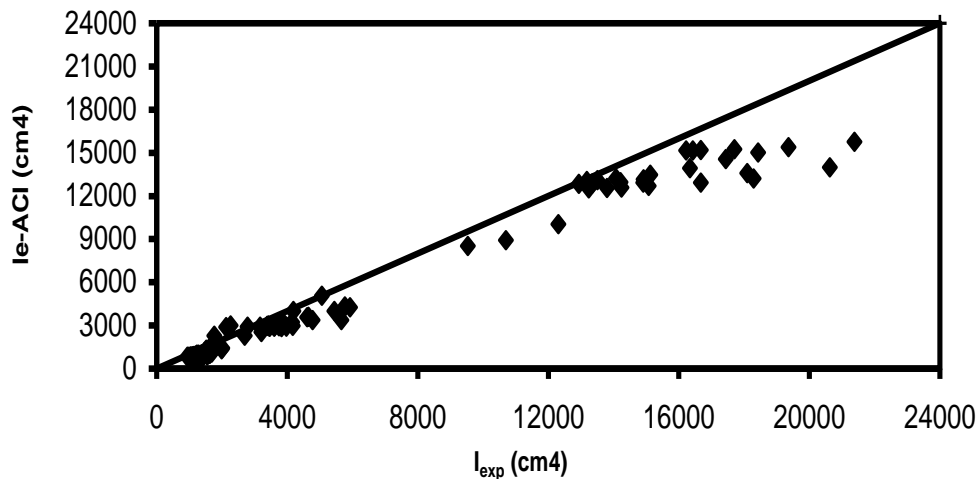
**Fig 8: Comparison between experimental moment of inertia and effective moment of inertia computed according to ACI Code**

The equation of the ACI Building Code for the effective moment of inertia is modified to the following form.

$$I_e = \left(\frac{M_{cr}}{M_a}\right)^m I_g + \left[1 - \left(\frac{M_{cr}}{M_a}\right)^m\right] I_{cr} \tag{4.0}$$

where the power m accounts for the type of loading and reinforcement ratio. The values of the unknown power m are evaluated experimentally at each load level for each beam based on the above equation.

This was done after substituting for $I_e$ in equation (4.0) by $I_{exp}$ as calculated by equation (3.0) for each load level of each beam. After which the unknown m was obtained.

Looking into the variation of the power m with the load level for the beams under midspan load (B13 & B16), a value of 1.08 appears to be appropriate to it. For beams subjected to uniform loads (B14, B17 & B21) an average value of 1.31 for m is found. It should be noted that the average reinforcement ratio for all the above-mentioned cases is 1.43%. Performing similar study for beams under third-points loads, it can be noted that "m" is inversely proportional to the reinforcement ratio (ρ). A straight line fitting gives the following relation for beams under third-points loads

$m = 2.34 - 0.749\,\rho$ (5.0)

where ρ is substituted for as a percentage.

To further extend the range of available data, two simply supported beams were solved for the deflection under midspan load and two simply supported beams were solved under uniform load using a finite element program. The reinforcement ratios for the beams were 1.89% and 0.881%. The values of 'm' were calculated for these beams. Doing a straight line curve fitting the following equation can be obtained for midspan load

$m = 1.5 - 0.522\,\rho$ (6.0)

and the following equation can be obtained for uniform load

$m = 1.43 - 0.457\,\rho$ (7.0)

Thus the final shape of the equation of the effective moment of inertia, which is called model 1, is as follows:

For third-points loads, $I_e = \left(\dfrac{M_{cr}}{M_a}\right)^{2.34-0.749\rho} I_g + \left[1 - \left(\dfrac{M_{cr}}{M_a}\right)^{2.34-0.749\rho}\right] I_{cr}$ (8.0)

For midspan loads, $I_e = \left(\dfrac{M_{cr}}{M_a}\right)^{1.5-0.522\rho} I_g + \left[1 - \left(\dfrac{M_{cr}}{M_a}\right)^{1.5-0.522\rho}\right] I_{cr}$ (9.0)

For uniform loads, $I_e = \left(\dfrac{M_{cr}}{M_a}\right)^{1.43-0.457\rho} I_g + \left[1 - \left(\dfrac{M_{cr}}{M_a}\right)^{1.43-0.457\rho}\right] I_{cr}$ (10.0)

A comparison of the experimental inertia and the computed effective moment of inertia according to the current model (model 1) at the different load levels for all the beams of this project is presented in Figure 9.0. The obtained error is 60.2% lesser than that of the equation of the ACI. The standard deviation is 590.2 cm[4].

**Proposed Formula For The Effective Inertia $I_e$ Based On The Cracked Length $L_{cr}/L$**
The proposed model is for simply supported rectangular and tee beams. It accounts for the effect of the loading type by considering the variation of the cracked length $L_{cr}$. This model follows the work by reference [4] and reference [5] for normal strength concrete.
The cracked length is the beam segment over which the working moment exceeds the cracking moment $M_{cr}$.
The equations used to calculate the cracked length can be determined using the fundamentals of structural analysis. The variation of the theoretical cracked length ratio, and consequently the effective inertia, with the level of loading for the different loading types can be shown from the experimental work. It can be found that at the same moment level the cracked length varies with the type of loading.
From this discussion the model for the estimation of $I_e$ should take into account the severity of crack propagation and the extension of cracking along the beam. Therefore, the proposed model is given in the form
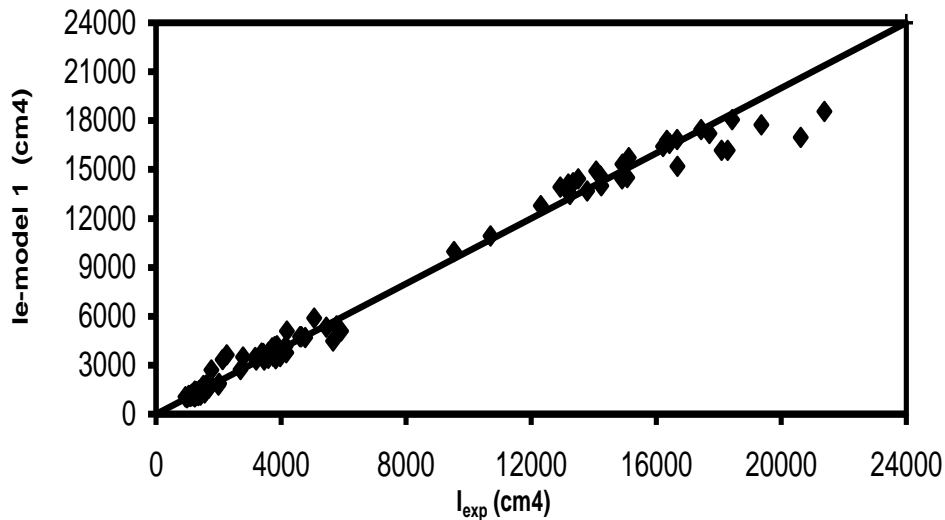


**Fig 9: Comparison between experimental moment of inertia and effective moment of inertia computed according to model 1**

$$I_e = \left(\frac{L_{cr}}{L}\right)^r I_{cr} + \left[1 - \left(\frac{L_{cr}}{L}\right)^r\right] I_g$$ (11.0)

Replacing the $I_e$ in the above equation by $I_{exp}$ from equation (3.0) at each load level, the value of the experimental r can be calculated.
The variation of the power r with the $L_{cr}/L$ ratio for beams under midspan load (B13, B16 & B20)can be given by the equation r=1.41$L_{cr}/L$. For beams subjected to uniform loads (B14, B17 & B21), this variation is described by the equation r=2.12$L_{cr}/L$. Performing similar study for

beams under third-points loads and fitting a straight line to the values of the power r against $L_{cr}/L$ for the different reinforcement ratios we obtain

$r= 1.48\ \rho\ L_{cr}/L$ (12.0)

where $\rho$ is substituted for as a percentage.

To further extend the range of available data, the finite element solutions for the previous four beams were used. Now incorporating the effect of reinforcement ratio, the following equation is obtained for the case of beams under midspan loads

$r= 1.64\ \rho\ L_{cr}/L$ (13.0)

and the following equation is obtained for the case of beams under uniform loads

$r= 8.52\ \rho\ L_{cr}/L$ (14.0)

Now, the effective moment of inertia take the following forms:

For third-points loads, $I_e = \left(\dfrac{L_{cr}}{L}\right)^{1.48\rho\frac{Lcr}{L}} I_{cr} + \left[ 1 - \left(\dfrac{L_{cr}}{L}\right)^{1.48\rho\frac{Lcr}{L}} \right] I_g$ (15.0)

For midspan loads, $I_e = \left(\dfrac{L_{cr}}{L}\right)^{1.64\rho\frac{Lcr}{L}} I_{cr} + \left[ 1 - \left(\dfrac{L_{cr}}{L}\right)^{1.64\rho\frac{Lcr}{L}} \right] I_g$ (16.0)

For uniform loads, $I_e = \left(\dfrac{L_{cr}}{L}\right)^{8.52\rho\frac{Lcr}{L}} I_{cr} + \left[ 1 - \left(\dfrac{L_{cr}}{L}\right)^{8.52\rho\frac{Lcr}{L}} \right] I_g$ (17.0)

To evaluate the accuracy of the proposed model which is called model 2, a comparison of the $I_{exp}$ and the computed $I_e$ according to this model for different load levels of all the beams of this research is presented in Figure 10.0. The obtained average error is 41.5% smaller than that of the ACI code equation and the standard deviation is 803.3 $cm^4$.
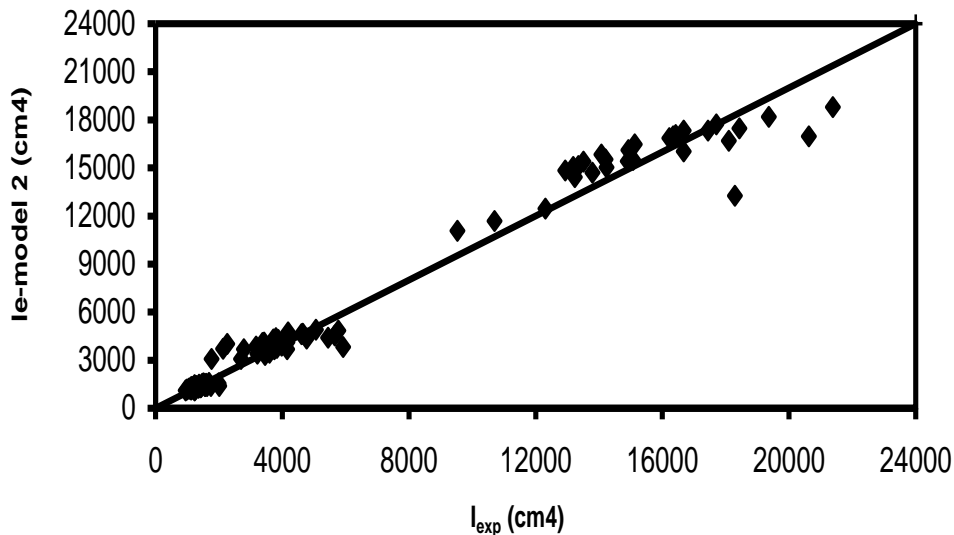


Fig 10 :  Comparison between experimental moment of inertia and effective moment of inertia computed according to model 2

## CONCLUSIONS

1.   The effective moment of inertia is influenced by the loading type and the reinforcement ratio.
2.   The ACI Code equation for the effective moment of inertia was modified by using the exponent m instead of the power "3". Applying the modified equation, model 1, to the

beams of the current experimental work the obtained error was 60.2% lesser than when using the original equation of the ACI Code.

3. The equation proposed by references 4 and 5 for the effective moment of inertia was modified and was refered to as model 2. Using the modified equation to calculate the effective moment of inertia of the beams of this paper the obtained average error was 41.5% smaller than that obtained using the ACI Code equation.

## REFERENCES

1. ACI Committee 318 (2002), "Building Code Requirements for Structural Concrete (ACI 318M-02) and Commentary (ACI 318RM-02)", American Concrete Institute, Detroit, USA.
2. Issa, M. S. (2003), "Immediate and Sustained Deflection of High Strength Reinforced Concrete Beams", PhD Thesis, Cairo University, Faculty of Engineering.
3. Branson, Dan E. (1968), "Design Procedures for Computing Deflections", ACI Journal, Title No.65-53, pp. 730-742.
4. Al-Zaid, Rajeh Z., Al-Shaikh, Abdulrahman H. and Abu-Hussein, Mustafa M. (1991), "Effect of Loading Type on the Effective Moment of Inertia of Reinforced Concrete Beams", ACI Structural Journal, 88(2), pp. 184-190.
5. Al-Shaikh, Abdulrahman H. and Al-Zaid, Rajeh Z. (1993), "Effect of Reinforcement Ratio on the Effective Moment of Inertia of Reinforced Concrete Beams", ACI Structural Journal, 90(2), pp. 144-149.

# FINITE ELEMENT ANALYSIS OF COLD FORMED STEEL C-PURLINS WITH INCLINED WEB

**\* Dr. A. M. Fadel**

*Associate Professor, Housing and Building National Research Center, Cairo, Egypt*
*Email: ashfadel@yahoo.com*

## ABSTRACT

Cold-formed steel C-shapes are commonly used as purlins carrying loads not parallel to their webs in most cases and leading to stresses in both major and minor directions of the sections. The author had carried out previous studies which showed the effect of web inclination on the overall behavior of the C-shaped purlins and compared the results with C-shaped purlins having perpendicular webs[1]. The previous study has been carried out using the finite strip method. In this research, the behavior of C-purlins having perpendicular and inclined webs have been carried out using finite element analysis to show the effect of web inclination on the capacity of the C-purlins. The members selected are widely used in practice and have (h/t) that varies from 66 to 133. The thicknesses of the used C -purlins are 1.5, 2.0, 2.5 and 3.0 mm. The height of the used sections is 200 mm. Four different sections have been studied to show the effect of the web inclination angle on the behavior of the C-purlins. The web angle varies from 0 to 11 degrees. The finite element analysis method has been used to compare the overall behavior of C-purlins having perpendicular and inclined webs. Results are discussed and recommendations are given for the use of the C-purlins having inclined webs.

**Keywords:** Cold formed, C-purlins, inclined web, Local Buckling, Distortional Buckling, Overall Buckling, Finite Element.

## INTRODUCTION

Cold-formed steel members provide substantial savings due to their high strength-to-weight ratio. As a result, they have become very popular in the construction of industrial, commercial, and factory buildings.

An important advantage of cold-formed steel is the greater flexibility of cross-sectional shapes and sizes available to the structural steel designer.

Through cold-forming operations, steel sheets, strips or plates can be shaped easily and sized to meet a large variety of design options. Such a large number of design possibilities create a very important challenge of choosing the most economical cold-formed shape in the design of steel purlins. Many researches had been carried out to obtain the optimum dimension of sections used as purlins [2]. Thorough analytical and experimental works had been carried out recently to enhance the design expressions stated by international codes for both C and Z sections and to distinguish between local, distortional and lateral-torsional buckling [3]. Previous researches had been carried out by the author using the finite strip analysis of both C and Z purlins [4].

In this research, finite element analysis is carried out to study the behavior of C-Purlins having inclined web and compare the behavior with the C-purlins having web perpendicular to flanges. The behavior of the C-purlins having webs inclined by $3°$, $6°$, $9°$ and $11°$ with the vertical axes was investigated and discussed. An approach for the effective use of the C-purlins to carry the major part of the applied load directly in their major directions and minimizing the effect of the lateral component of the applied load, which acts along the minor direction of the purlins, is introduced.

## BUCKLING MODE SHAPES

### Local, Distortional and Global Buckling Mode Shapes

Figure 1 shows the various buckling modes; A) Local buckling, B) Distortional buckling and C) Global Buckling. Local Buckling involves significant distortion of the cross-section, but this distortion involves only rotation, with no translation at the fold lines of elements with edge-stiffened flanges. For distortional buckling, both rotation and translation at the fold lines of the elements shall take place. The global or "Euler" buckling mode includes flexural, torsional, or flexural-torsional for columns, and lateral torsional for beams.
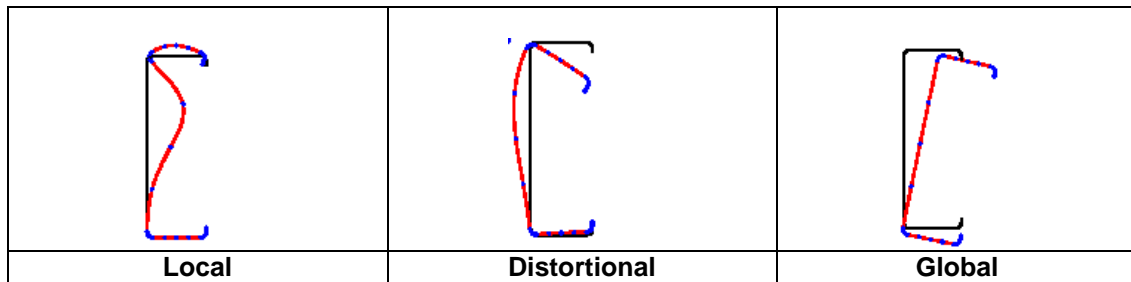


| Local | Distortional | Global |

**Fig. 1: Local, Distortional and Global (Flexural) Buckling Modes in Bending**

## ANALYSIS OF COLD FORMED C-PURLINS HAVING PERPENDICULAR OR INCLINED WEBS

Figure 2 shows the layout of purlins located above rafter of portal frame for both cases of purlins having perpendicular web and purlins having inclined webs. Figure 2 (a) shows the load acting on the purlins having perpendicular web; the resultant R in this case shall be resolved to two components as shown in the figure. Figure 2 (b) shows the load acting on the purlins having inclined webs; the major part of the resultant R in this case shall be carried directly in the major direction of the purlin. Note that the web inclination angle of the purlin is the same as the angle of inclination of the rafter. Cold formed C-purlins with 4 different thicknesses 1.5, 2 , 2.5 and 3 mm have been used in the analysis, each of them have web angle with the vertical axis of 0, 3, 6, 9 and 11 degrees, which makes the total number of sections analyzed to be 20 sections. Table 1 and Fig. 3 show the notations of the sections used which can be summarized as follows: For the case of load acting parallel to the web; the sections names are 3C-0, 6C-0, 9C-0 and 11C-0 for web angles 3, 6, 9 and 11 degree with the vertical respectively. For load making angles 3, 6, 9 and 11 degrees with the web; the sections notations are 3C, 6C, 9C and 11C, respectively. The notation 200C20 (e.g.) means that the height of the C-section is 200 mm, the thickness is 2 mm
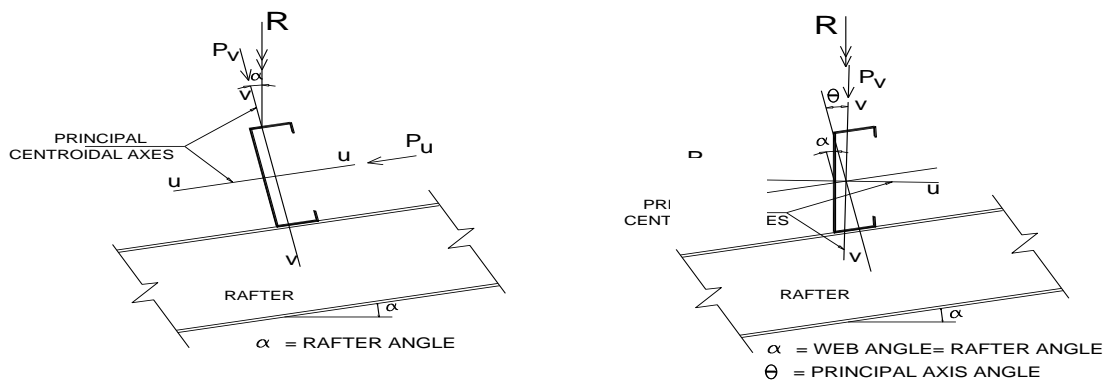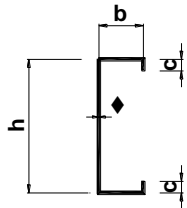


**a) Purlins having Perpendicular Web**     **b) Purlins having Inclined Web**

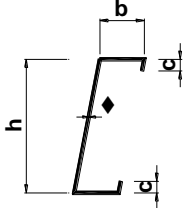**Fig. 2: Layout of Purlins Having Perpendicular Web and Inclined Web**

All 20 sections have been studied under the effect of pure bending assuming that the maximum stress at the top and bottom of the section is 2400 kg/cm². The purlins studied have simple span of 6 meters and carry sandwich panels load of 15 kg per square meter plus the own weight of the purlin and a live load of 50 kg per square meter. The spacing between purlins is taken 1.20 m. Finite element analysis is carried out to study the behavior of the above mentioned C-Purlins.

**Table 1: Dimensions of the Selected Cold Formed C-purlins**

| NOTATION | h (mm) | b (mm) | c (mm) | t (mm) |
|----------|--------|--------|--------|--------|
| 200C15 | 200 | 60 | 20 | 1.5 |
| 200C20 | 200 | 60 | 20 | 2 |
| 200C25 | 200 | 60 | 20 | 2.5 |
| 200C30 | 200 | 60 | 20 | 3 |

**C-Purlins with Perpendicular Web**     **C-Purlins with Inclined Web**

Purlins Type:(3C-O, 6C-O, 9C-O AND 11C-O)

a- (Load Parallel to Web)

Purlin Type:(3C)

b- (Load Inclination Angle=$3°$)

Purlin Type:(6C)

c- (Load Inclination Angle=$6°$)

Purlin Type:(9C)

d- (Load Inclination Angle=$9°$)
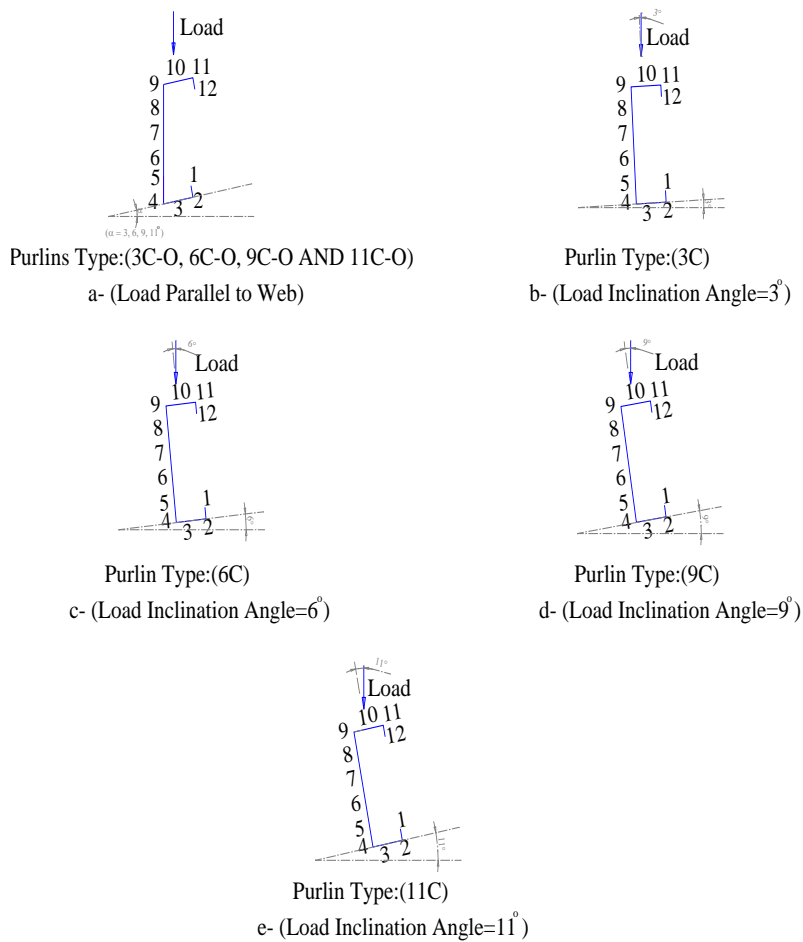
Purlin Type:(11C)

e- (Load Inclination Angle=$11°$)

**Fig. 3: Setup of Purlins and Notations**

### Determination of the Principal Axes

Table 2 shows the moments of inertia of the sections analyzed about the principal centroidal axes at different web slopes and the angle of rotation ($\theta$) with vertical line.

**Table 2: Moments of Inertia about the Principal Centroidal axes at Different Web Angles**

| Angle | 0 | | 3° | | 6° | | 9° | | 11° | |
|---|---|---|---|---|---|---|---|---|---|---|
| | $I_u$ | $I_v$ | $I_u$ | $I_v$ | $I_u$ | $I_v$ | $I_u$ | $I_v$ | $I_u$ | $I_v$ |
| **200C15** | 350.4 | 30.1 | 351.5 | 30 | 355 | 29.8 | 360.8 | 29.6 | 358.5 | 29.1 |
| **200C20** | 467.2 | 40.1 | 468.7 | 40 | 473.3 | 39.8 | 481.1 | 39.4 | 478 | 38.8 |
| **200C25** | 583.9 | 50.1 | 585.9 | 50 | 591.7 | 49.7 | 601.3 | 49.3 | 597.5 | 48.5 |
| **200C30** | 700.7 | 60.2 | 703.1 | 60 | 710 | 59.7 | 721.6 | 59.2 | 717 | 58.2 |

\* All values of $I_u$ and $I_v$ are in cm$^4$

## FINITE ELEMENT ANALYSIS

Finite element analysis is carried out using ANSYS software. The solid 8 node plane stress element is used to analyze the steel C-shaped purlins. With a plane stress element it is assumed that there are no stresses in the thickness direction of the purlins.

The model of the C-shaped purlins are divided to 11 elements along the cross section and 30 elements along the length of the beam as shown in Fig. 4

It is assumed that the structure is a simply supported beam of span 6m and made of steel with modulus of elasticity E=2100 t/cm$^2$ . The grade of steel used is grade 37 with a yield stress $F_Y$ = 2.4 t/cm$^2$ and ultimate strength $F_u$ = 3.60 t/cm$^2$. For all sections; the loads are applied on the top flange of the C-Sections.
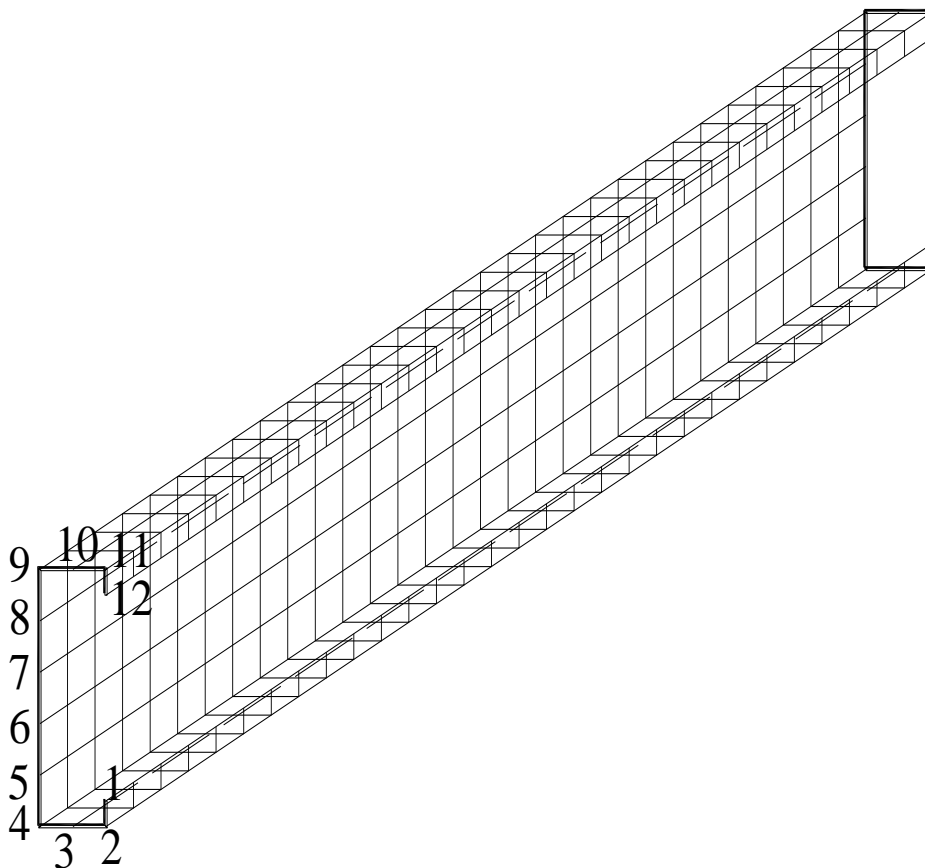


**Fig. 4: Finite Element Model of C-Purlins**

## RESULTS AND DISCUSSIONS

Figure 5 shows the deformed shapes of C-purlins cross sections. Figure 5a shows the deformed shapes of the C-purlins at mid spans and at quadrant point of the span for the case of parallel load to the web i.e. the case of inclined web samples 3C-O, 6C-O, 9C-O and 11C-O. It has to be noted that for all the mentioned samples; the deformed shapes are identical since the load is parallel to the web.

Figures 5b, 5c. 5d, 5e show the deformed shapes of the C-purlins at mid span and at quarter points (samples 3C, 6C, 9C and 11C) respectively for load making angles equal 3, 6, 9 and 11 degrees respectively.

From Figure 5 it has to be noted that the sections are subjected to global buckling mode which involve flexure and rotation of the entire cross section.
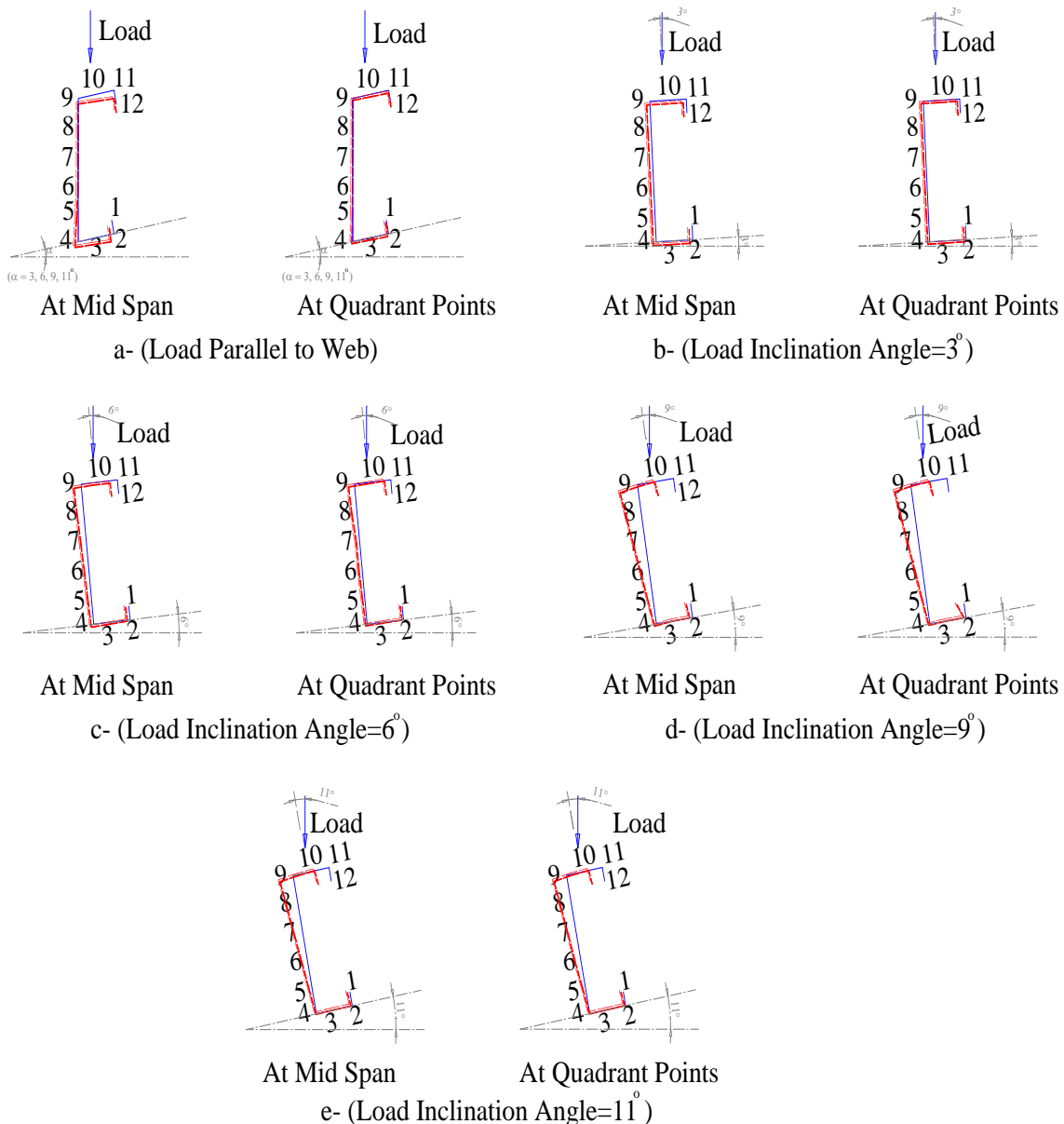


Fig. 5: Deformed Shapes of C-Purlins at Mid Spans and Quarter Points

Figures 6 and 7, show two buckling modes that result from the analysis of the C-purlins. The figures also emphasized that the sections are subjected to global buckling modes.
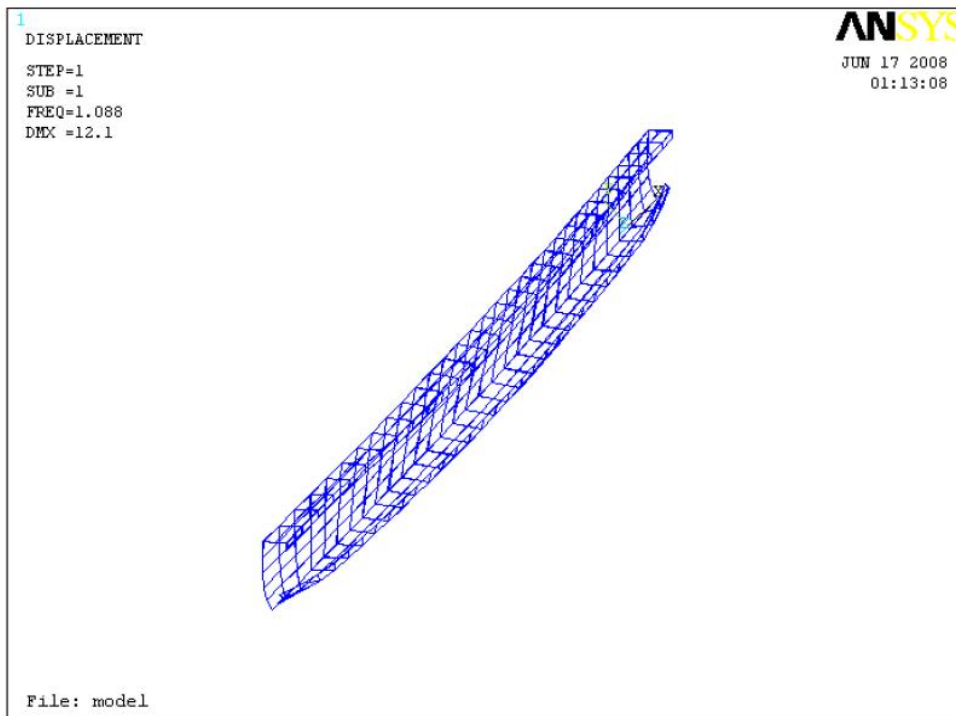
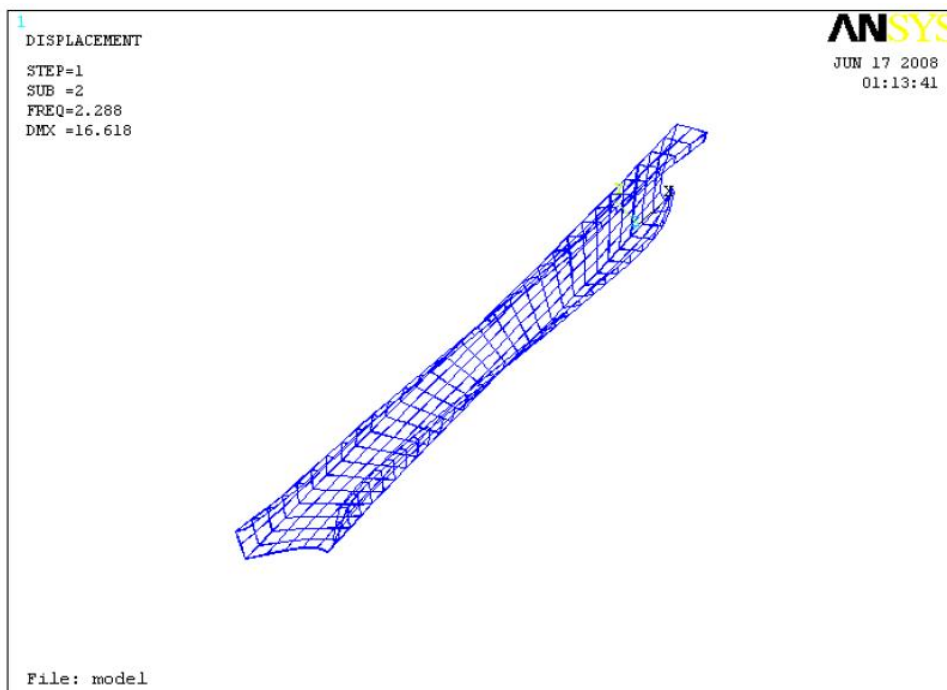**Fig. 6: First Buckling Mode of C-Purlin**



**Fig. 7: Second Buckling Mode of C-Purlin**

Table 3 shows the failure loads of the studied sections and the percentage of reduction in capacities compared to the corresponding case of the load acting parallel to the web (angle = 0). From Table 3 it has to be noted that the failure load of the C-purlin thickness 1.5 mm for the

case of load acting parallel to the web = 0.74 ton and = 0.29 ton for the case of load acting with an angle 11 degrees with the web. In other words a reduction in the load carrying capacity of the C-purlin of 61% is observed.

Similarly, the failure load of the C-purlin thickness 2 mm for the case of load acting parallel to the web = 1.05 ton and = 0.48 ton for the case of load acting with an angle 11 degrees with the web, which means a reduction in the load carrying capacity of the C-purlin of 55% is observed.

The failure load of the C-purlin thickness 2.5 mm for the case of load acting parallel to the web = 1.16 ton and = 0.71 ton for the case of load acting with an angle 11 degrees with the web, which means a reduction in the load carrying capacity of the C-purlin of 39% is observed.

The failure load of the C-purlin thickness 3 mm for the case of load acting parallel to the web = 1.68 ton and = 0.99 ton for the case of load acting with an angle 11 degrees with the web, which means a reduction in the load carrying capacity of the C-purlin of 41% is observed.

Figure 8 shows the plotting of the above results.

**Table 3: Capacity Reduction of C-Purlins at Different Web Inclination Angles**

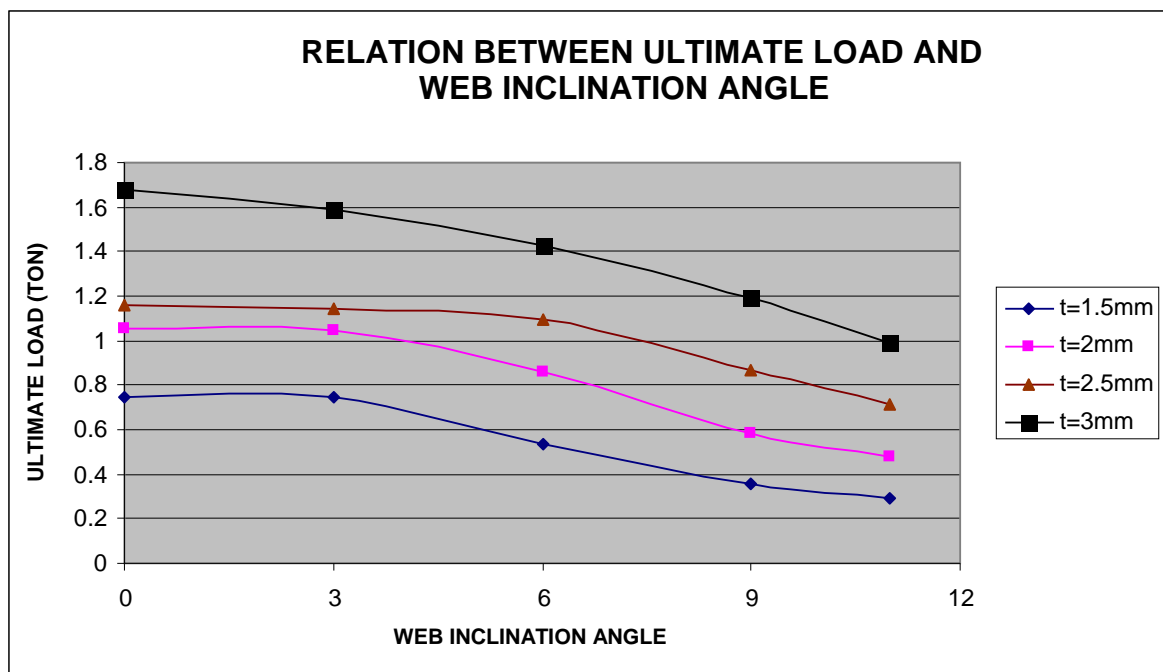| Web Inclination | T=1.5 mm | | T=2 mm | | T=2.5 mm | | T=3 mm | |
|---|---|---|---|---|---|---|---|---|
| | P(Ult.) | % Reduction | P(Ult.) | % Reduction | P(Ult.) | % Reduction | P(Ult.) | % Reduction |
| 0 | 0.74 | 0% | 1.05 | 0% | 1.16 | 0% | 1.68 | 0% |
| 3 | 0.74 | 0% | 1.05 | 0% | 1.14 | 2% | 1.59 | 5% |
| 6 | 0.53 | 28% | 0.86 | 18% | 1.09 | 6% | 1.43 | 15% |
| 9 | 0.36 | 52% | 0.58 | 44% | 0.87 | 25% | 1.19 | 29% |
| 11 | 0.29 | 61% | 0.48 | 55% | 0.71 | 39% | 0.99 | 41% |



**Fig. 8: Relation between Ultimate Load and the Web Inclination Angle of C-Purlin**

## CONCLUSIONS AND RECOMMENDATIONS

The finite element analysis to study the behavior of C-purlins having inclined webs under loads parallel to their webs is made and compared with that for C-purlins having perpendicular webs subjected to loads not parallel to the web. From author's previous research [1], it has been proved that the lateral moment of inertia capacities of the C-purlins having inclined webs are lower than the corresponding values for the C-purlins having perpendicular webs by not more than 3.2%.

Also, the torsional capacities of the C-purlins having inclined webs are almost the same as those for C-purlins having perpendicular webs.

The use of C-purlins having inclined web in conformance with the rafter inclination angle is greatly affecting the design of purlins. For the case of C-purlins having thickness of 1.5 mm and the web inclination angle = 11 degrees, the ultimate load capacity of the C-purlins having perpendicular web is less than that of the corresponding purlin with inclined web by 61%. For the case of C-purlins having thickness of 2 mm and the web inclination angle = 11 degrees, the ultimate load capacity of the C- purlins having perpendicular web is less than that of the corresponding purlins with inclined web by 55%. For the case of C-purlins having thickness of 2.5 mm and the web inclination angle = 11 degrees, the ultimate load capacity of the C-purlins having perpendicular web is less than that of the corresponding Purlin with inclined web by 39%.

For the case of C-purlins having thickness of 3 mm and the web inclination angle = 11 degrees, the ultimate load capacity of the C-purlins having perpendicular web is less than that of the corresponding purlin with inclined web by 41%.

The author recommends the use of C-purlins with inclined webs provided that the web inclination angle is the same as the rafter inclination angle. This will lead to considerable saving in weight of purlins.

## REFERENCES

1.  Fadel, A. M., "Effect of Web Inclination on the Behavior of Cold Formed Steel C-Purlins", HBRC Journal, Vol. 1, No. 2, July 2005, PP 81 – 91
2.  Wei Lu, "Optimum Design of Cold-Formed Steel Purlins Using Genetic Algorithms", Ph.D., 2003, Helsinki University of Technology, Department of Civil and Environmental Engineering, Laboratory of Steel Structures.
3.  Cheng Yu and Benjamin W. Schafer, "Local Buckling Tests on Cold-Formed Steel Beams", Journal of Structural Engineering, ASCE, December 2003, PP 1596 – 1606.
4.  Fadel, A. M., El-Saadawy M. M., "Effect of Web Inclination on the Behavior of Cold Formed Steel Z-Purlins", Journal of Engineering and Applied Science, Cairo University, Vol. 52-Number 5, October 2005, PP 905 – 920

# A COMPUTATIONAL MODELING FOR A VERTICAL PILE IN SOIL

**\* Dr. Yasser A. Rihan and Dr. Ibrahim S. Ibrahim**

*Hot Lab. Center, P. Code 13759, Atomic Energy Authority, Cairo – Egypt*
*Email: yarihan159@yahoo.com*

## ABSTRACT

This study presents a computational investigation for the vertical pile in soil under axisymmetric loading conditions. A numerical pile load-testing program was carried out using finite element technique. Linear strain quadrilateral elements were employed to model soil and pile. The numerical rnodel was validated against experimental load tests data for different authors. The numerical model was then used to analyze stresses influencing the pile behavior in soil and to establish the pile failure mechanism. The factors affecting the failure mechanism such as the pile depth and diameter, shaft relative roughness and angle of shearing resistance were studied. The stresses and coefficient of earth pressure acting on the pile shaft were reported. The theoretical model was developed to predict the ultimate bearing capacity of a pile in soil. An approximate method to predict the coefficient of earth pressure acting on the pile shaft was developed and used extensively in the theoretical model. The results concur with the recent research conclusions, which indicate that the average skin resistance tends to increase with depth. A design procedure is proposed and verified against field test results, good agreement was achieved. The results of the present investigation the basis for a design procedure to estimate the ultimate bearing capacity of single pile in sand.

**Keywords:** Axisymmetric loading, Modeling, Numerical analysis, Pile, Soil, Vertical.

## INTRODUCTION

Several techniques have been proposed to model the finite soil. Winkler's model that has been developed in the work of Lee [1] has the advantage of its simplicity and relative ease of implementation on the computer, but it has the difficulty of choosing the elastic moduli of the springs for a given combination of pile size and soil type. Burmister [2] was the first to use integral transforms to obtain semi-analytical solutions for the displacements and stresses in a heterogeneous medium without taking foundations into account. Others working along the same lines are (Gibson, 1967; Ueshita and Meyerhof, 1968) [3, 4].

The finite layer method can be used to reduce the three dimensional problem to one involving only two dimensions by combining the Fourier transform technique with the finite element method. Piles are introduced into the system by introducing equilibrium and compatibility conditions at the interfaces between the two media. The finite element method is the most versatile and powerful tool available to solve numerical problems in mechanics. However, when it is applied to infinite domains, such as the soil, the preparation of data is complicated and requirements for data storage and processor time are heavy, especially when the problem is formulated with three dimensional elements [5].

A number of researchers have employed Mindlin's solution [6] for the semi-infinite continuum and the simplified Steinbrenner [7] model for finite media. However, the use of Mindlin's fundamental solution in a boundary element method application is only valid for a single homogeneous medium. It is not possible to introduce other media with distinct physical properties because the boundary conditions imposed a priori by the formulation of the solution. The numerical modeling techniques based on the finite element or finite difference methods are

becoming increasingly used in geotechnical engineering. Pile behavior has been widely investigated using numerical analysis, and various modeling techniques of the pile-soil interface have been reported. Fellenius et al. [8] performed two dimensional finite element analysis for piles subjected to bidirectional loading using the thin layer element, and Bui et al. [9] conducted two dimensional finite difference analysis using the strength reduction factor. Kong et al. [10] performed both two dimensional finite element analysis and the Rocket program [11].

Based on the method described by Zienkiewicz [12], a variety of finite element computer programs have been developed with varieties of facilities to suit different needs. Analysis for piles using the finite element method have been used by numerous researchers [13- 18]. The numerical model developed in this study was carried out using finite element method. In this paper, a numerical model was introduced to examine the effect of various factors influencing the bearing capacity of a pile driven in sand and the coefficient of earth pressure acting on the pile shaft.

## NUMERICAL PROCEDURE

The numerical model developed in the present study was carried out using the finite element code CRISP94 [19]. Fig. 1 shows the typical mesh used in this work and the general configuration of the interface surfaces. In this analysis, a circular pile was adopted in two-dimensional axisymmetric conditions. The overall dimensions of the model boundaries comprise a width of 25 times the pile diameter (d) from the pile center and a height of pile length (L) plus a further 1.5 L below pile-toe level. These dimensions were considered adequate to eliminate the influence of boundary effects on the pile performance [20]. The pile and soil are modeled with finite elements, which allow for rigorous treatment of the soil-structure interaction. Both the soil and pile are represented by eight-node, second-order quadratic elements. A relatively fine mesh was used near the pile-soil interface and the pile-toe, and became coarser farther from the pile. An isotropic elastic model was used for the pile and a Mohr-Coulomb model was used for the soil. Table 1 shows the elastic parameters required by the program to model the pile and soil materials.
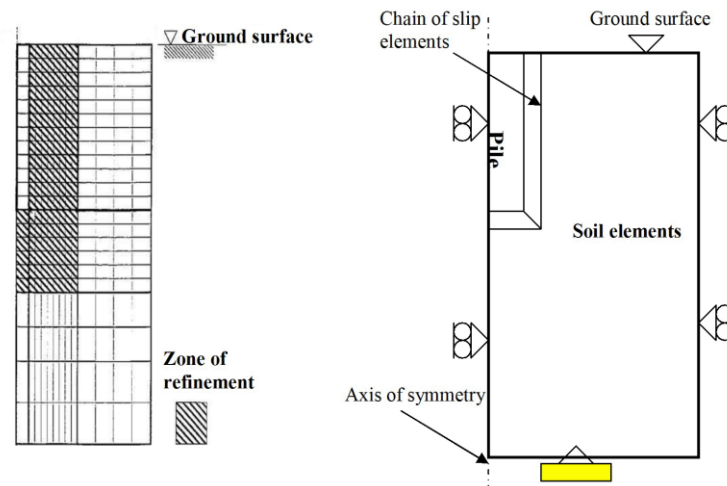


**Fig. 1: Typical Idealized Two-Dimensional Axi-Symmetric Model for Finite Element Analysis**

**Table 1: Elastic Parameters for Steel Pile and Sand Soil**

| Parameter | Pile | Soil |
|---|---|---|
| Young's modulus | $2 \times 10^8$ kN/m$^2$ | $14 \times 10^6$ kN/m$^2$ |
| Poisson's ratio | 0.3 | 0.3 |
| Shear modulus | $77 \times 10^6$ kN/m$^2$ | - |
| Bulk unit weight | 78.4 kN/m$^3$ | 9.82 kN/m$^3$ |

The skin friction can be calculated using Sarma's method (1979), which divided the soil mass enclosed in a plane slip surface into a number of slices. The total skin friction, $Q_s$, can be computed as:

$$Q_s = \left( R_g \cos(90 - \phi - \beta) - W_a + \left( \frac{W_g + W - AR_1}{A - \tan \delta} \right) \tan \delta \right) \left( \frac{2\pi}{\xi} \right)$$  (1)

where $R_g$ is the ground reaction on the surface and can be expressed as:

$$R_g = 0.25 \gamma H^2 K_0 R \xi$$  (2)

$\gamma$ = unit weight of sand.
$H$ = vertical height of mobilized skin resistance zone.
$\Phi$ = angle of shearing resistance of sand.
$K_0 = 1 - \sin\Phi$.
$R$ = radius of influence in meter.
$\xi$ = central angle of rotation.
$\beta$ = inclination angle of outer side of mobilized skin resistance zone.
$W$ = weight of slice.
$W_g$ = vertical reaction acting above slice.

$$A = \left( \frac{\sin \alpha - \tan \chi . \sin(90 - \alpha)}{\cos \alpha - \tan \chi - \cos(90 - \alpha)} \right)$$  (3)

$\chi$ = mobilized angle of shearing resistance.

The earth pressure force, $E_e$, acting on the vertical height ($L_1 + L_2$) is given by:

$$E_e = 0.5 K_s \gamma [(2d - L_1 - L_2)] \xi$$  (4)

where,
$K_s$ = coefficient of earth pressure acting on the pile shaft.

The point resistance, $Q_p$, can be expressed as:

$$Q_p = \left( \frac{2\pi}{\xi} \right) (F_n \cos\psi + F_t \sin \psi) - W_c$$  (5)

where,
$W_c$ = weight of the cone of sand beneath the pile tip.
$\psi$ = base angle, $\tan^{-1} (L/d)$.
$F_n$ and $F_t$ is the normal and tangential forces, the calculation of these forces starts with analysis of external forces acting on the control volume.
The bearing capacity factor, the non-dimensional form of bearing capacity, can be computed using the following equation:

$$N_q = Q_p / (\gamma D A_p)$$  (6)

where,
$D$ = embedded depth of the pile.

A slip element was employed to simulate the interaction at soil-pile interface. The slip element used in the analysis was similar to the one proposed by Desai [21]. It was treated as a one dimensional element with six distinct nodes. This element was also formulated to behave as a linear elastic-perfectly plastic.
The nodes belonging to the periphery of the cylindrical mesh are considered to be fixed against displacement in both horizontal directions and the nodes constituting the bottom of the mesh are fixed against displacement in both horizontal and vertical directions.

## RESULTS AND DISCUSSION

The results from Ottaviani [22] will be compared with those obtained by the present method at the same conditions to validate this model, evaluating in particular the effect of varying the depth between the rigid floor of the soil and the end of the pile. Fig. 2 shows the values of maximum shear stress in soil adjacent to the pile at points down the shaft. There is a good agreement between the present results and Ottaviani results.
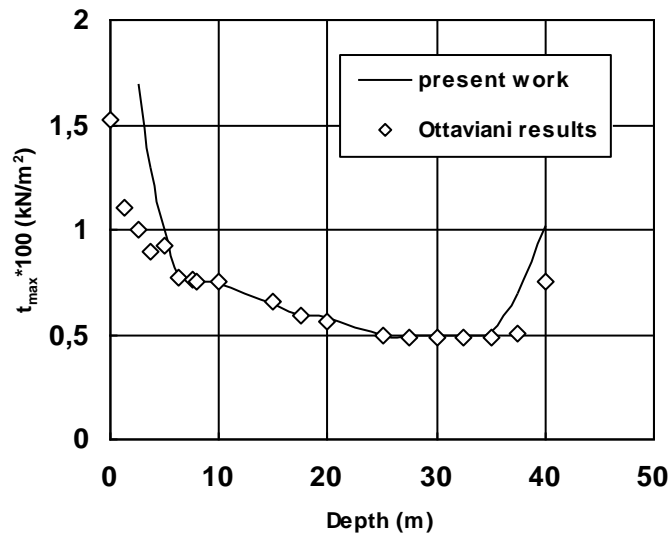


**Fig. 2: Maximum Shear Stress in Soil Adjacent to Pile *vs.* Depth**

Fig. 3 predicts the bearing capacity factor as a function of pile depth at different pile diameters, d, and different angles of shearing resistance of sand, Φ, in degrees. The critical depth increased with pile width and depth as shown in the figure. The curve also indicate the increase of bearing capacity due to the increase of shearing resistance angles. The unit skin friction versus pile depth for various pile diameters are shown in Fig. 4. The skin friction is increasing with increasing depth. The critical depth depends on the pile depth, diameter and angle of shearing resistance. The critical depth decreases with pile diameter.
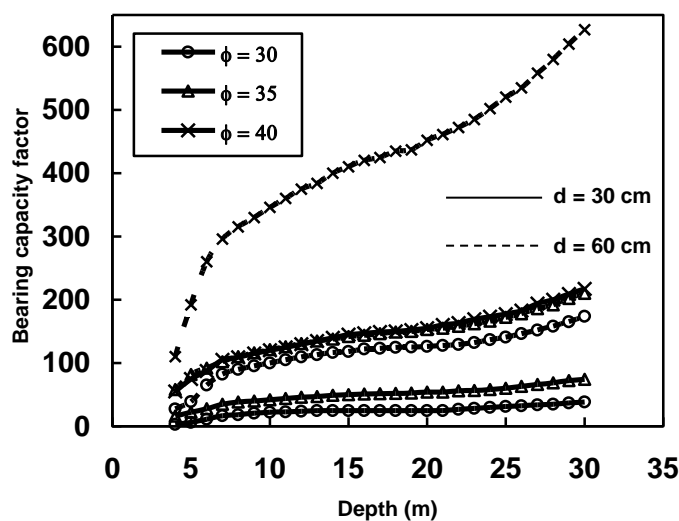


**Fig. 3: Bearing Capacity Factor *vs.* Pile Depth at Different Angles of Shearing Resistance**
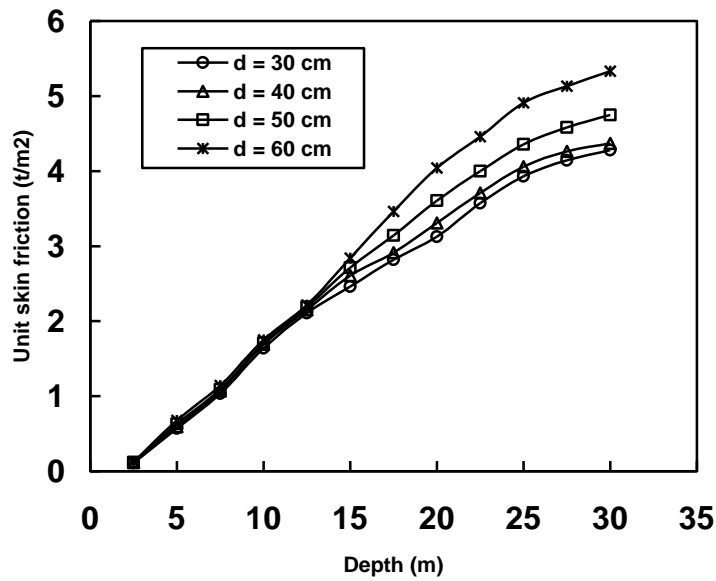
Fig. 4: Unit Skin Friction *vs.* Pile Depth, $\phi = 35°$

Coefficient of earth pressure is considered as a major factor affecting the value of skin resistance. The distribution of the coefficient of earth pressure is not constant over the shaft and it varies with depth. Fig. 5 shows that the coefficient of earth pressure decreases with the increase of angle of shearing resistance and reaches higher values with smaller pile depths. The effect of the shaft roughness, $\rho$, on the coefficient of earth pressure is shown in Fig. 6. The figure indicates that with increasing the shaft roughness, the coefficient of earth pressure increases. Fig. 7 indicates the increase of ultimate load due to the increase of shearing resistance angles. The results obtained show good agreement with those found in the literature.
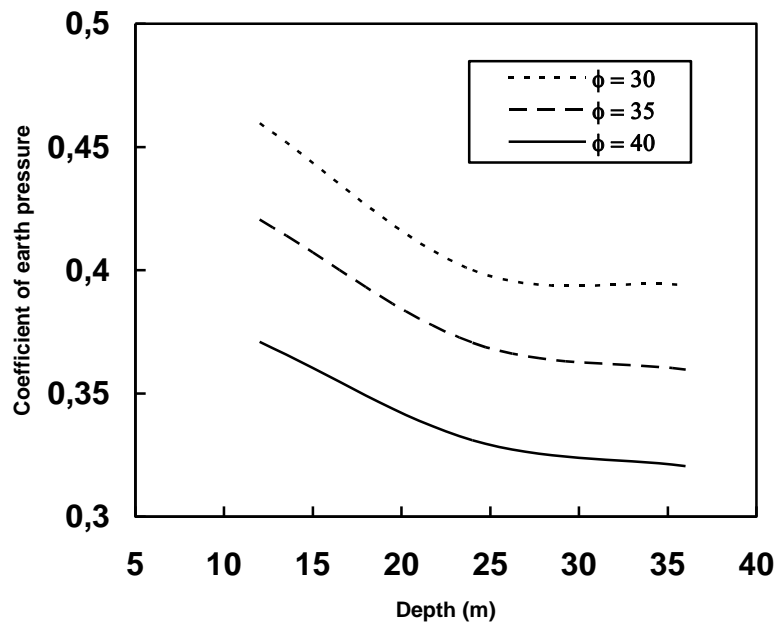


Fig. 5: Coefficient of Earth Pressure *vs.* Depth at Different Angles of Shearing Resistance, d = 40 cm
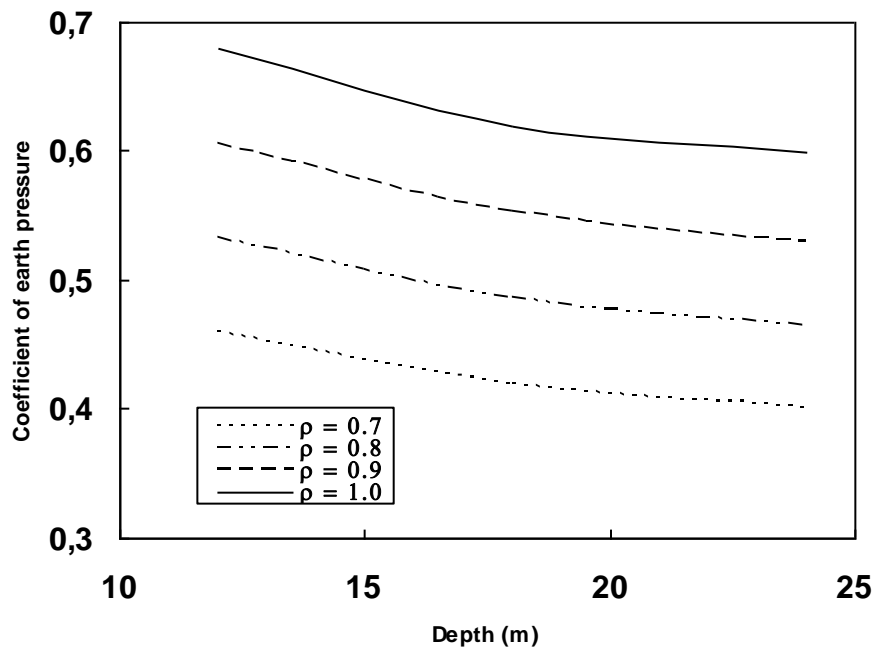
**Fig. 6: Coefficient of Earth Pressure *vs.* Depth at Different Shaft Roughness, $\phi = 35°$**
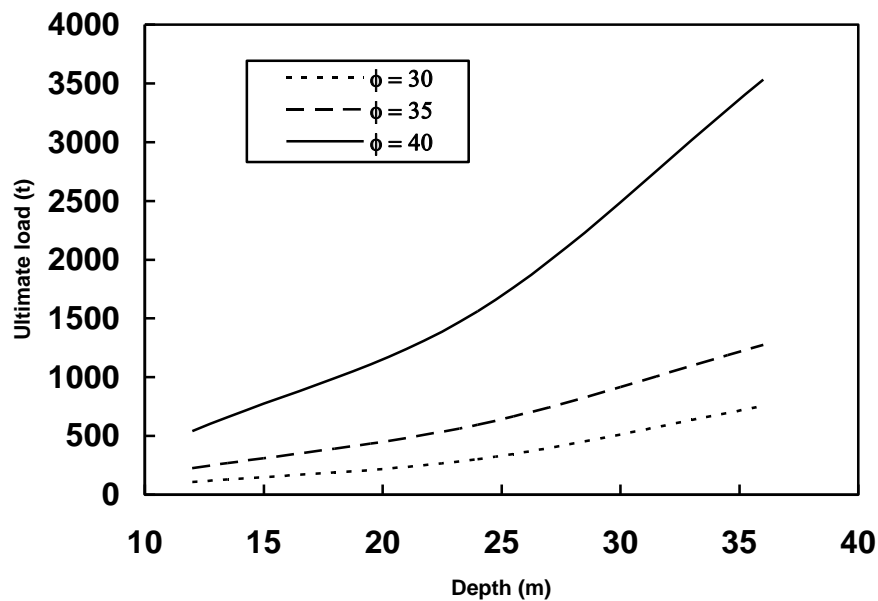


**Fig. 7: Ultimate Load at Different Angles of Shearing Resistance, d = 35 cm**

## CONCLUSIONS

A computer program facilitating a new theoretical model was developed and used to investigate the vertical pile in soil under axisymmetric loading conditions. A numerical pile load-testing program was carried out using finite element technique. The numerical rnodel was validated against experimental load tests data. The numerical model was then used to analyze stresses

influencing the pile behavior in soil and to establish the pile failure mechanism. The factors affecting the failure mechanism such as the pile depth and diameter, shaft relative roughness and angle of shearing resistance were studied. The distribution of the coefficient of earth pressure is not constant over the shaft and it varies with depth. The coefficient of earth pressure acting on the pile shaft were reported. The model was developed to predict the ultimate bearing capacity of a pile in sand employing the Sarma method of slices and limit equilibrium technique. The results concur with the recent research conclusions, which indicate that the average skin resistance tends to increase with depth. The results are the basis for a design procedure to estimate the ultimate bearing capacity of a single pile in sand.

## REFERENCES

1. Lee, C. (1993), "Pile group settlement analysis by hybrid layer approach", J. Geotech. Eng., Vol. 18, pp. 41-45.
2. Burmister, D. (1945), "The general theory of stresses and displacements in layered systems I", J. Appl. Phys., Vol. 16, pp. 89-96.
3. Gibson, R.E. (1967), "Some results concerning displacements and stresses in a nonhomogeneous elastic half-space", Géotechnique, Vol. 17, pp. 58-64.
4. Ueshita, K., and Meyerhof, G. (1968), "Surface displacement of an elastic layer under uniformly distributed loads", Highway Res. Board Record, Vol. 228, pp. 1-10.
5. Valério, S., and João, B. (2007), "Static analysis of soil/pile interaction in layered soil by BEM/BEM coupling", Advances in Engineering Software, Vol. 38, pp. 835-845.
6. Mindlin, R. (1936), "Force at a point in the interior of a semi-infinite solid", J. Phys., Vol. 7, pp. 195-202.
7. Poulos, H.G. (1967), "Stresses and displacements in an elastic layer underlain by rough rigid base", Géotechnique, Vol. 17, pp. 378-410.
8. Fellenius, B., Altaee, A., Kulesza, R., and Hayes, J. (1999), "O-cell testing and FE analysis of 28-m-deep barrette in Manila, Philippines", J. Geotech. Geoenv. Eng., Vol. 125, pp. 566-575.
9. Bui, T., Li, Y., Tan, S., and Leung, C. (2005), "Back analysis of O-cell pile load test using FEM", In: Proceedings of the sixteenth international conference of soil mechanics and geotechnical engineering, Osaka, pp. 1959-1962.
10. Kong, K.H., Kodikara, J., and Haque, A. (2006), "Numerical modelling of the side resistance development of piles in mudstone with direct use of sidewall roughness", Int. J. Rock Mech. Min. Sci., Vol. 43, pp. 987-995.
11. Seidel, J.P., Collingwood, B. (2001), "A new socket roughness factor for prediction of rock socket shaft resistance", Can. Geotech. J., Vol. 38, pp. 138-153.
12. Zienkiewicz, O.C. (1977), "The finite element method", McGraw-Hill, New York.
13. Simonini, P. (1994), "A finite element analysis of the tip bearing of bored piles in sand", Proc. of 8th Int. Conf. on Computer Methods and advances in Geomechanics, Balkema, Roterdam, Vol. 3, pp. 2311-2316.
14. Zaman, M., Najjar, Y., and Muqtadir, A. (1993), "Effects of cap thickness and pile inclination on the response of a pile group foundation by three-dimensional nonlinear finite element analysis", Computers and Geotechnics, Vol. 15, pp. 65-86.
15. Chen, L., and Polous, H. (1993), "Analysis of pile-soil interaction under lateral loading using infinite and finite elements", Computers and Geotechnics, Vol. 15, pp. 189-220.
16. Sadecka, L.A. (2000), "A finite/infinite element analysis of thick plate on a layered foundation", Comp. Struct., Vol. 76, pp. 603-610.
17. Hossien, T., and Kazuo, K. (2007), "Numerical analysis of nonlinear soil-pile group interaction under laterals loads", Soil Dynamics and Earthquake Engineering, Vol. 27, pp. 463-474.
18. Cheng, C.Y., Dasari, G., Chow, Y., and Leung, C. (2007), "Finite element analysis of tunnel-soil-pile interaction using displacement controlled model", Tunnelling and Underground Space Technology, Vol. 22, pp. 450-466. O'Neill, M.W., Townsend, F., Hanssan, K.M., Buller, A., and Chan, P. (1996). "Load transfer for drilled shafts in intermediate geomaterials." US Department of Transportation, Washington.
19. Britto, A.M. (1988), "CRISP user's and programmer's guide.", CUED.

20. O'Neill, M.W., Townsend, F., Hanssan, K.M., Buller, A., and Chan, P. (1996), "Load transfer for drilled shafts in intermediate geomaterials", US Department of Transportation, Washington.

21. Desai, C.S. (1974), "Finite element analysis of the Colombia lock pile foundation system", US Army Engineer waterways Experiment Station, Technical Report, S-74-6.

22. Ottaviani, M. (1975), "Three-dimensional finite element analysis of vertically loaded pile groups", Géotechnique, 25(2), pp. 159-174.

# AN OVERVIEW OF CHALLENGES AND SOLUTIONS TOWARD IMPROVED, LOW COST BUILDING SYSTEMS IN THE US

**\* Fernando P. Ruiz**

*Owner of Brighton Homes and Builder of PATH Concept Home in Lincoln (see footnote), Nebraska, USA, Tel (402)434-2456, E-mail: fpages@brightonconstruction.biz*

**James D. Goedert, Ph.D., P.E.**

*Director Construction Engineering and Management, University of Nebraska, USA, 68182, Tel (402)554-3281, E-mail: jgoedert@mail.unomaha.edu*

## ABSTRACT

The United States faces a housing affordability crises, especially among minority and disadvantaged populations in both rural and inner city, urban locations. The solutions to this challenge have come mainly through government subvention programs. However, dwindling Federal and State monetary resources cannot meet the needs of a burgeoning population requiring safe, energy-efficient, affordable housing. The United States department of Housing and Urban Development (HUD) recognized the need to address these issues from a broad, market-driven approach that relies on improved construction methods and materials, rather than simply underwriting inefficient and technologically outdated building practices. The Partnership for Advancing Technology in Housing (PATH) "is dedicated to accelerating the development and use of technologies that radically improve the quality, durability, energy efficiency, environmental performance, and affordability of America's housing." HUD's Office of Policy Development and Research manages and coordinates PATH activities. This government program in partnership with private industry is currently building a Concept House in Omaha, Nebraska, modeling the most advanced technological building methods currently in practice in the United States for residential construction. This house integrates compatible advanced building systems as an educational tool for both the housing industry and consumers of US housing. This paper will present a survey of affordable housing technologies and concepts.

**Keywords:** Residential, Affordable, Insulated Concrete Forms, Durable, Panelized.

## INTRODUCTION

This paper describes some features of a Concept House that are relevant to the international audience because they highlight construction concepts as well as specific building techniques. The United States (U.S.) Department of Housing and Urban Development's (HUD) Partnership for Advancing Technology in Housing (PATH) in partnership with private industry is building the first concept house that integrates advanced building systems.

The U.S. Department of Housing and Urban Development's (HUD) mission is to increase homeownership, support community development and increase access to affordable housing. The Policy Development and Research (PD&R) Division of HUD is responsible for conducting research on important housing issues. Within PD&R is the PATH. PATH is "dedicated to accelerating the development and use of technologies that radically improve the quality, durability, energy efficiency, environmental performance, and affordability of America's housing" [1]. PATH has authored a library of research papers that have helped architectural engineers and manufacturers to develop more effective construction methods and materials. Examples include studies and testing on cross-linked polyethylene (PEX) piping that lead to its broad

acceptance throughout the United States at a time when copper prices made traditional water piping prohibitive. Other examples include research in concrete and wood framing techniques that provide cost savings and reduce the consumption of raw materials.

Residential construction in the United States operates, largely, within small, local code jurisdictions and without formal training. The lack of uniformity in construction regulations and a predominantly uneducated workforce makes it difficult to introduce new building technologies. The bureaucracies of municipal building departments tend to resist new construction methods. The artisan approach to training construction workers results in a labor pool that has memorized choreography of work habits. Little is learned regarding the engineering behind construction methods. Resistance to innovation is endemic to the construction industry in the Untied States.

The goal of the PATH Advisory Group is to designing and building one Concept House each year that would illustrate the best practices in residential construction and introduce a few emerging technologies. This is intended to speed the adaptation of new construction methods and to generate consumer interest in the advancing technology of homebuilding. This paper describes a few of the salient features in PATH's first Concept House. The home includes a number of innovative features that provide quality and affordability through improvements in production methods. The house is currently under construction in Omaha, Nebraska. This paper will first review the systems approach to design, then describe some energy efficiency features, and then discuss the panelized construction systems, insulated concrete foundation, and efficient mechanical systems.

## SYSTEMS APPROACH

Technologies that are relatively new to the United States were introduced in the Concept House such as grey water recycling and movable interior partition walls. However, the most significant innovation came through a "systems" approach to design. This means every element in the house, from the foundation through the roof was engineered to work in coordination. The objectives of every element in the system were energy efficiency, durability, flexibility and speed of construction.

 Energy efficiency came with the best weatherproof barriers available, a mechanically engineered grey water reclamation system, a water-saving tank-less water heater, expanding foam insulation derived from soybeans, and an engineered heating and air-conditioning system. Durability was the focus of the exterior. It includes a 150-year standing seam steel roof. It also includes a panelized, insulated concrete form (ICF) used for the basement that installed in one day. A new attic wrap system assures ventilation for the sheathing and a weather-tight envelope over the attic.

 Flexibility means a house that adapts to changing lifestyles. One example is movable partition walls. Wireless switches allow a homeowner the flexibility to reconfigure the floor plan to adapt to a range of lifestyles and family configurations.

Factory built components were assembled on the construction site increasing the speed of construction. The most dramatic improvements in construction time came with the panelized insulated concrete form (ICF) basement. These were manufactured in Minneapolis, Minnesota and trucked to the construction site in Nebraska. Within seven hours of the truck's arrival, workmen had finished assembling and pouring concrete into the insulated forms. Panelized floor, wall, and roof wood framing permitted similar improvements in the construction productivity of all structural components. Even millwork for windows and doors were fabricated in a factory setting and simply installed in place. With precise panelized framing and a systems approach to efficiency and durability, the home was quickly dry and under cover.

## ENERGY EFFICIENCY

The double-hung windows were installed perfectly into the rough framing openings, providing further evidence of the precisely constructed shell.  These Energy Star windows are efficient and durable to keep the harsh Nebraska weather out, thanks to a low U factor (0.35) and a low-emissivity film with UV protection to reduce heat gain and fading.

The weather barrier system features an innovative weather resistant barrier. It has specially designed vertical grooves to channel water to the outside while still allowing moisture vapor to pass through. The weather resistant system for the roof and attic includes a "cool" metal roof. It

gives long-term durability and maximum energy performance through its pre-painted solar reflective color that reduces heat and its special zinc/tin alloy that provides enhanced corrosion resistance (see Figure 1).



**Fig. 1: Energy Efficient Exterior**

The attic wrap is a breathable membrane installed just under the top chord of the trusses. It helps to create an airtight seal. Its metalized surface reflects heat while allowing moisture vapor to escape.  This reduces air leakage and energy loss through roof while allowing the attic to dry out.Insulated vinyl siding was installed over the framing and weather resistant barriers, creating an energy efficient shell. Styrofoam backing provides an R-3 insulative value and increases the stiffness and rigidity of the siding. The thermal siding with the drain wrap keeps water out and allows any moisture to easily drain from the assembly. The wood trim was pre-painted and ready to install upon arrival allowing the trim to be installed along with the siding. This feature reduced installation time and rental fees associated with lift equipment as shown in Figure 2.



**Fig. 2: Vinyl Siding**

## PANELIZED CONSTRUCTION SYSTEMS

Panelized construction systems in the United States refers to building components manufactured off site, generally in a factory, and then transported to the point of construction in flat panels ready for assembly. The Concept House used several factory built components, most notably insulated concrete forms (ICF) built in approximately 3.66 meters (12-feet) by approximately 2.44 meters (8 feet) rectangles; factory framed floors brought to the jobsite in approximately 2.44 meters (8 feet) by approximately 7.32 meter (24 feet) sections; walls in 2.44 meters (8 feet) by 3.05 meters (10-feet) sections, and truss roof framing. The benefits of

panelized construction include reliable working conditions in areas of inclement weather, speed of construction and assembly, reliability based on computer driven tools and factory tolerances, and worker safety in erecting fully-built panels rather than building block-by-block in more precarious jobsite conditions.

**Insulated Concrete Foundations**
ICFs are appealing for the increased productivity and high insulation values. The proprietary product design and expensive distribution system coupled with high labor costs have diminished the benefits of a these super-insulated concrete walls in affordable housing. Gajda and VanGeem [4] found that homes built with ICFs had total energy reductions between 8% and 19% below traditional wood framed construction. In addition, the cost savings from reduced system capacity ranged from 16% to 30% below houses meeting the International Energy Conservation Code.  Proponents argue that the benefits of additional structural insulation are often paid back in lower operating costs. Others indicate that reduced operating costs can be achieved through other less costly methods.

ICFs come in three varieties including a flat wall core system illustrated in Figure 3. Other systems include the waffle grid and the screen grid [5]. Nevertheless, when used in a panelized system, the lower onsite labor costs and speed of assembly promise to provide a bright future for ICFs. In regions of the world where facilities exist for designing and building polystyrene blocks and labor is less expensive, ICFs represent a viable alternative to concrete block.
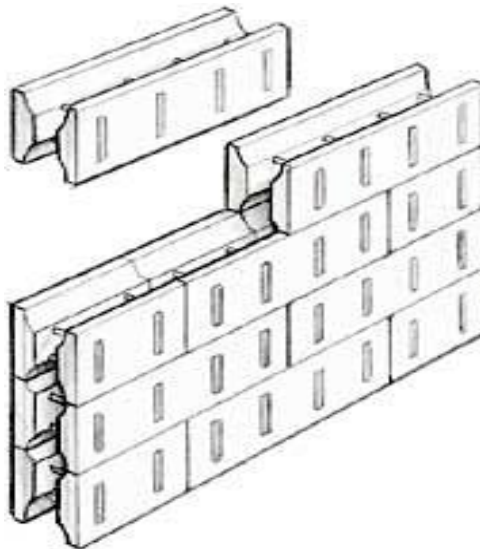


**Fig. 3: Insulated Concrete Form**

On the concept house, instead of stacking standard sized blocks, the manufacturer designed full height wall panels to within half-an-inch of the specified height. They were trucked to the construction site along with an expert installer.

After training a local crew who were inexperienced with the product, the manufacturer delivered the basement walls for a 2,000 square-foot house at 8:00 in the morning. The walls were unloaded and erected by noon, with concrete placement beginning in the early afternoon as shown in Figure 4. The windows were cut into place with no need to strip forms, apply waterproofing, or insulate the basement. The whole process was done in a day. The standard block or aluminum formed basement would have taken approximately two weeks to complete in two separate phases.

**Factory Framing**
Wood framing is of lesser relevance to projects outside North America. However, the Concept House was greatly advanced through the use of component floors and walls. Like the ICF forms, these components are built in a factory using proprietary engineering software and a

**Fig. 4: Concrete Placement in Insulated Concrete Forms.**

computer automated factory equipment. The equipment cuts and marks all framing members. Assembly occurs on steel tables with large banks of nail guns. The panels are lifted onto trucks in reverse order of jobsite assembly, delivered to the construction, and then assembled by semi-skilled labor. Of greatest interest to the international construction community might be the component floor systems, since many countries use wood in the construction of floors and roof structure as shown in Figure 5.



**Fig. 5: Component Floor System**.

Ruiz [8] indicates that panelized systems result in substantial labor savings. The first floor panel required 21.36 man-hours of shop time and 6.25 man-hour of field time. Conventional framing would take approximately 31 man-hours of field time. The second floor panels required 29.64 man-hours of shop time and 7.5 man-hours of field time. Convention framing of the second floor would take approximately 41 man-hours. This is a productivity increase of approximately nine percent.

## MECHANICAL SYSTEMS

The key to balancing durability with energy efficiency in the Concept House's mechanical system was to system engineer the whole rather than separate elements. Durability was provided using low-cost means while achieving longer lifespan in mechanical systems. Cross-linked polyethylene (PEX) has been used in Europe for more than 30 year and more than 10 years in North America. PEX is superior to polybutylene piping systems [3] and does not break

in freezing temperatures or corrode with mineral elements [2]. Energy efficiency was accomplished with tightly sealed duct delivery system for heating and air conditioning that would not waste fuel consumption due to in-line losses and pour, unbalanced distribution of conditioned air.

A tankless water heating system produces hot water on-demand. This device won't waste energy keeping water hot when there is no demand. Even the venting of the system is advanced, relying on special 1-way air valves called Air Admittance Vents (AAVs) to let air into the drain system when needed.  These units perform the same function as a traditional vent stack but eliminate the piping requirements and most of the roof penetrations.

**Engineered Plumbing**

The Concept Home has a state-of-the-art integrated system, featuring an efficient design, water-conserving components, and innovative technologies that show the future in water management.

The Concept House floor plans show a centralized mechanical core with bathrooms and laundry room adjacent to this core. This innovative design strategy reduces the necessity to run pipes, wires and ducts throughout the home.  Material requirements are reduced, along with the number of joints and time required for installation. In the United States, residential plumbing, heating and electrical systems are generally designed on site relying on individual tradesmen to simply figure out what and how to install based on experience. The PATH Concept House employed professional engineers to analyze and design the systems for maximum efficiency.

The PEX tubing was literally pulled from the basement to the upstairs fixtures, saving on installation time. The "home run" lines have no joints and ensure that hot water arrives quickly upon demand. Many of the lines take advantage of 3/8" tubing (instead of ½"). This further reduces line loss while waiting for hot water. The system displayed in Figure 6 allows the builder and homeowner to control each water line independently, meaning that maintenance and remodeling can take place without shutting off water for the entire home.  Installation and updates to the plumbing are further simplified by quick-connect fittings that quick snap connection between the PEX and each fixture.  These innovative components speed installation and make later disconnects easy.



**Fig. 6: PEX Plumbing Manifold**

**Grey Water System**

Grey water systems in the UK usually refers to water recycling from "any water source except those with fecal matter present but is mainly restricted to baths, showers and hand basins" [6]. Following filtration and sterilization, the recycled "grey water" is used for clothes washing, irrigation, and supply water to toilets. The system uses no chemicals to clean the water making it an environmentally benign product. These small scale treatment plants represent a growing trend in water conservation. This particular system represents the first grey water recycling system installed in a major metropolitan area in the United States. Many government agencies are not yet familiar with these systems and substantial hurdles exist for installation.

Issues regarding recycled water are extremely complex when considering large-scale urban environments where the opportunities abound. However, these small scale recycling

technologies so real potential and have become commercially available. Jeffrey, et.al. [7] indicates that "a simple reuse system which takes water from the bath and shower to be used for toilet flushing, average water savings of about 20%." This saving is significant when multiplied by the large number of households in a given municipality.

## CONCLUSIONS

The HUD PATH program is attempting to educate home builders across the United States through the concept home. Innovative technologies are developed and then incorporated into the home. This is followed by a series of promotions including a website with links describing those new technologies. The first concept home built in Omaha, Nebraska incorporates a number of innovative systems. Most of these systems are proven technologies that have not gained wide acceptance. Some systems may be cost prohibitive in a competitive market. Others may have higher initial cost with lower overall life cycle cost. Technologies such as the ICFs are gaining market share. The concept house used the ICF only for the basement. Some builders are using the ICF for the entire structure including affordable home builders. PEX water distribution systems make good economic sense and are allowed by the International building code. This alternative to copper piping is economical in terms of both materials and installation. It is not yet widely accepted in the United States due in large part to the lack of information but probably more from resistance to change. This resistance to change is endemic in the United States construction industry. The construction industry has no single leader that creates or establishes a competency with economic advantage for other to follow. Rather it is a fragmented industry with a number of competitors with little will to affect change. It is efforts like the HUD PATH program working with industry on the concept home that will create the change agent necessary to influence the industry as a whole.

## REFERENCES

1. "About PATH", http://www.pathnet.org/sp.asp?id=15221 (2007), accessed April 20, 2007
2. "Crosslinked Polyethylene (PEX) Tubing", (1998), Plastic Pipe Institute, TN-17.
3. "Differences Between PEX and PB Piping Systems for Potable Water Applications", (2004), Plastic Pipe Institute, TN-31.
4. Gajda, J., & VanGeem, M. (2000), "Energy Use in Residential Housing: A Comparison of Insulated Concrete Form and Wood Frame Walls", Portland Cement Association, Research and Development Serial No. 2415.
5. "ICFs in Residential Construction", http://www.forms.org, (2007) accessed April 22, 2007.
6. Jefferson, B., Laine, A.L., Judd, S.J., & Stephenson, T. (2000) "Membrane bioreactors and their role in wastewater reuse", Water Science and Technology, Vol. 41, No. 1, pp. 197-204.
7. Jeffrey, P., Seaton, R.A.F., Parsons, S.A., Judd, S.J., Stephenson, T., Fewkes, A., Butler, D., & Dixon, A. (2000), "An interdisciplinary approach to the assessment of water recycling technology options", International Journal of Water, Vol. 1, No. 1, pp. 102-117.
8. Ruiz, F.P., (2005), "Better Framing with Factory-built Walls", Fine Homebuilding, February/March, pp. 68-71.

## ACKNOWLEDGEMENT

# HEAVY METALS REMOVAL BY ADSORPTION ONTO PEANUT HUSKS CARBON

**\* Maha m. El shafei , omar e.abdel salam , ne'ama a. Reiad**

*Housing and Building national Research Center – Cairo -Egypt m_elshafai@yahoo.com*
*Faculty of Engineering, Cairo University, Giza, Egypt omarelfaroukabdelsalam@yahoo.com*
*Faculty of Engineering, Cairo University, Giza, Egypt. neama_1973@yahoo.com*

## ABSTRACT

Carbon prepared from peanut husks (PHC), which is derived from agricultural waste has been used for the adsorption of $Cu^{+2}$, and $Zn^{+2}$ from aqueous solutions. Batch isotherm experiments were carried out to evaluate the removal of heavy metals from aqueous solutions; Parameters such as pH, contact time, agitation speed, and initial metal concentration were studied to optimize the conditions to be utilized on a commercial scale for the decontamination of effluents using a batch adsorption technique. The influence of pH of the metal ion solutions on the uptake levels of the metal ions by peanut husk charcoal (PHC) were carried out between pH 4 and pH 11. The optimum pH for copper and zinc removal was 6 and 7, respectively. Equilibrium time 2 h was required for the adsorption of $Cu^{+2}$, and $Zn^{+2}$ onto peanut husk charcoal. Adsorption parameters were determined using both Langmuir and Freundlich isotherms, but experimental data were better fitted to the Langmuir equation than to Freundlich equation, and therefore, it is more suitable for the analysis of kinetics. The results obtained from batch experiments adsorption were used to remove metal ions by column to be utilized on a commercial scale. Break through curves were obtained to investigate the influence of flow rate, and the bed height of the three different adsorbents on the removal of $Cu^{+2}$, and $Zn^{+2}$ ions. The fixed capital investment cost of the proposed column was L.E. 2500, and the annual operating cost was L.E. 5500.

**Keywords:** Adsorption, Agricultural Waste, Decontamination, Industrial Wastewater, Peanut Husk Charcoal (PHC).

## INTRODUCTION

Water Pollution due to the disposal of heavy metals, continues to be a great concern world wide. Consequently, the treatment of polluted industrial wastewater remain a topic of global concern since wastewater collected from municipalities, communities and industries must ultimately be returned to receiving waters or to the land [20]. Heavy metals pollution occurs in many industrial wastewater such as those produced by metal plating facilities, mining operations, battery manufacturing processes, the production of paints and pigments, ceramic and glass industries. This wastewater commonly includes Cd, Pb, Cu, Zn, Ni and Cr [3]. Whenever toxic heavy metals are exposed to the natural eco-system, accumulation of metals ion in human body will be occurred through either direct intake or food chains. Therefore, heavy metals should be prevented before it reaches to the natural environments because of its toxicity [14]. In order to remove toxic heavy metals from water systems, conventional methods have been used such as: chemical precipitation, coagulation, ion exchange, solvent extraction; filtration, evaporation, and membrane methods [10]. Activated carbon is widely used as an effective adsorbent in many applications, it is the most commonly used adsorbent in the adsorption process for the treatment of wastewater, Activated carbon produced by carbonizing organic materials is the most widely used adsorbent. However, the high cost of the activation

process limits its use in wastewater treatment. [1]. Over the last few years number of investigations has been conducted to test the low cost adsorbents for heavy metal ion removal. Agriculture wastes are mainly comprised of cellulose materials that can adsorb heavy metal cations in aqueous medium. The utilization of agricultural waste materials is increasingly becoming a vital concern because these wastes are of little or no value and present serious disposal problems [9], these includes peanut hulls, rice husk & straw, corn cobs, saw dust, barks, rice and wheat bran [1]. Peanut husks widely available in Senegal are of no economic value and in fact present a disposal problem. The vast quantity is generally dumped in landfills [18]. Periasamy and Namasivayam (16) studied the use of Peanut hull carbon for the adsorption of Cu (II) from wastewater, comparative study with a coal based commercial granular activated carbon (GAC) showed that the adsorption capacity of PHC was 18 times larger than that of GAC. Other researcher has studied the removal of lead form aqueous solution onto dried peanut husk using column adsorption experiments [6]. Another researcher have studied the removal of heavy metals using rice husk [11], batch and column adsorption studies indicate that rice husk could be used to remove (Ni, Zn, Cu, and Pb) in single and mixed metal solutions effectively.

The objective of this work is to study the feasibility of using peanut husk charcoal (PHC) to remove copper and zinc from wastewater streams using batch technique, the effect of different parameters namely, pH, contact time; agitation speed, and initial metal concentration on the adsorption capacity were studied, the equilibrium data is described by Freundlich and Langmuir adsorption isotherms. Continuous column adsorption experiments were conducted to evaluate peanut husk charcoal (PHC) for copper and zinc removal in combination.

## EXPERIMENTAL WORK

### Materials
### Preparation of Adsorbent
Peanut husks were washed thoroughly to remove dust using distilled water, then dried in an oven at 60 º C for 18 hours, then ground using a laboratory mill and sieved to 0.5 – 0.8 mm, and rinsed using 0.1 N HCl, Then the pH was adjusted with 0.1 N HCl at values (6 – 7), PHC was dried and stored in an oven at 80ºC till reach constant density and humidity [18].

### Characterization of PHC
The surface area of PHC has been found equal to 485 $m^2g^{-1}$. This value is very high in comparison with other carbons which have a surface area about 10 – 100 $m^2g^{-1}$, Moreover, most PHC have areas of pores whose diameters were less than 3.5 nm. It seems that the PHC used were also micro porous. The chemical composition of PHC was shown in Table (1), values are expressed in w/w. The adsorption capacity of carbon is strongly influenced by the chemical structure of their surface. The surface structures of carbon-oxygen (functional groups) suggested most often are carboxyl groups, phenolic hydroxyl groups, carbonyl groups (e.g. quinone type), and lactone groups.

### Reagents
Stock solutions of copper chloride and zinc chloride of 400 mg/l were used as adsorbate, and solutions of various concentrations were obtained by diluting the stock solution with distilled water. Copper and zinc concentrations were determined by spectrophotometer. All the chemicals used were of analytical grade reagent and all experiments were carried out in 500 ml glass bottles.

### Batch adsorption experiments
Batch adsorption experiments were carried out by shaking a series of bottles containing various amounts of the different adsorbents used and heavy metal ion at optimum pH, A predetermined amount of the adsorbents used was mixed with 500 ml of distilled water with adsorbent dose 5 g/l, the pH of the mixture was adjusted to the desired value with 0.1 M HCl and 0.1 N NaoH until the pH was stabilized, and was agitated in a jar test at 27 ºC $\pm$2 ºC for 1 hour, then the copper and zinc ions in the form of chloride salts were added to the bottles to make initial concentration 10-100 mg/l, and the bottles were agitated for further 1 hour until the equilibrium was attained, at the end of mixing the adsorbent particles were separated from the suspensions by filtration through 0.43 µm filter paper. The residual concentration of heavy metals was determined by the

spectrophotometer, In addition to adsorption tests, a set of blank tests was conducted to evaluate the removal by metal hydroxide precipitation at various pH's.

**Table 1:  Chemical composition of PHC**

| Elements | C | H | O | N | Ca | Na | K | Al | Fe | Si |
|----------|----|----|------|-----|-----|-----|-----|----|----|----|
| % | 56 | 1 | 15.8 | 0.5 | 1.2 | 2.7 | 2.6 | 1 | 1 | 20 |

**Column adsorption experiments**

The results obtained from batch adsorption experiments were used to remove metal ions by column. Column flow experiment was conducted in

PVC columns with dimensions 8 cm internal diameter, and 100 cm length. Columns ends were fitted with filter disk (Millipore) to retain the material. The peanut husk charcoal was used to pack the column up to 30 cm. Column was shaken while being packed to minimize void volumes and air gaps. heavy metals such as Cu and Zn were spiked in the deionized water to have final concentration of Cu and Zn ions 12 mg/l and 10 mg/l, respectively, then adjusted to optimum pH in the range pH 6 – 8 with 0.1N NaoH and 0.1M HCL then pumped through the adsorber column using pump. The column experiments were carried out at room temperature 25 $\pm$ 2 ºC, Three different flow rates 2, 4 and 8 dm$^3$/hr was percolated through column of 10, 20 and 30 cm. Finally the effluent was discharged into the drain. Samples were taken at different positions, at appropriate time intervals. Effluent samples were collected every 1 hour. Filtered, preserved and determined the concentrations of copper and zinc ions by the spectrophotometer.

## RESULTS AND DISCUSSIONS

**Effect of pH**

The pH of the solution has a significant impact on the uptake of heavy metals, since it determines the surface charge of the adsorbent, and the degree of ionization and speciation of the adsorbate [5].The results obtained are shown in Figure (1) which shows the effect of pH on the adsorption of Cu$^{2+}$, and Zn$^{2+}$ ions from the aqueous solution on peanut husk charcoal, in terms of the metal ions removed percent. It is clear that Cu$^{2+}$, and Zn$^{2+}$ ions were effectively adsorbed in the pH range (4-7), and the maximum adsorption of Cu$^{2+}$, and Zn$^{2+}$ ions using peanut husk charcoal occurred at pH 6, 7, respectively, thus, those pH values was chosen for all experiments. These results are similar to results obtained by Rodda et al. [19] for heavy metal ion sorption on agricultural waste sorbents.

The results in Figure (1) showed that the equilibrium capacity of copper and zinc removal by peanut husk charcoal increased significantly as the pH of the solution increased. If the initial pH was too high, copper and zinc ions precipitate out and this defect the purpose employing the sorption process as the sorption process is kinetically faster than the precipitation. [2]. the adsorptive capacities of Cu$^{+2}$, and Zn$^{+2}$ ions increased rapidly as the pH value increased. At pH value above the range 5-6 the adsorptive capacities of Cu$^{+2}$, and Zn$^{+2}$ ions increased but at a slower rate because of the competitive adsorption between hydrogen ion and the heavy metal cation [8].
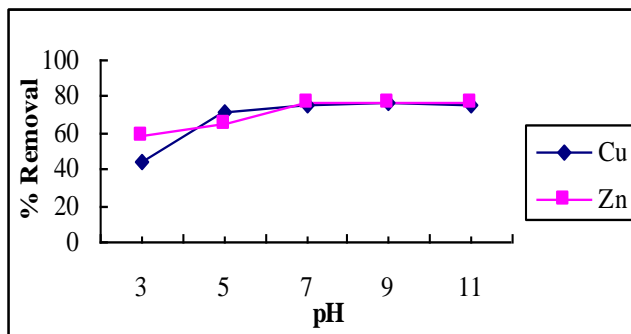


**Fig. 1: Effect of pH on copper and zinc removal by peanut husk charcoal**

**Effect of contact time**

Effect of contact time on the removal efficiency of peanut husk charcoal for copper and zinc ions was studied, and the results are shown in Figure (2), the rate of uptake of metal ions was rapid; the metal removal in the first 30 minutes was 67 % and 64 % of the maximum removal for copper and zinc, respectively. Equilibrium was reached within 2 h for copper, and zinc. At equilibrium, 72 % of copper ions, and 70.6 % of zinc ions were removed from the solution. Similar results were reported by Recordel et al. [18], who studied heavy metals removal by adsorption onto peanut husk charcoal.
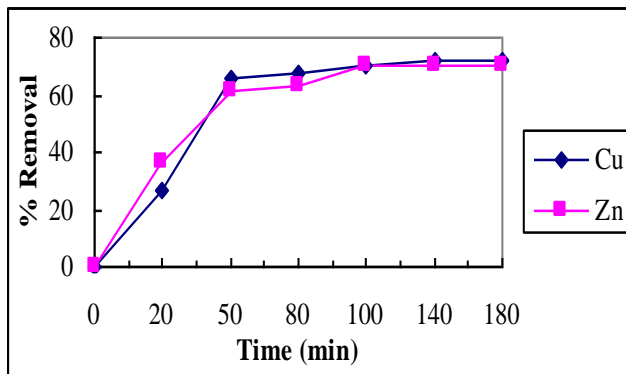


**Fig. 2: Effect of contact time on copper and zinc removal by peanut husk charcoal**

**Effect of agitation speed**

The effect of agitation speed on the percent removal of Cu(II) and Zn(II) was studied with different agitation rate (50- 300 rpm). The results are shown in Figure (3) which indicate that the percent of adsorption increases with increasing agitation rate, these is due to disperse of the adsorbent particles in the aqueous solution which lead to reduce the bounding layer resistance to mass transfer and even it may increase the velocity of particles, so that increase in the percent removal of metal ions [13]. The percentage of adsorption increased to attain a maximum removal at rpm 200 and above rpm 200 the increase in removal efficiency is not significant.
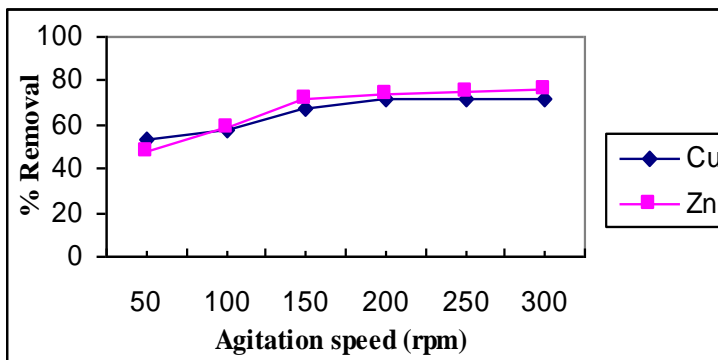


**Fig. 3: Effect of agitation speed on copper and zinc removal by peanut husk charcoal**

**Effect of initial metal concentration**

The effect of initial metal concentration on copper and zinc removal was studied by batch adsorption experiments which carried out at 27 ± 2 ºC using different initial metal ion concentration (10, 20, 40, 60, 80 & 100 mg/l) at optimum pH 6-7, The results are shown in Figure (4) which indicate that the percentage removal decreases with the increase in initial metal ion concentration.
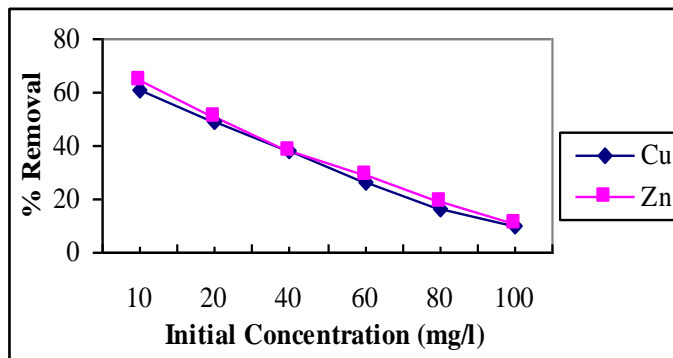
**Fig. 4: Effect of initial metal concentration on copper and zinc removal by peanut husk charcoal**

**Adsorption Isotherm**

An adsorption isotherm equation is an expression of the relation between the amount of solute adsorbed and the concentration of the solute in the fluid phase, since the adsorption isotherms are important to describe how adsorbates will interact with adsorbents and so are critical for design purposes [8]. Two isotherm equations were adopted in this study (i.e.)

*(a) Freundlich Isotherm Equation*

The Freundlich sorption isotherm, one of the most widely used mathematical descriptions. This isotherm gives an expression encompassing the surface heterogeneity and the exponential distribution of active sites and their energies, *The Freundlich isotherm* is defined as:

$$Q_e = k\ C_e^{\ 1/n} \qquad (1)$$

and in linearized form is:

$$\log Q_e = \log k + (1/n) \log C_e \qquad (2)$$

Where $C_e$ is the equilibrium concentration in mg/l, $Q_e$ is Amount of adsorbate adsorbed per unit weight of adsorbent (mg/g). k is a parameter related to the temperature and n is a characteristic constant for the adsorption system under study, The plots of $\log Q_e$ against $\log C_e$ are shown in Figure (5) for adsorption of copper and zinc ions onto peanut husk charcoal gave a straight line, values of n between 2 and 10 show good adsorption [7]. The Freundlich isotherm constants and their correlation coefficients $R^2$ are listed in Table (2).

**Table 2: Freundlich constants for the sorption of Cu & Zn ions onto peanut husk harcoal**

| Metal ion | Freundlich constants | | Correlation Coefficient |
|---|---|---|---|
| | k | n | $R^2$ |
| Cu | 2.814 | 3.67 | 0.97 |
| Zn | 2.604 | 3.604 | 0.95 |

*(b) Langmuir Isotherm equation*

Langmuir equation is based on the assumptions that maximum adsorption corresponds to saturated mono-layer of adsorbate molecules on the adsorbent surface, that the energy of adsorption is constant, and that there is no transmigration of adsorbate in the plane of the surface [17], *The Langmuir isotherm* is defined as :

$$q_e = (b\ q_m\ C_e)/(1+bC_e) \qquad (3)$$

and in linearized form is:

$$C_e/q_e = (C_e/q_m) + 1/(b\ q_m) \qquad (4)$$

Where $q_m$ and b are Langmuir constants related to the sorption capacity, and sorption energy, respectively, $C_e$ is the equilibrium concentration in mg/l, and Qe is the amount of adsorbate adsorbed per unit weight of adsorbent (mg/g). The plots of $C_e/q_e$ against $C_e$ are shown in Figure

(6) for adsorption of copper and zinc ions on peanut husk charcoal gave a straight line. The Langmuir isotherm constants and their correlation coefficients $R^2$ are listed in Table (3).

**Table 3: Langmuir constants for the sorption of Cu & Zn ions onto peanut husk charcoal**

| Metal ion | Langmuir constants | | Correlation Coefficient |
|---|---|---|---|
| | $Q_m$ | b | $R^2$ |
| Cu | 0.3451 | 4.071 | 0.988 |
| Zn | 0.3681 | 1.986 | 0.981 |

As can be observed, experimental data were better fitted to the Langmuir equation ($R^2 = 0.98$) than to the Freundlich equation, and therefore, it is more suitable for the analysis of kinetics. Consequently, the sorption process of metal ions on PHC follows the Langmuir isotherm model where the metal ion are taken up independently on a single type of binding site in such a way that the uptake of the first metal ion does not affect the sorption of the next ion. Budinova et al. [4], and Lopez et al. [12] reported a similar relationship when active carbon obtained from different raw materials were used as the adsorbent.
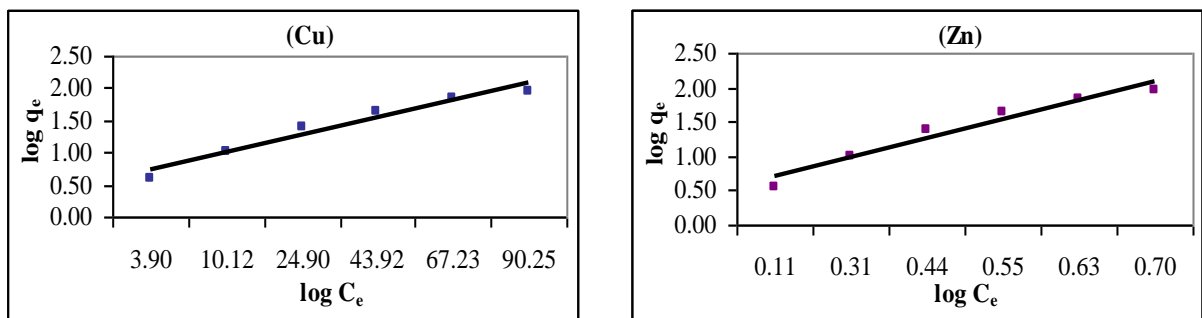


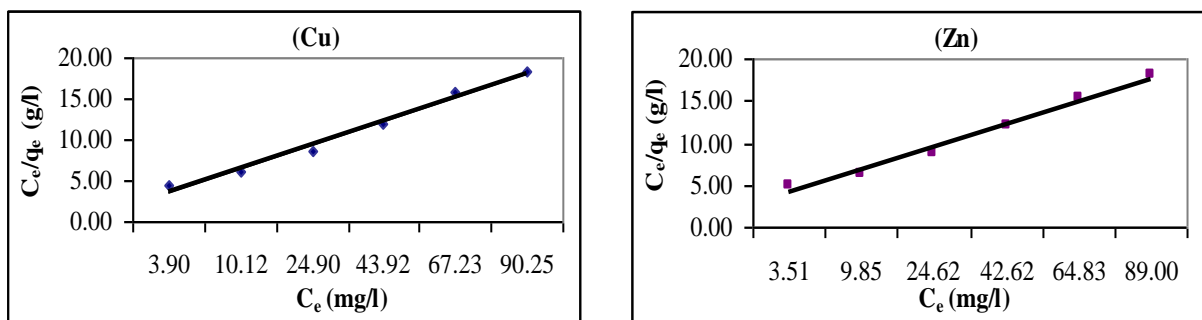**Fig. 5: Freundlich plot for peanut husk charcoal for copper and zinc**



**Fig. 6:  Langmuir plot for peanut husk charcoal for copper and zinc**

**Column Adsorption studies**
The results obtained from batch adsorption experiments were used to remove metal ions by column. Typical 'S' shaped curves were obtained for all experiments, where $C_t$ represents the time-dependent outlet metal concentration of the bed and $C_o$ the inlet concentration. The higher the column capacity may be due to the fact that a continuously large concentration gradient occurred at the interface as it passes through the column, while the concentration gradient decreases with time in the batch experiment. As shown in Figures (7, 8) every experiment indicates that at the same flow rate 2 l/h, increasing column height giving an increase in the adsorption capacity. The flow rate of the effluent was varied to achieve the maximum removal of peanut husk charcoal, and it was found that the maximum uptake of metal ions was achieved at flow rate 2 l/h, which illustrates in figures not shown here. Every experiment indicates that at the

same bed depth 30 cm, decreasing flow rate giving an increase in the adsorption capacity for the adsorbent.
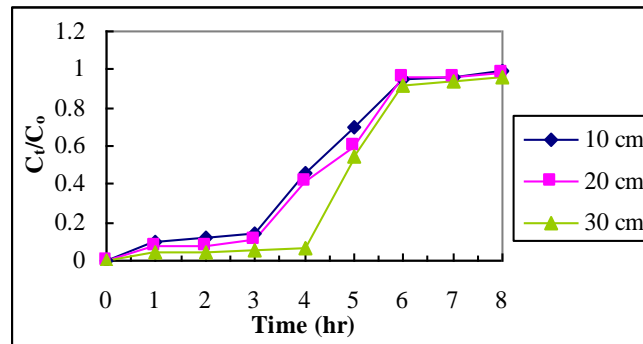


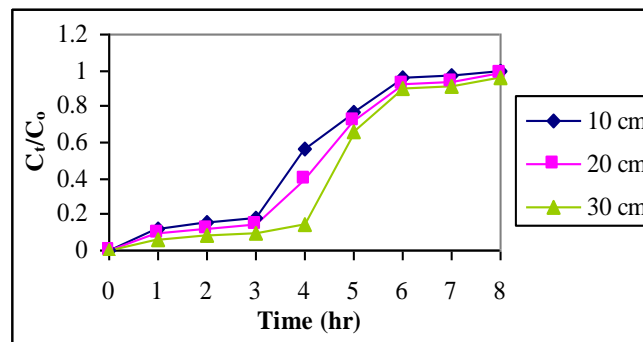**Fig. 7: Breakthrough curve for adsorption of copper onto peanut husk charcoal at different bed depth, flow rate 2 l/h**



**Fig. 8: Breakthrough curve for adsorption of zinc onto peanut husk charcoal at different bed depth, flow rate 2 l/h**

**Treatment of metal industrial wastewater**

A preliminary design of a proposed commercial fixed bed column for the treatment of wastewater from a local plating industry showed that, the column dimensions were 240 cm in height, 36.6 cm in diameter, and 137 cm bed depth, for the treatment of effluent with flow rate 1 $m^3$/day, with average copper and zinc concentration 11.4, 8.5 mg/l, respectively, raw wastewater was pumped through the column with flow rate 2 l/h. The percent removal of copper and zinc from raw wastewater were 66, 62 %, respectively.

**Cost of adsorbent**

Commercial activated carbon of cheapest variety cost L.E.16000 /ton, peanut husk cost is 4000 L.E./ton. The finished products would cost approximately 5500 L.E./ton by adding all expenses (Transportation, handling, chemicals, electrical energy, drying,…. etc.)

## CONCLUSIONS

Peanut husk charcoal is an effective adsorbent for the removal of $Cu^{+2}$ and $Zn^{+2}$ from aqueous solutions. Parameters such as pH, contact time, agitation speed and metal concentration were studied at ambient temperature using batch method.The optimum pH corresponding to the maximum adsorption of copper and zinc removal was 6, 7, respectively, Copper and zinc ions were adsorbed onto the Peanut husk charcoal very rapidly within the first 30 minutes, while equilibrium was attained within 2 hours for copper and zinc ions. Langmuir isotherm better fitted the experimental data for both metals. In the column adsorption experiments, the adsorption efficiency depends on column height and flow rate, the increase in column height and decrease

in flow rate make adsorption efficiency increase. The maximum metal ion removal for the three different adsorbents used was achieved at flow rate 2 l/h, and bed height 30 cm.

## REFERENCES

1. Amarasinghe B., Williams R.A., "Tea waste as a low cost adsorbent for the removal of Cu and Pb from wastewater", Chemical Eng. Journal, No.132, 2007, p.p. 299-309.
2. Appel C, Lena M., "Concentration,  pH, and surface charge effects on cadmium and lead sorption in three tropical soils", J. Environ. Qual. No. 31, 2002, p.p. 581-589.
3. Argun M.E., Dursun S., "A new approach to  modification of natural adsorbent  for heavy metal  dsorption",  Bioresource Technology, Vol. 3(1), 2007, pp. 101-112
4. Budinova T.K., Gergova K.M., Petrov N.V.,  J.Chem. Tech. Biotechnol. 60 (1994), pp. 177.
5. Cho H., Dalyoungoh, Kwanho kim, "A study  on removal characteristics of heavy metals from aqueous solution by fly ash", Journal  of Hazardous Materials,  B127, 2005, pp.187–195.
6. Disyawongs G. and Boonsong "Agro-industrial waste as adsorbent of $Pb^{+2}$ from solution onto dried peanut husk", 7th International Symposium on waste management,  Amsterdam, 27–29 Sep., 2006.
7. Erdem E., Karapinar N., Donat R., "The removal of  heavy metal cations by  natural zeolites", Journal of colloid and interface science, 280  (2004) , p.p. 309 – 314
8. Hashem M.A., "Adsorption of lead ions from aqueous solution by okra wastes", International Journal of physical sciences, Vol. 2(7), 2007,  pp. 151-157.
9. Igwe J.C. and Abia A.A., "Adsorption kinetics and intra particulate diffusivities for bio-remediation of Co(II), Fe(II), and Cu(II) ions from wastewater using maize cob", International journal of physical sciences, Vol. 2(5), May 2007, pp. 119-127.
10. Jai P. H., Jeong Wook, Yang Jae Kyu, "Removal of heavy metals using waste eggshell", Journal of Environmental Sciences,  No.19, 2007,  pp. 1436 – 1441.
11. Krishnani  K.K. , Xiaoguang Meng, C. Christodoulatos, Veera M. Boddu, "Biosorption mechanism of nine different heavy metals onto biomatrix from rice husk", Journal of Hazardous Materials, Vol. 3(1), 2007, p.p. 1-13.
12. Lopez-Delgado A., Perez C., Lopez F.A., Water Res., No. 32, 1998, pp. 989.
13. Mahmoud M.A., Daher A., Aghareed M.Tayeb, "Adsorption of heavy metal from industrial wastes by some agricultural by products", 18th International Conference on solid waste technology and management,      Philadelphia, USA, 23 – 26 March   2003.
14. Meena A. K., Kadirvelu K., Mishra G.K. , "Adsorptive removal of heavy metals from aqueous solution by treated saw dust", Journal of Hazardous Materials, Vol. 2(5), 2007, p.p.1-8
15. Netzer A, Hughes DE. "Adsorption of copper, lead, and cobalt by activated carbon", Water Res., 18(8), 1984, pp. 927-33.
16. Periasamy K. and Namasivayam C.,"Removal of Cu (II) by adsorption onto peanut hull carbon from water and copper plating industry wastewater", Chemosphere, No.32(4), 1996, pp. 769- 789.
17. Periasamy K. and Namasivayam C., "Removal  of Ni (II) from aqueous solution using an agricultural waste: peanut hulls", Waste  management, Vol. 15, No.1, 1995, pp. 63-68.
18. Recordel S., Taha S., Cisse I., "Heavy metals  removal by adsorption onto peanut husks carbon", Separation and purification  technology 24 (2001), pp. 389 – 401.
19. Rodda D, Johnson B, Wells, "The effect of  temperature and pH on the adsorption of copper(II) , lead(II) and zinc(II)onto goethite", J.Coll. Interface Sci., No. 161, 1993,  pp. 57-62.
20. Weber WJ, Jinley MC, Katz L, "Sorption  phenomena in subsurface systems: concepts, models ", Water Res. ,Vol. 25, 1991, pp. 499- 52

# SPEECH COMPRESSION TECHNIQUES BASED ON GAUSSIAN MIXTURE MODEL AND WAVELET ANALYSIS

**\* Mahmoud I. Abdalla, Mahammed M. Fouad, Adel M. Zaglol and Rania A. Elsayed**

*Electronics & Communications Engineering Department, Zagazig University, Egypt*

**Khalid . Fawzy**

*Electronics Research Institute (ERI), Dokki, Cairo, Egypt,*

## ABSTRACT

The basic goal of speech data compression is to reduce the bit rate for transmission and storage while either maintaining the original quality or providing an acceptable fidelity. This article introduces two techniques for Arabic speech compression based on Gaussian Mixture Model (GMM) and Wavelet Transform (WT). The performance evaluation of these techniques is carried out. The Expectation Maximization (EM) is used to extract the GMM model.
A supervised learning technique is implementing based on EM algorithm to evaluate the model parameters of the probability density function (pdf). The probability density function is used to build an optimized quantizer based on Lloyed algorithm.Different compactly supported wavelet functions are investigated to get the proper wavelet function which should be used for Arabic speech compression. The effect of increasing the level of decomposition and threshold values on the compression ratio are also investigated. Different compression ratios at different signal to noise ratios are calculated. The results show that the compression ratio becomes approximately constant after level 3. The results also show that the Bior3.1 and Db10 wavelet functions give the highest compression ratio. A comparison between the two techniques is given. The speech quality after compression is measured using MOS ranking test.

**Keywords:** Speech compression, Speech coding, Expectation-maximization algorithm, Gaussian mixture models and Wavelets analysis.

## INTRODUCTION

Speech coding has enjoyed successful period during the past decades. A major objective in speech coding is to compress the signals that is, to employ a few bits as possible in digital representation of the speech signals. The efficient representation of the speech signal makes it possible to achieve bandwidth efficiency in transmission of the signal over a variety of communication channels or to store it efficiency on a variety of magnetic and optical media.
Speech coding research started over sixty years ago with the pioneering work of Homer Dudley [1] of Bell Telephone Laboratory. Many researches have been carried out to improve and reduce the bit rate [2,3,4,5,6] of speech transmission.Progress in speech coding, particularly in the late of eighties, enabled recent adoptions of low-rate algorithms for mobile telephony.
An 8 kbits/s hybrid coder has selected for North America digital cellular standard [2] and a similar algorithm has been selected for the 6.7 kbits/s Japanese Digital cellular standard [5]. In Europe, a standard that uses a 13 kbits/s regular pulse excitation algorithm has been completed and partially deployed by the "Group Special Mobil" [7]. Parallel standardization efforts for secure military communications have resulted in adoption of a 4.8kbits/s hybrid algorithm for Federal standard 1016[8]. In addition, a 6.4kbits/s improved multi-band excitation coder [6] has been adopted for the International Maritime Satellite system [9]. Speech coding algorithms are still needed to be robust against background noise of various levels and kinds . Low complexity

---

speech coding with low rate is still needed. Rainer and Schafer discussed the different digital speech coding techniques [10]. This article introduces two techniques based on Gaussian Mixture Model (GMM) and wavelet analysis for speech compression applied to Arabic speech files. In GMM techniques, the Expectation Maximization (EM) algorithm is used to construct a Gaussian mixture model as an estimation of the underlying probability distribution function for a given set of random data (training data). The random data may represent a set of values obtained from one-dimensional (scalar) or multidimensional (vector) source.

The obtained probability density function *pdf* is then used to compress speech signals through non-uniform quantization [11]. This technique directly uses the estimated probability distribution function (GMM) to determine the quantization levels for one-dimensional source or the codevectors (codebook) for two-dimensional source of the quantizer. This design is based on distribution these quantization levels according to estimated probability density function pdf. After this, we carry out quantization process. In WT techniques, speech signal is transformed from time domain to other different domain. Wavelet transform (WT) represents now one of the most important tools in signal analysis. It is one of the methods used for time frequency representation of signals giving an indication to which spectral components are present at which time. The fundamental idea behind wavelets is to analyze according to scale. In the case of wavelets, it is better to speak about time-scale representations not time-frequency representations, scale being in a way the opposite of frequency, because the term frequency is reserved for the Fourier transform. A wavelet analysis is capable of revealing aspects of data that other signal analysis technique such as Fourier analysis miss and can be used to analyze non-stationary, time-varying, or transient signals [12,13,14]. Wavelets concentrate speech information (energy and perception) into a few neighboring coefficients. Therefore, many coefficients will either be zero or have negligible magnitudes. In this work, data compression is then achieved by truncating small-valued coefficients and replacing them with zeros. Experiments are carried out to get the optimal wavelet function and the optimal decomposition level. Performance of a coding algorithm is primarily specified by the speech quality at the prescribed coding rate. Speech quality can be measured subjectively and objectively. Subjectively measurements are obtained as consequences of listening tests, whereas objectively measurements are computing directly from the coded speech parameters. Typical subjective measures often quoted are Mean Opinion Score or MOS ranking, Diagnostic Acceptability Measure (DMA), and Diagnostic Rhyme Test (DRT). The MOS, probably the most widely used, is obtained by averaging test results rated by a group of listeners who are asked to quantify their perceptual impressions on a five point scale (bad=1, poor=2, fair=3, good=4, excellent=5) [15]. A good objective measure should be able to consistently predict the subjective quality of the speech. Widely used objective measures include squared error and signal to noise ratio [16].

## NON-UNIFORM QUANTIZATION

It is desired to design a quantizer that minimizes the mean square quantization error. It is necessary to know the probability distribution of the sample values so that the most probable samples will incur less error than the least probable samples. To apply this idea to design a non-uniform quantizer for speech requires an assumption of an analytical form for the probability distribution [17]. While a non-uniform quantizer provides lower average distortion, the design of non-uniform quantizer is also somewhat more complex. However, the basic idea is quite straightforward: find the decision boundaries and reconstruction levels that minimize the mean squared quantization error. Fig.1 shows the input/output relationship for the non-uniform quantizer.

Let us denote the decision boundaries by $\{b_i\}_{i=0}^{M}$, the reconstruction levels by $\{y_i\}_{i=1}^{M}$, and the quantization operation by Q (.). Then

$$Q(x) = y_i \qquad if \qquad b_{i-1} \prec x \le b_i . \tag{1}$$

The mean squared quantization error is given by:

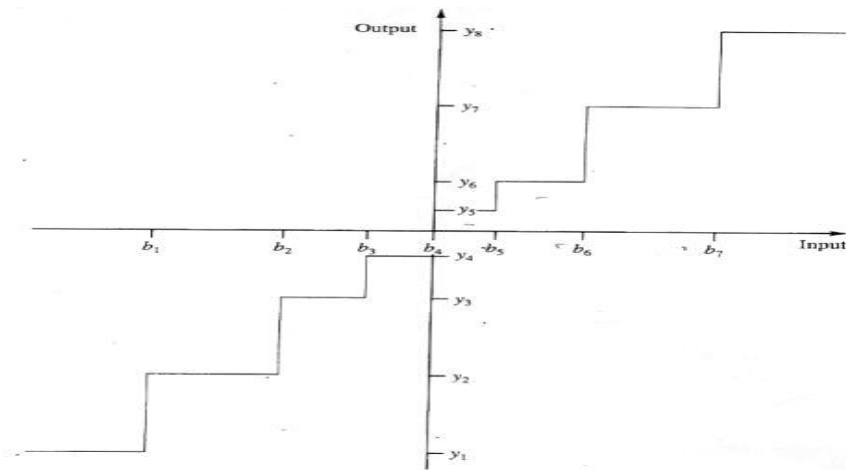$$\sigma_q^2 = \int_{-\infty}^{\infty} (x - Q(x))^2 \ f_x(x) \ dx \tag{2}$$

**Fig.1: Non-uniform quantizer input/output relation.**

$$= \sum_{i=1}^{\infty} (x - y_i)^2 \, f_x(x)dx \qquad\qquad (3)$$

It is supposed that the random variable x is modeled by probability density function $f_x(x)$.

A direct approach for locating the best non-uniform quantizer is to find the $\{b_i\}_{i=0}^{M}$, and $\{y_i\}_{i=1}^{M}$ that minimize the Equation (3). Setting the derivative of Eq. (3) with respect to $y_i$ to zero and solving for $y_i$, then [17}:

$$y_j = \frac{\displaystyle\int_{b_{j-1}}^{b_j} x f_x(x)dx}{\displaystyle\int_{b_{j-1}}^{b_j} f_x(x)dx} \qquad\qquad (4)$$

Taking the derivative with respect to $b_i$ and setting to zero, we get:

$$b_j = \frac{y_{j+1} + y_j}{2} \qquad\qquad (5)$$

The decision boundary is simply the midpoints of the two neighboring reconstruction levels. Solving these two equations will give the values for the reconstruction levels and decision boundaries that minimize the mean square quantization error. Joel Max [18] showed how to solve the two equations iteratively. Lloyed established the fundamentals of optimum quantization [19]. Lloyed gave an algorithm for designing optimum non-uniform quantizers based on sampled speech signals. Optimum non-uniform quantizers can improve the signal to noise ratio by 6dB over μ law quantizer with the same number of bits [19].

## TECHNIQUES

### Gaussian Mixture Model *(GMM)*
The job of determining the optimal compression scheme would be greatly facilitated by knowledge of the underlying probability distribution of the data vectors. In practical applications, the probabilistic model of the data is sometimes dynamic and rarely fits a standard distribution like a Gaussian distribution. However, much like the decomposition of periodic signals into the sum of sinusoids, the probability density of a data source can be estimated as the finite sum of standard distributions. The standard distributions are taken as Gaussians, and the result is a Gaussian Mixture Model (GMM).

The most common technique used to determine the parameters of the GMM is the expectation maximization (EM) algorithm [20]. The EM algorithm was introduced by Dempster et al. (1977), who also presented its main properties [20]. The EM algorithm is an efficient iterative procedure to compute the maximum likelihood estimation (MLE) In MLE, we wish to estimate the model parameters $\theta$ for which the observed data (given data $X$) are the most likely. Each iteration of the EM algorithm consists of two processes: The E-step, and the M-step. In the expectation, or E-step, the missing data are estimated given the observed data and current estimate of the model parameters. In the M-step, the likelihood function is maximized under the assumption that the missing data are known. The estimates of the missing data from the E-step are used in lieu of the actual missing data [21]. Convergence is assured as the algorithm is guaranteed to increase the likelihood after each iteration. So, The EM algorithm is numerically stable with each EM iteration increasing the likelihood.

Density estimation for random observed data has been done using two different approaches namely [22]: (1) parametric density estimators (those that make strong assumptions about the distribution of the sampled data) and (2) non-parametric estimators (those that make weak distributional assumptions). In the parametric density estimation it is assumed that the unknown probability density function of the source, $f(x)$, belongs to a family of parametric densities, $f(x|\theta)$. The goal here is to find the particular value of the parameter $\theta$ such that best $f(x|\theta)$ explains the observations data. This technique falls in the field of maximum likelihood parameter estimation. The main advantage of this approach is computationally efficient, since the parameter can be estimated from a fairly small number of observations which linearly grows with the number of parameters [23]. However, the main drawback of this approach is the enforcement of a priori structure on the observed data and hence this approach can lead to poor estimates of the unknown *pdfs* in those cases where this assumption is invalid. Non parametric density estimation does not make any prior assumption about the unknown probability density function. They estimate the unknown probability density function relying only on the observations at hand. Therefore, the estimation is consistent which roughly means that if the number of samples is large enough, each estimated value is very close to true value irrespective of the unknown probability density function. However, non parametric techniques need large number of observations to make their estimates. It is well known that the number of training samples scales exponentially with the dimension of the problem [22,23]. So, in order to solve problem density estimation using mixture models, which lie in the class of quasi parametric model estimation, an estimator has been introduced in [23]. This method benefits from the advantages of both previously mentioned methods [24].

In this approach, the unknown probability density function is modeled as a mixture of parametric (Gaussian) probability density functions *pdf's*,

$$f(x|\theta) = \sum_{k=1}^{K} \alpha_k \, f_k(x|\theta_k) = \sum_{k=1}^{K} \alpha_k \, \phi(x|\mu_k, C_k) \qquad (6)$$

$$\theta = [K, \alpha_1, ..., \alpha_K, \ \theta_1, ..., \theta_K] \qquad (7)$$

where $\alpha_k \geq 0$; $k = 1, ..., K$ are the mixture weights (or the amplitude of each parametric probability density functions), with $\sum_{k=1}^{K} \alpha_k = 1$, and $f_k(x|\theta_k)$, $k = 1, ..., K$ is an individual parametric density parameterized by $\theta_k$ of component $k$ in *N*-dimensional space with mean vector $\mu_k$ and covariance matrix $C_k$ given by [24]:

$$f_k(x|\theta_k) = \phi(x|\mu_k, C_k) = \frac{1}{\sqrt{(2\pi)^N |C_k|}} \exp\left(\frac{-(x-\mu_k)^t C_k^{-1}(x-\mu_k)}{2}\right) \qquad (8)$$

where the superscript $(\cdot)^t$ indicates the transpose of a matrix or vector and *x* is an N-dimensional vector. The parameter $\theta$ is the parameter set which defines the quasi parametric model; each $\theta_k = \{\mu_k, C_k\}$ represents the two elements: mean vectors and covariance matrices of each Gaussian component. Here $K$ is the number of the Gaussian probability

density function in the mixture model. Each Gaussian distribution is parameterized by $\mu_k$, $C_k$. Then the result is a GMM. GMM assumes that data points are generated from a set of Gaussian models with the same set of mixture weights. The most popular algorithm used to compute the model parameters $(\theta)$ that maximize the likelihood (or log likelihood) of the GMM, given the training data is the EM algorithm. The expression for the GMM likelihood is a nonlinear function of the parameters. So, direct maximization is not possible [25].Due to the fact that GMMs use a discrete set of Gaussian functions, each with their own mean and variance, it is expected that the GMM have several different "shapes", depending on the form of their covariance matrices. The two most widely used forms are full and diagonal covariance matrices. The full covariance matrix models the data that is correlated whereas diagonal covariance matrices (the non-diagonal elements are zeros) model the data that is uncorrelated. In this work, The EM algorithm assumes multidimensional random data with "full" covariance matrices i.e. it assumes that the training vectors have their components as correlated random variables. The iterative EM algorithm for GMM can be described as follows [24]:

**Initialization**
In this step an initial estimation of the parameters is obtained. For all values of $k$ the weight coefficients are initialized to $1/K$. The mean vectors are initialized either to a random vector or a vector randomly chosen from the training data base $X$ as well as the covariance matrices [23].

**E-step (likelihood computation)**
In each iteration, $p$, the posterior probabilities is computed [23] for all $i = 1, ..., n$, $k = 1, ..., K$.

$$P_{i,k} = \frac{\alpha_k^{(p)} \, \phi\left(x_i \,\middle|\, \mu_k^{(p)} , C_k^{(p)}\right)}{\sum\limits_{k=1}^{K} \alpha_k^{(p)} \, \phi\left(x_i \,\middle|\, \mu_k^{(p)} , C_k^{(p)}\right)} \tag{9}$$

where $p_{i,k}$ shows the posterior probability that given the observation vector $x_i$ and the parameter $\theta$ is generated by the $k\,th$ cluster.

**M-step:  (parameter update)**
Having the posterior probabilities, the weights, mixture means and covariances are computed by [23]:

$$\alpha_k^{(p+1)} = \frac{\sum\limits_{i=1}^{n} P_{i,k}}{n} \tag{10}$$

$$\mu_k^{(p+1)} = \frac{\sum\limits_{i=1}^{n} P_{i,k} \, x_i}{\sum\limits_{i=1}^{n} P_{i,k}} \tag{11}$$

$$C_k^{(p+1)} = \frac{\sum\limits_{i=1}^{n} P_{i,k}(x_i - \mu_k)(x_i - \mu_k)^t}{\sum\limits_{i=1}^{n} P_{i,k}} \tag{12}$$

**Step 2 and 3 are repeated until convergence occurs.**
For the purposes of transmission and storage, there is a need to build quantizers with reasonable search and computational complexity that provide good performance relative to a

relevant distortion measure. Conventional non-adaptive quantization schemes design the quantizer using a large database of the source called the training data. The training data is so chosen that it encompasses all possible statistics of the source. In this work, the EM algorithm and its variants provide a way to extract an approximation of the distribution of the source (i.e., a GMM), which could then be used for designing the quantizer. Thus the relatively small parameter set of a GMM could replace, with possibly the induction of a slight reduction in performance, an entire training set. There are many ways to use a GMM to design a quantizer. If the GMM adequately models the data, then it serves as an alternate, compact representation of that data. The problem of quantizer design for a random source may be conveniently broken down into one of estimating the probability density function *(pdf)* of the random source and then efficiently quantizing the estimated *pdf* through non-uniform vector quantizer VQ to get codevectors.

**Wavelet Decomposition Technique**

Wavelet analysis is a relatively new mathematical discipline, which has generated much interest in both theoretical and applied mathematics over the past decade. Wavelets have the ability to analyze different parts of a signal at different scales. The wavelet transform (WT) is a transformation that provides time-frequency representation of the signal or image. The continuous one dimensional WT is a decomposition of *f(t)* into a set of basis function $\Psi_{a,b}(t)$ called wavelets [26]:

$$C\,(a,b) = \int_{-\infty}^{\infty} f(t)\cdot\psi_{a,b}(t)\ dt \tag{13}$$

The wavelets are generated from a single mother wavelet $\psi(t)$ by dilation and translation

$$\Psi_{a,b}(t) = \frac{1}{\sqrt{|a|}}\ \Psi^{*}\left[\frac{(t-b)}{a}\right] \tag{14}$$

where:

*f(t)* is the signal to be analyzed, a is the scale factor, and b is the translation factor. As seen in the above equation, the transformed signal is a function of two variables, the scale "a" and the translation "b". The term wavelet means a small wave or window function. The term translation is related to the location of the window as the window is shifted through the signal. The scale parameter is defined as 1/frequency. In the above equation *f(t)* is the signal to be analyzed in order to find its frequency content and the time of occurrence of its frequencies. The mother wavelet is chosen to serve as a prototype for all windows in the process. All windows that are used are the dilated (or compressed) and shifted versions of the mother wavelet. The computation starts with a scale a=1. The wavelet is placed at the beginning of the signal at the point which corresponds to time t=0. This wavelet function is multiplied by the signal and then integrated over all times. The final result is the value of the wavelet transform at time t=0 and scale a=1. The wavelet at scale 1 is then shifted towards the right by "b" amount and the above equation is computed. The procedure is repeated until the wavelet reaches the end of the signal. This process is repeated for every value of the scale "a".

Filters of different cut off frequencies are used to analyze the signal. A continuous wavelet transform can operate at each scale. Also the analyzing wavelet is shifted smoothly over the full domain of the analyzed function. In discrete wavelet transform (DWT), scales and positions of powers of two are chosen. An efficient way to implement this scheme using filters was developed by Mallat in 1988 [27]. Given a signal S of length N, the DWT consists of stages at most. The first step produces, starting from S, two sets of coefficients: approximation coefficients CA1 and the details coefficients CD1. These vectors are obtained by convolving S with a low pass filter for approximations, and with a high pass filter for details, followed by dyadic decimation. The next step splits the approximation coefficients CA1 into two parts using the same scheme, replacing S by CA1 and producing CA2 and CD2, and so on.For many signals, the low-frequency content is the most important part. It gives the signal identity. The high-frequency content, on the other hand, imparts flavor or nuance. In wavelet analysis, the approximations are the low-frequency components of the signal and the details are the high-frequency components [28]. It is possible to generate the original signal back from the coefficients through wavelet reconstruction. We can modify the wavelet coefficients before

performing the reconstruction step. The speech signal is a good application as this signal has a localization in both time and frequency domains. So speech processing can be done using either time analysis methods which manipulate the speech signal in time domain or frequency analysis methods which manipulate the speech signal via spectral parameters. The joint time frequency is the best representation for the speech signal. It takes the advantages of both simplicity of time based methods and powerful of frequency based methods in noise cancellation and signal compression [29].The idea behind signal compression using wavelets is primarily linked to the relative scarceness of the wavelet domain representation for the signal. After applying DWT, the frequencies that are most prominent in the original signal will appear as high amplitudes in that region of the DWT signal which includes those particular frequencies. The frequency bands that are not very prominent in the original signal will have very low amplitudes and that part of the DWT signal can be discard without any major loss of information, allowing data compression. This idea is used in our algorithm for compression of speech and audio signals. This means that data compression is then achieved by treating small valued coefficients as insignificant data and thus discarding them [30].

The process of compressing a speech signal using wavelets involves some experimental techniques such that the choice of the optimal mother-wavelet function and the effect of increasing the level of decomposition on the compression ratio are investigated. Also, the compression ratio is calculated using different wavelet functions at different levels. Wavelets work by decomposing a signal into different resolutions or frequency bands, and this task is carried out by choosing the wavelet function and computing the Discrete Wavelet Transform (DWT) [31]. The DWT on a given signal, the decomposition level can reach up to level $L = 2^K$, where K is the length of the discrete signal. Thus we can apply the transform at any of these levels. But in fact, choosing a decomposition level for the DWT usually depends on the type of signal being analyzed or some other suitable criterion such as entropy. For the processing of speech signals decomposition up to scale 5 is adequate [32], with no further advantage gained in processing beyond scale 5 and usually processing at a lower scale leads to a better compression ratio. There are two different approaches for calculating thresholds for the truncation of coefficients:

**Global threshold:**
The global threshold technique works by retaining the wavelet transform coefficients which have the largest absolute value. In this case you can manually set a global threshold, thus, only a single parameter needs to be selected. The coefficient values below this value should be set to zero, to achieve compression.

**Level dependent thresholding:**
This approach consists of applying visually determined level dependent thresholds to each decomposition level in the Wavelet Transform**.** The level-dependent threshold technique is derived from the Birge-Massart strategy [31].

The value of the threshold applied depends on the compression ratio we want to achieve. The task is to obtain higher compression ratios and an acceptable SNR needed to reconstruct the signal and detect it. There are many threshold selection rules. From these rules used here, threshold value can be calculated by $Thr = \sqrt{2\log(length(x))}$, where x is the signal to be compressed, and also is chosen by trail and error rule. For each level from 1 to n, threshold value is calculated and hard threshold is applied to detail coefficients. Signal compression is achieved by first truncating small-valued coefficients and then efficiently encoding them [31].

## EXPERIMENTS

### Data Bases
The Arabic speech data bases contain three files in wave formatting (.wav). File1 contains the speech of sound wave "بسم الله الرحمن الرحيم" that has a size of 26000 samples with 8000 sample per second and 16-bit per sample for a mono voice or a size of 26000 samples with 8000 two-dimensional vector samples per second and 32-bit per sample for a stereo voice. File2 contains the speech of sound wave "سورة الإخلاص" that has a size of 113741 samples with 8000 sample per second and 16-bit per sample. File3 contains a normal male speech that has a size of

146751 samples with 8000 sample per second and 16-bit per sample. These files are compressed using GMM and WT.

**Gaussian Mixture Model Algorithm**
**Step 1:**
Read speech file (.wav). This file may be 1-D or 2-D.
**Step 2:**
Construct GMM by using EM algorithm for the Arabic speech file.
**Step 3:**
Use GMM in designing quantizer i.e. calculation of quantization levels according to number of bits are used in quantization process.
**Step 4:**
The quantization process is carried out by calculating the decision boundaries and the reconstruction levels.

**Wavelet Decomposition Algorithm**
The process of compressing a speech signal using wavelets involves some experiments. The first experiment is the choice of the optimal mother-wavelet function. Different wavelet functions have been used to get the optimal wavelet function for making compression. The second experiment is to determine decomposition level. Different numbers of decomposition level is used to select the optimal decomposition level. The results of optimal wavelet function and optimal decomposition level are showed in the next section. The third experiment is to  select threshold that is used to truncate wavelet coefficients. Then, data compression is then achieved by truncating small valued coefficients and replacing them with zeros.
**Step 1:**
Read a speech file (.wav).
**Step 2:**
Apply the wavelet transform to the speech signal at specified level to obtain the approximation and detail coefficients.
**Step 3:**
Calculate threshold value and all values below this threshold are set to zero.
**Step 4:**
Use encoding scheme to get rid of the truncated coefficients. In this step, compression ratio is calculated.
**Step 5:**
Decode the stored / received signal.
**Step 6:**
Outputs are the reconstructed speech signal from compressed speech. SNR, PSNR and NRMSE are calculated.

## RESULTS AND DISCUSSIONS

The results obtained using GMM in quantization process are presented for both mono and stereo voice sources. The mono voice source requires a one-dimensional VQ and the stereo voice source requires two-dimensional VQ. For mono voice "file1", a GMM of 5 components is constructed using the EM algorithm and The EM algorithm runs for 15 iterations to get stable GMM. Fig.2 shows the original sound wave "file1" before quantization. Fig.3 illustrates constructed probability density function that consists of a number of Gaussian distribution functions and number of quantization levels calculated for 7 bit quantization. Fig.4 shows the sound wave "file1" after quantization using 7 bit quantization.
The results obtained using GMM for a mono voice "file1" are summarized in table 1. The quality of the speech at signal to noise ratio of 6 dB is good using the MOS ranking test. It can be heard without problems at compression ratio of 8.
For a stereo voice "file1", a GMM of 7 components is constructed using the EM algorithm and the EM algorithm runs for 15 iterations to get stable GMM. Fig.5 shows the used original sound wave "file1" at the left-hand speaker before quantization. Fig.6 shows this original sound wave "file1" at the right-hand speaker before quantization. Fig.7 shows the distribution of the original data representing the stereo voice and depicts the seven components of the constructed GMM;
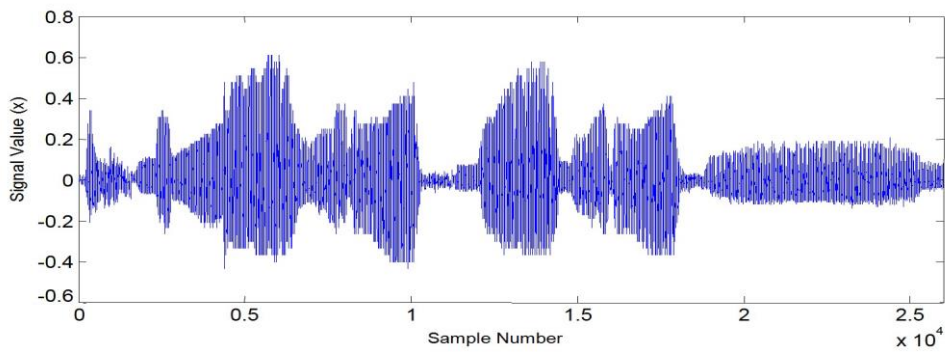
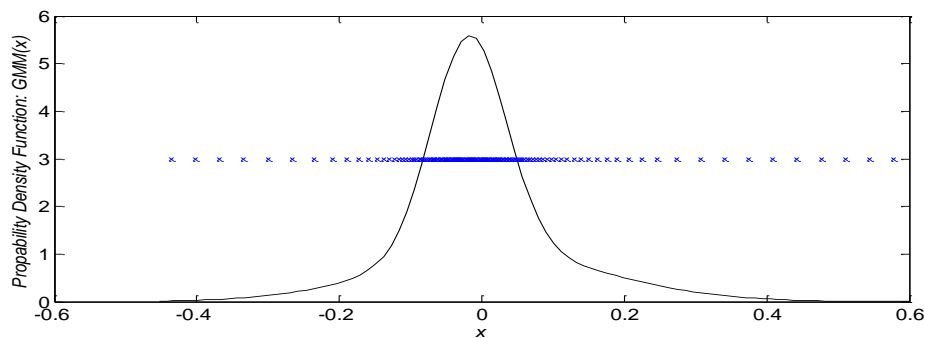**Fig. 2: Original sound wave "file 1" before quantization**



**Fig. 3: Constructed probability density function and the 128 quantization levels (7-bit)**
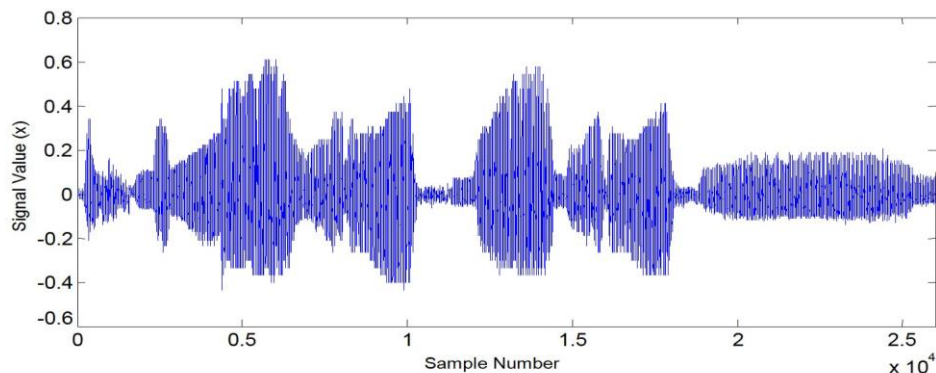


**Fig. 4: Sound wave "file 1" after quantization using 128 quantization levels (7-bit)
(CR = 2.28, SNR =  32 dB)**

**Table 1: The results of compression ratio and SNR for mono voice "file 1"**

| n bits | 7 | 6 | 5 | 4 | 3 | 2 |
|--------|------|------|------|------|------|---|
| C.R    | 2.28 | 2.67 | 3.2  | 4    | 5.33 | 8 |
| SNR db | 32   | 28.1 | 22.2 | 17.9 | 11.5 | 6 |

 "file1" at the right-hand speaker before quantization. Fig.7 shows the distribution of the original each component is shown as an ellipse which has the eigenvectors of the covariance matrix as axes and the radii of twice the square root of the corresponding eigen-value. Fig. 8 shows the original data of the stereo voice signal and number of quantization vectors used for 6 bit quantization. Figs.9-10 show quantized sound wave at the left-hand speaker and the right-hand speaker for 6 bit value for the component of each code-vector.
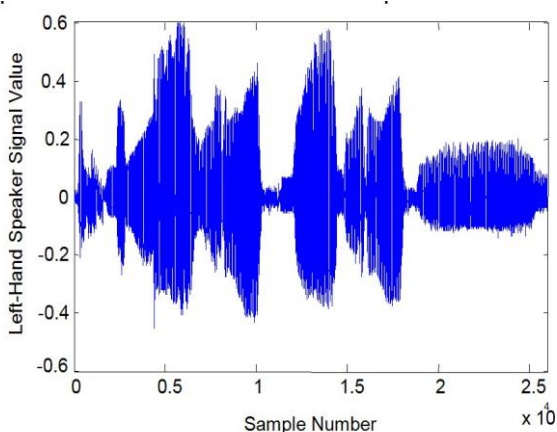
**Fig. 5: Original wave "file 1" at the left-hand Speaker before quantization**
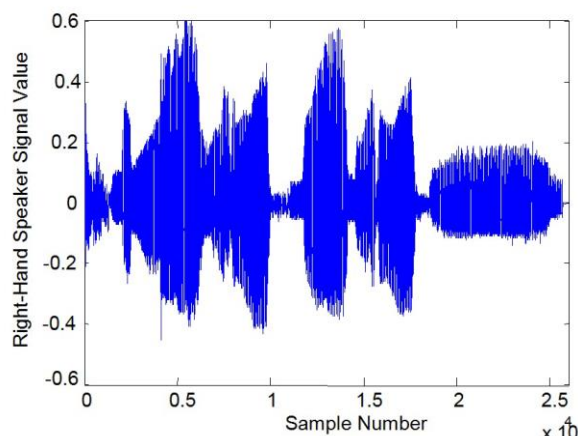


**Fig. 6: Original wave "file 1" at the right hand speaker before quantization**
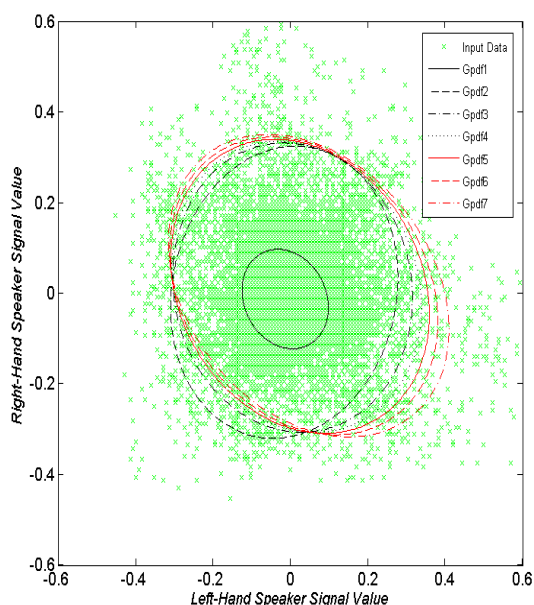


**Fig. 7: The data representing the stereo and the ellipses representing the 7 components of the constructed GMM**
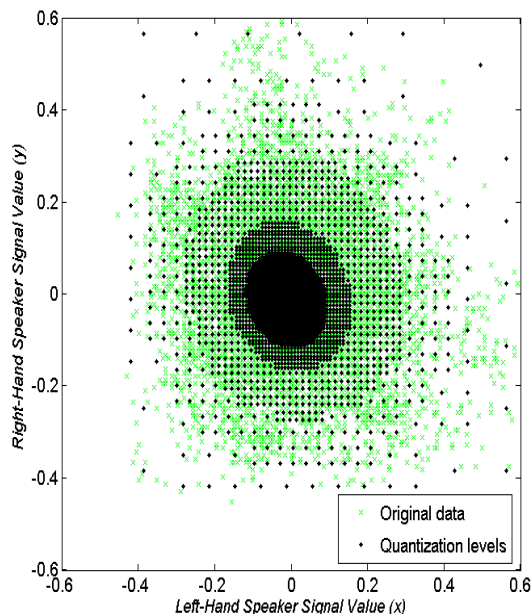


**Fig. 8: The original data of the stereo voice and 4096 quantization vectors using 6-bit value for each codevector (i.e. 12 bits per sample)**

Fig. 11 illustrates relationship between the speech compression ratio and signal-to-noise ratio for the stereo voice signal presented in Figs. 5-6. The quality of speech at C.R of 8 with SNR of 6.2 is good based on the MOS ranking test and it is heard clearly. We choose number of bits for quantization process according to value of compression ratio needed to compress the signal and value SNR desired to reconstruct the signal and detect it. Compression ratio is related (inversely) to the SNR dB.

If we do the same experiments for a mono voice "file 2", we will obtain to results similar to results before. Table 2 illustrates the results of compression ratio and SNR. Also, if we do the same experiments for a mono voice "file 3", we will obtain to results similar to results before. Table 3 illustrates the results of compression ratio and SNR. The quality of speech at C.R of 8 with SNR of 2.5 is worse.

Compression ratio using wavelet technique has been evaluated for different values of threshold, decomposition level as well as different wavelet functions. Fig. 12 illustrates the relation
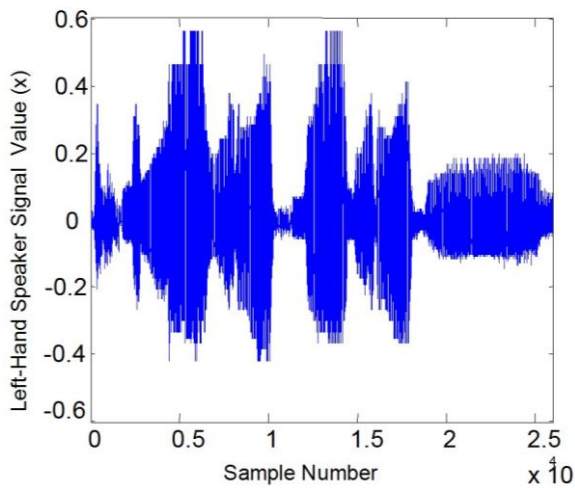
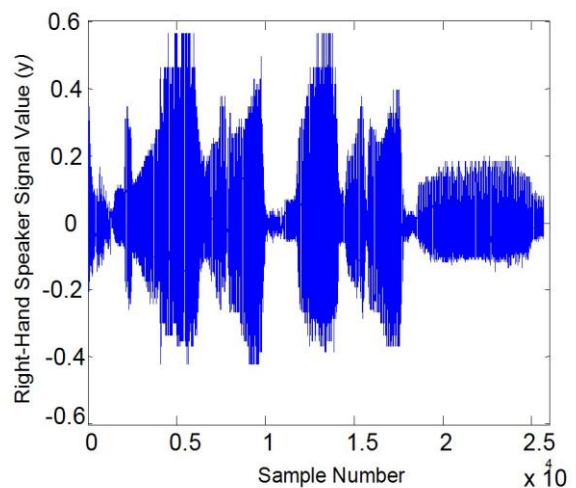**Fig. 9: Quantized wave "file 1" at the left-hand Speaker shown in Fig. 8**

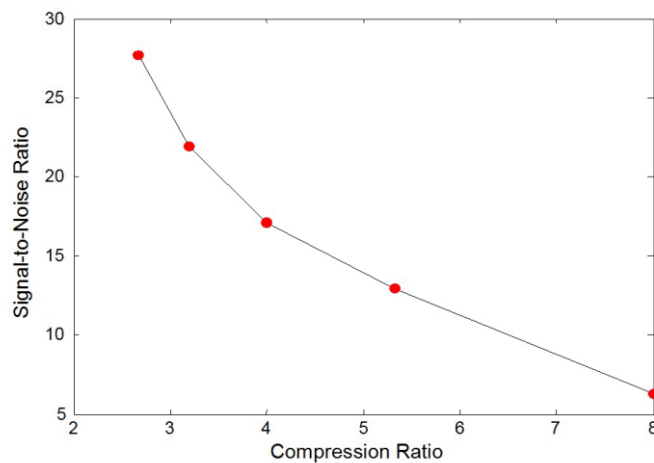**Fig. 10: Original wave "file 1" at the right hand speaker shown in Fig. 8**



**Fig. 11: Relation between speech compression ratio and signal-to-noise ratio for stereo voice "file 1"**

**Table 2: The results of compression ratio and SNR for mono voice "file 2"**

| n bits | 7 | 6 | 5 | 4 | 3 | 2 |
|--------|------|------|------|------|------|-----|
| C.R | 2.28 | 2.67 | 3.2 | 4 | 5.33 | 8 |
| SNR db | 33 | 29.4 | 23.7 | 18.2 | 13 | 8.6 |

**Table 3: The results of compression ratio and SNR for mono voice "file 3"**

| n bits | 7 | 6 | 5 | 4 | 3 | 2 |
|--------|------|------|------|------|------|-----|
| C.R | 2.28 | 2.67 | 3.2 | 4 | 5.33 | 8 |
| SNR db | 29 | 25.1 | 19.1 | 14 | 8 | 2.5 |

between the level of decomposition and the Compression Ratio. It is clear that the optimal level is found to be the second level. This means that the highest C.R can be obtained at level 2. Fig. 13 illustrates the relation between the compression ratio using different wavelets at different levels of decompositions for file 1. It is clear that the optimal wavelet type is found to be Bior3.1. Db10 and Sym8 are comparable in their ratio. Haar gives the lowest compression ratio. Also, it is noted that, after level 3, the compression ratio is approximately constant.
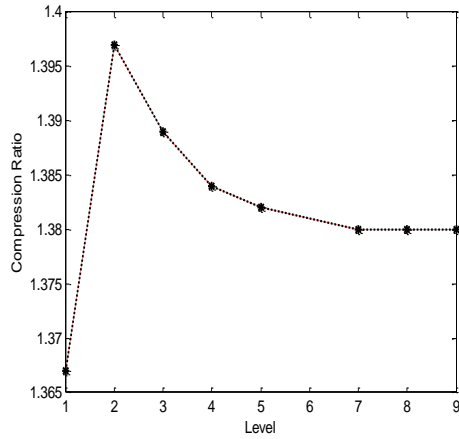


Fig. 12: Relation between the level and compression ratio for "file 1", bior 3.1
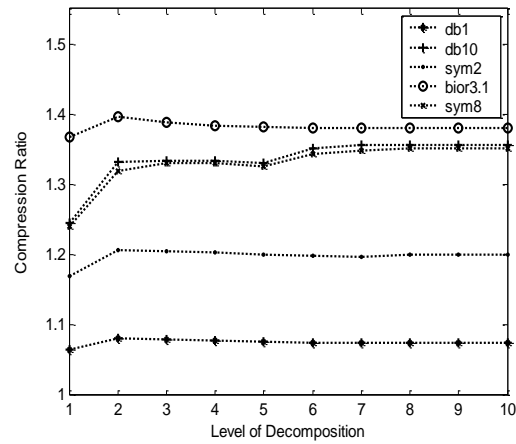


Fig. 13: Compression ratio using different wavelet types at different levels for "file 1"

The relation between compression ratio and the threshold is given in Fig. 14. It is obvious that after threshold of 0.3 the compression ratio becomes constant. In this paper, the task is to obtain higher compression ratios and an acceptable SNR needed to reconstruct the signal and detect it. Fig. 15 illustrates the relation between the compression ratio and the signal to noise ratio. With increasing the compression ratio, the signal to noise ratio is decreased. At of 6 dB, the speech quality is found to be good according to MOS ranking test.
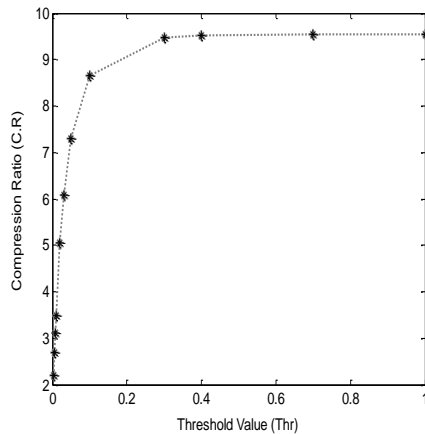


Fig. 14: Relation between threshold value & C.R at n =3, Bior 3.1 for "file 1"
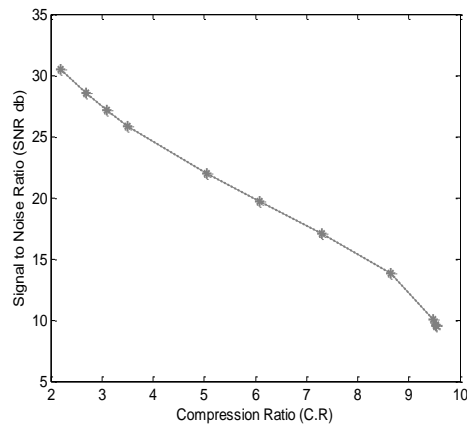


Fig. 15: Relation between the C.R and SNR at n =3, Bior 3.1 for "file 1"

A comparison between GMM and WT for three files is shown in Fig. 16. It is clear that, for file 1 & 2, GMM is better than wavelet transform in SNR db at any value of compression ratio and the speech quality is acceptably even though for high compression ratios. But for wavelet transform, speech sound wave is not acceptably for high compression ratios. These results are for Holy Quran. For example, in file1, when the compression ratio equals 2.67 "low", SNR for GMM equals 28 db but for wavelet equals 14.05 db and also when the compression ratio equals 8 "high" SNR for GMM equals 6 db but for wavelet equals 1.5 db. In this case, the quality of speech at SNR is good based on the MOS ranking test and it is heard clearly. Also it is noted

that, for file 3, GMM and wavelet transform are relatively equal in value SNR db. As wavelet transform gives results for SNR better than results are obtained from file1 & 2. For example, when the compression ratio equals 2.67 "low", SNR for GMM equals 25.1 db but for wavelet equals 23.8 db and also when the compression ratio equals 8 "high" SNR for GMM equals 2.5 db but for wavelet equals 3 db. It is noted that when compression ratio increases to a certain high value (i.e. C.R = 8), the speech quality is not acceptably for GMM and wavelet transform. These results are for normal male speech.
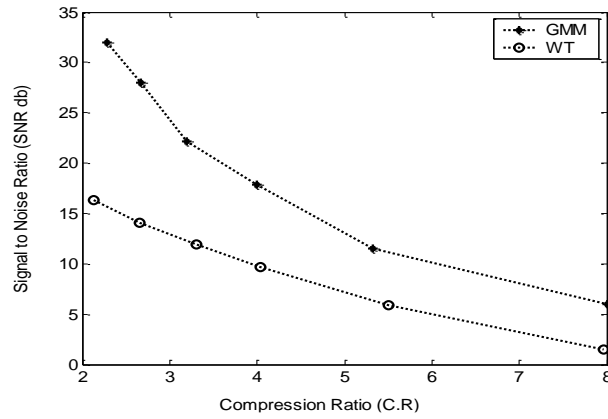


**(a) for file 1**
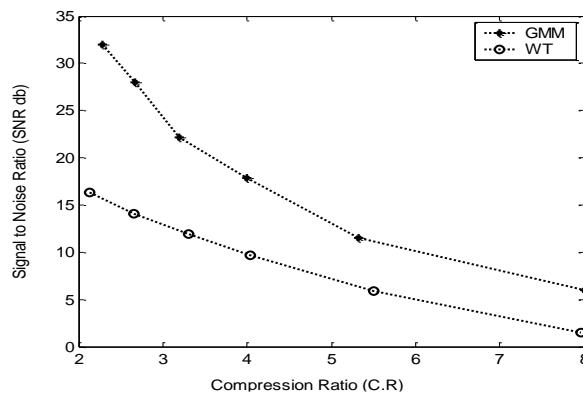


**(b) for file 2**
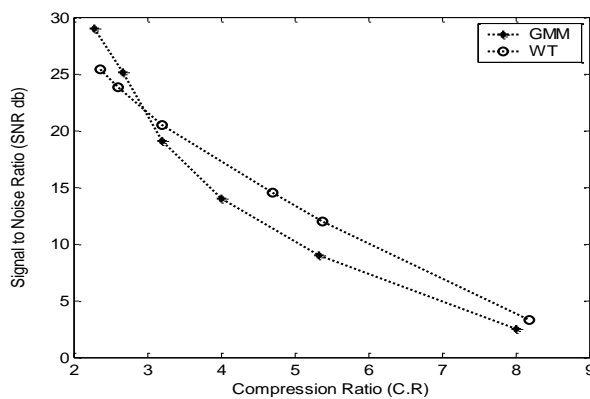


**(c) for file 3**

**Fig. 16: Relation between the compression ratio and the signal to noise ratio (db) in case of GMM and WT (a) for file 1 (b) for file 2  (c) for file 3**.

## CONCLUSIONS

This article introduces two different techniques for Arabic speech compression. These techniques are Gaussian Mixture based Model (GMM) and Wavelet based model. It is found that Gaussian Mixture Model (GMM) based on EM algorithm gives good compression ratios with acceptable SNR. For mono and stereo voice, the quality of output speech is nearly identical. The Bior3.1 and Db10 wavelet functions can be used for speech compression as they give better results than other wavelet functions.Increasing the level of decomposition increases the compression ratio, but after a certain level, the compression ratio becomes approximately constant. No further enhancements were achieved beyond level 3 decomposition. Also, in wavelet compression, the threshold choice affects extremely the quality of the output speech.Gaussian Mixture Model is better than Wavelet transform in speech compression especially for Holy Quran even though for high compression ratios. But, for normal speech, Gaussian Mixture Model and Wavelet transform give a relatively equal value for low compression ratios. When compression ratio increases to a certain high value, wavelet transform gives SNR better than SNR that is obtained from GMM. However, this speech is not acceptably at this value of high compression ratio.

## REFERENCES

1.  Andreas S. Spanias, "Speech Coding: A Tutorial Review", Department of Electrical Eng., Telecomm. Research Center, Arizona State University, January, 2002.
2.  I. Gerson and M. Jasiuk, "Vector Sum Excited Linear Prediction (VSELP) Speech Coding at 8kbits/s", proc.ICASSP-90, pp. 461-464, New Mexico, Apr., 1990.
3.  W. B. Kleij et al, "Fast Methods for the CELP Speech Coding Algorithm", IEEE Trans. ASSP- 38(8), p.1330, Aug., 1990.
4.  Y. Shoham, "Constrained Stochastic Excitation Coding of Speech at 4.8kb/s.", In Advances in Speech Coding, Eds: B. Atal, V. Cuperman, and A. Gersho, Kluwer Ac. Publ., 1990.
5.  M. McLaughlin, "Channel Coding for Digital Speech Transmission in the Japanese Digital Cellular System,", Meeting of IEICE, RCS90-27, Nov.,1990.
6.  J. Hardwick and J. Lim, "The Application of the IMBE Speech Coder to Mobile Communication", Proc. ICASSP-91, pp. 249-252, May 1991.
7.  D. Kemp et al, "An evaluation of 4800 bits/s Voice Coders", Proc. ICASSP-89, p.200, Glascow, Apr., 1980.
8.  B. Atal, V. Cuperman, and A. Gersho, "Advances in Speech Coding", Kluwer Ac.Publ., 1990.
9.  Siu-Wah Wong, "An Evaluation of 6.4 kbits/s Speech Codecs for the INMARSAT_M System", Proc. ICASSP-90, PP. 629-632, Toronto, May, 1991.
10. Lawrence R. Rabiner and Ronald W. Schafer, "Introduction to Digital Speech Processing ", Foundation and Trends in Signal Processing, Vol. 1, Nos.1-2(2007) 1-194.
11. P. Hedelin and J. Skoglund, "Vector Quantization Based on Gaussian Mixture Models", IEEE Trans. Speech and Audio Processing, July, 2000, vol. 8, no. 4, pp. 385-401.
12. A. Graps, "An Introduction to Wavelets", IEEE Computational Sciences and Engineering, http://www.amara.com/IEEEwave/IEEEwavelet.html (current Mar.15, 2001).
13. G. Strang and T. Nguyen, "Wavelets and Filter Banks", Wellesley-Cambridge Press, 1996.
14. J. S. Walker, "Wavelets and their Scientific Applications", Chapman and Hall/CRC, 1999.
15. J.R. Deller, J.G. Proakis and J.H. Hanssen, "Discrete-Time Processing of Speech Signals", Macmilla, New York, 1993.
16. S.R.Quackenbush, T.P Barnwell and M.A.Clement, :Objective Measures of Speech Quality", Prentic Hall, Englewood Cliff, NJ, 1988.
17. Khalid Sayood, "Introduction to DATA COMPRESSION', Morgan Kaufmann Publishers, Rlsevier, 2006.
18. J. Max , "Quantizing for Minimum Distortion ", IRE Transaction on Information Theory, It-6:7-12, January 1960.
19. S. P. Lloyed, "Least square quantization in PCM", IEEE Transaction on Information Theory, Vl.28, pp. 129-137, March 19982.
20. A.P. Dempster, N. M. Laird, and D. B. Rubin, "Maximum likelihood from incomplete data via the EM algorithm", J. R. Statist. Soc., 1977, vol. 39, pp. 1-37.

21. Sean Borman, "The Expectation Maximization Algorithm: a short tutorial", Augest 2006.
22. D. Subramaniam and B.D. Rao," PDF Optimized Parametric Vector Quantization of Speech Line Spectral Frequencies", IEEE Trans. Speech, Audio Processing, vol. 11, pp. 130-142, March 2003.
23. Sam Vakil, "Gaussian Mixture Model Based Coding of Speech and Audio ", Master thesis in department of electrical & computer engineering, McGill University, Montreal, Canada, October 2004.
24. Z. Ghahramani and M. I. Jordan, "Supervised learning from incomplete data via an EM approach", in Advances in Neural Information Processing Systems, vol. 6. Morgan Kaufmann Publishers, Inc., 1994, pp. 120-127.
25. Tiago Henrique Falk, "Objective Speech Quality Estimation using Gaussian Mixture Models", Master thesis in department of electrical & computer engineering, Queen's University Kingston, Ontario, Canada May 2005.
26. Y. T. Chan, "Wavelet Basics", Kluwer Academic Publishers, 1995.
27. Mallat, S., "A Theory for Multi-resolution Signal Decomposition: The Wavelet Representation", IEEE Trans. on Pattern Analysis and Machine Intelligence, pp.674693, July 1989.
28. Wavelet Toolbox User's Guide, copyright 1996-1997 by the Math Works, Inc
29. E.M.Saad, M.Aboul-Wafa, H.Amer, B.Said, "Firmware Implementation of the Discrete Wavelet Transform", AL-AZHAR Engineering Sixth International Conference, September 1-4, 2000, pp. 177-186.
30. P.S.Sathidevi and Y.Venkataramani, "Applying Wavelet Analysis in Coding of Speech and Audio Signals for Multimedia Applications", Published in the web site www.black.csl.uiuc.edu/~meyn, International Conference on Stochastic Optimization and Adaptation, ICSOA 2000, CUSAT, Cochin, December 2000.
31. E.B. Fgee, W.J. Phillips, W. Robertson, "Comparing Audio Compression using Wavelets with other Audio Compression Schemes", IEEE Canadian Conference on Electrical and Computer Engineering, IEEE, Edmonton, Canada, 1999, pp. 698-701.
32. Jalal Karam, and Raed Saad, "The Effect of Different Compression Schemes on Speech Signals", pp. 230-234,  International Journal of Biomedical Sciences Volume 1 Number 4, 2007.